Peter Wied, BSc.

Engineering Rieske Non-Heme Oxygenases for Improved Electron Transfer in Light-driven biocatalysis

Masterarbeit

zur Erlangung des akademischen Grades

Diplom-Ingenieur

Masterstudium Biotechnologie

eingereicht an der

Technischen Universität Graz

Betreuer

Dr. Sandy Schmidt

Prof. Dr. Robert Kourist

Institute für Molekulare Biotechnologie

Graz, November 2018

EIDESSTATTLICHE ERKLÄRUNG

Ich erkläre an Eides statt, dass ich die vorliegende Arbeit selbstständig verfasst, andere als die angegebenen Quellen/Hilfsmittel nicht benutzt, und die den benutzten Quellen wörtlich und inhaltlich entnommenen Stellen als solche kenntlich gemacht habe. Das in TUGRAZonline hochgeladene Textdokument ist mit der vorliegenden Masterarbeit identisch.

Datum Unterschrift

ACKNOWLEDGMENTS

I would like to express my appreciation to Prof. Robert Kourist for giving me the opportunity of conducting my master thesis in his research group and providing me with valuable suggestions during the planning of my research project.

I would also like to express my deepest gratitude to Dr. Sandy Schmidt, for her patient guidance, valuable insights and constructive suggestions during the planning and development of this research project, as well as her readiness of giving me her valuable time so generously, which was very appreciated.

My grateful thanks are also expressed to everyone in the research group. I would like to thank Anna Schweiger, Hanna Büchsenschütz, Ivana Drienovska and Melissa Horvat for the scientific discussions and inspiration, which helped me in becoming a more proficient scientist. Special thanks also to Clemens Farnleitner, Maria Schabhüttl, Daniel Mertschnigg for their support in the everyday lab routine.

I would also like to acknowledge and thank Prof. Hideaki Nojiri for providing me with the plasmid harboring CDO. Moreover, I would like to express my thanks to Jakob Sinnitsch, who supplied his expertise and equipment in the construction of the 3D-printed photobioreactor.

Special thanks and gratitude to my parents who never gave up on me and without whom I would not have had the possibility of following my scientific passion. Last, but certainly not least, Maria Sinnitsch, who supported me every step of the way and encouraged me, albeit having to put up with my frustrations, and sharing my excitement during scientific breakthroughs.

ABSTRACT

Rieske non-heme iron oxygenases (ROs) are able to catalyze the chemo-, regio- and stereoselective oxyfunctionalization of a large number of alkenes and arenes. Nevertheless, common issues in redox biocatalysis are the requirement of cofactors, which create an economical challenge for the implementation of oxidoreductases in industrial processes. In this study, an alternative light-driven cofactor supply was established for the *in vivo* regio- and stereospecific hydroxylation of alkenes by using *E. coli* cells harboring the cumene dioxygenase (CDO) from *Pseudomonas fluorescens* IP01. A first examination of the CDO system consisting of codon-optimized genes revealed, that expression of active enzyme could not be achieved in *E. coli*. However, the conducted optimization of the system highlight successful strategies for the expression of soluble enzyme in *E. coli*, *e.g.* by co-expressing chaperones (GroEL/GroES). After successfully expressing CDO as native genes, the *in vivo* photobiocatalytic approach was established. Hence, the photosensitizers flavin mononucleotide (FMN), eosin Y (EY) and rose bengal (RB) were examined for their capability of acting as intermediate electron shuttles. Moreover, ethylenediamine-tetraacetic acid (EDTA) as well as triethanolamine (TEA) have been investigated as sacrificial electron donors in the desired *in vivo* photobiocatalytic approach. The successful conversion of (*R*)-(+)-limonene to (1*R*,5*S*)-carveol was achieved by using the combination of EY/EDTA and RB/EDTA under white light irradiation. Throughout this thesis, different light reactor concepts were examined, resulting in the creation of a novel 3D-printed photobioreactor. This study clearly demonstrates the proof-of-concept for the light-driven *in vivo* cofactor supply of CDO, thus representing the first light-driven activation of a RO for stereoselective hydroxylation reactions. While the microbial toxicity of limonene and carveol are still a challenge for the *in vivo* biocatalysis using *E. coli*, the investigation of further substrates will pave the way for the application of this system with additional ROs.

ZUSAMMENFASSUNG

Rieske Nicht-Häm Eisen Oxygenasen (ROs) können die chemo-, regio- und stereoselektive Oxyfunktionalisierung einer großen Anzahl von Alkenen und Arenen katalysieren. Dennoch ist ihre Anwendbarkeit für industrielle Zwecke vor allem aufgrund ihrer Cofaktorabhängigkeit limitiert. Aus diesem Grund werden aktuell alternative Strategien zur Cofaktor-Regenerierung entwickelt. In dieser Arbeit wurde eine Methode zur lichtgetriebenen Cofaktor-Regenerierung entwickelt, um in einem Ganzzellsystem mittels der Cumene Dioxygenase (CDO) aus *Pseudomonas fluorescens* IP01, die Hydroxylierung von Alkenen in *E. coli* zu katalysieren. Die Untersuchung des CDO-Systems ergab, dass Codon-optimierte Gene nicht zur Expression von aktiver CDO in *E. coli* führen. Dennoch konnte anhand einer Expressionsoptimierung gezeigt werden, dass die Coexpression von Chaperonen zu einer deutlichen Erhöhung des Ertrages an löslichem Protein führt. Nachdem native Gene, welche die CDO kodieren, erfolgreich exprimiert werden konnten, wurde der *in vivo* photobiokatalytische Ansatz zur Cofaktor-Regenerierung etabliert. Hierzu wurden die Photokatalysatoren Flavinmononukleotid (FMN), Eosin Y (EY) und Bengalrosa (RB) auf ihre Fähigkeit untersucht, als intermediäre Elektronen-Transporter zu fungieren. Darüber hinaus wurden sowohl Ethylendiamintetraessigsäure (EDTA) als auch Triethanolamin (TEA) als Elektronendonor in der gewünschten *in vivo* photobiokatalytischen Methode eingesetzt. Die erfolgreiche Umwandlung von (*R*)-(+)-Limonen zu (1*R*,5*S*)-Carveol konnte unter Verwendung der Kombination EY/EDTA und RB/EDTA unter Illumination mit weißen Licht erreicht werden. Zusätzlich wurden in dieser Arbeit verschiedene Lichtreaktorkonzepte untersucht, wodurch ein neuartiger 3D-gedruckter Photobioreaktor entstand. Weiterhin konnte in dieser Arbeit ein erster „proof-of-concept“ für die lichtgetriebene *in vivo* Cofaktor-Regenerierung der CDO gezeigt werden, wodurch stereoselektive Hydroxylierungsreaktionen erfolgreich durchgeführt wurden. Während die mikrobielle Toxizität von Limonen und Carveol nach wie vor eine Herausforderung für die *in vivo* Biokatalyse mit *E. coli* darstellt, könnte die Untersuchung weiterer Modellsubstrate den Weg für die Anwendung des Systems mit weiteren ROs bereiten.

TABLE OF CONTENTS

List of Abbreviations

Å	Ångström
BVMO	Baeyer-Villiger monooxygenase
CDO	Cumene dioxygenase
CFE	cell-free extract
CumA1	α-subunit of the terminal oxygenase component of CDO
CumA2	β-subunit of the terminal oxygenase component of CDO
CWW	cell wet weight
DCM	dichloromethane
ddH_2O	double-distilled water
de	diastereomeric excess
EDTA	ethylenediaminetetraacetic acid
ee	enantiomeric excess
EY	eosin Y
FAD	flavin adenine dinucleotide
Fd	ferredoxin component of CDO
FdR	ferredoxin reductase component of CDO
FMN	flavin mononucleotide
GC-FID	gas chromatography - flame ionization
GC-MS	gas chromatography - mass spectrometry
H_2O_2	hydrogen peroxide
LB	*lysogeny* broth
LED	light emitting diode
MBC	minimal bactericidal concentration
MCS	multiple cloning site
MIC	minimum inhibitory concentration
NAD(P)H	nicotinamide adenine dinucleotide (phosphate)
nt	nucleotide
O_2	molecular oxygen
ONC	over-night culture
P450s	P450-monooxygenases
PCR	polymerase chain reaction
PLA	polylactide
RB	rose bengal
redox	oxidation-reduction
RGB	red green blue
ROs	Rieske non-heme iron oxygenases
SDS-PAGE	sodium dodecyl sulfate - polyacrylamide gel electrophoresis
SOC	super optimal broth with catabolite repression
TB	terrific broth
TEA	triethanolamine
T_m	melting temperature
w	weight
w/v	weight/volume
WT	wild-type

1 INTRODUCTION

1.1 OXIDOREDUCTASES FOR BIOCATALYTIC APPLICATIONS

The rising need for “Green” chemistry has increased the use of biocatalysts for the synthesis of fine and bulk chemicals, as well as the application of biocatalysts in pharmaceutical, food, cosmetic, textile, pulp and paper industries. Due to mild reaction conditions, especially concerning pH, pressure and temperature, biocatalysts have gained increasing importance in organic synthesis. Additionally, the ability to perform the reactions with high chemo-, regio- and stereoselectivity is a considerable benefit for biocatalysts over the 'classical' chemical approaches (Gamenara *et al.*, 2012; Choi, Han and Kim, 2015; Martínez *et al.*, 2017; Dong *et al.*, 2018). For instance, ketoreductases are applied for the synthesis of atorvastatin (cholesterol lowering drug) sidechains or Baeyer-Villiger monooxygenase (BVMO) for the synthesis of esomeprazole (stomach acid lowering drug) (Bornscheuer *et al.*, 2012).

Oxidoreductases (EC 1.-) gain increasing importance as alternatives or in combination with organic synthesis routes in chemical and pharmaceutical industries (Dong *et al.*, 2018). Classified as enzymes which act on their substrate involving electron transfer, oxidoreductases can perform oxidation-reduction (redox) reactions. Thus, this class of enzymes enables manifold reactions such as hydroxylation reactions, Baeyer-Villiger oxidations, the oxidation of alcohols, aldehydes, acids, and aromatic compounds, but also the reduction of ketones, aldehydes, C-C and C-N double bonds and reductive aminations. Compromising more than 25 % of all discovered enzymes so far, the group of oxidoreductases includes oxygenases, oxidases, peroxidases and dehydrogenases (Gamenara *et al.*, 2012).

Oxygenases are of particular interest due to the generation of new functional groups by the selective incorporation of oxygen (Dong *et al.*, 2018). For example, they are able to perform the asymmetric dihydroxylation of alkenes to vicinal diols, which alleviates the use of hazardous catalysts and thus being considered as environmentally more benign. For example, the application of oxygenases can replace conventional osmium tetroxide

catalyzed asymmetric dihydroxylation (Sharpless asymmetric dihydroxylation), which is still largely applied (Sharpless *et al.*, 1992; Mehrman *et al.*, 2004; Gally, Nestl and Hauer, 2015). The class of oxygenases are grouped in monooxygenases and dioxygenases. Monooxygenases only incorporate one oxygen molecule from molecular oxygen (O_2) and form water as a side product. Dioxygenases are capable of incorporating both oxygen atoms from molecular oxygen or even hydrogen peroxide (H_2O_2), thus, reducing a C-C double bond.

Dioxygenases are classified in the subclasses EC 1.13.- and EC 1.14.-. The former subclass of enzymes is acting on single donors without the use of a redox cofactor, the latter is acting on paired donors (Gamenara *et al.*, 2012). Being a heterologous group of enzymes, dioxygenases may be categorized as iron(II) or iron(III) non-heme iron oxygenases. The group of iron(II) dioxygenases compromises extradiol dioxygenases and Rieske-type oxygenases, which are capable of direct O_2 activation. Alternatively, iron(III) dioxygenases compromise lipoxygenases and intradiol oxygenases, which activate the substrate (Gamenara *et al.*, 2012).

1.2 Rieske Non-heme Iron Oxygenases (ROs)

Rieske iron non-heme dioxygenases (ROs) represent very promising biocatalysts to promote catalytic asymmetric dihydroxylation reactions of alkenes since they are the only enzymes known to catalyze the stereoselective formation of vicinal *cis*-diols in one step (Barry and Challis, 2013). Additionally, ROs create an alternative to conventional synthesis routes, namely Sharpless asymmetric dihydroxylation. Similar to P450-monooxygenases (P450s) in mammalian cells, ROs may be used in the bacterial metabolism to initiate the degradation of aromatic compounds by introducing *cis*-dihydroxylated metabolites (Ferraro, Gakhar and Ramaswamy, 2005; Chen *et al.*, 2014). Furthermore, it has been proposed that ROs are capable of performing a so called angular dioxygenation of polycyclic arenes (Figure 1) (Nojiri, Habe and Omori, 2001). This results in the formation of chemically unstable intermediates, which undergo spontaneous cleavage, followed by subsequent *meta* cleavage and hydrolysis. This atypical

form of oxygenation may be attributed to the large substrate scope, also described as "loose" substrate specificity of these enzymes (Nojiri, Habe and Omori, 2001).

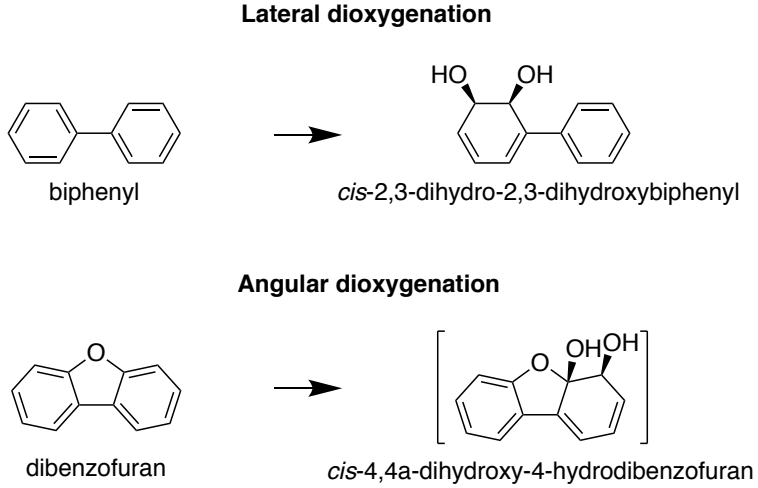

FIGURE 1 - Lateral vs. angular dioxygenation reaction adapted from Nojiri *et al.* (Nojiri, Habe and Omori, 2001).

Already in 2000, Gibson and Parales estimated that the small group of discovered ROs is able of forming more than 300 different *cis*-diols (Gibson and Parales, 2000). This relaxed substrate specificity has been shown extensively throughout the years, and has seen broad interest in the application of these enzymes for asymmetric dihydroxylation reactions (Wackett, 2002; Boyd *et al.*, 2005; Lipscomb and Hoffman, 2005; Dror and Fishman, 2012; Tøndervik *et al.*, 2012; Barry and Challis, 2013; Gally, Nestl and Hauer, 2015; Groeneveld *et al.*, 2016; Halder, Nestl and Hauer, 2018). Remarkably, in contrast to the large substrate scope, different ROs from different origins yield products with the same enantiopreference due to their evolutionary highly conserved active site (Wackett, 2002). In addition to their capability of performing *cis*-dihydroxylation reactions, it has been shown that ROs also catalyze monohydroxylation reactions, which further broadens their application potential for biocatalysis (Barry and Challis, 2013). Moreover, ROs can catalyze a wide variety of different reactions, such as, C-N-bond cleavage, O/N-demethylation, desaturation, N-oxygenation and C-C bond formation reactions (Lee and Zhao, 2006; Capyk *et al.*, 2009; D'Ordine *et al.*, 2009; Sydor *et al.*, 2011; Yoshiyama-Yanagawa *et al.*, 2011; Summers *et al.*, 2012; Kalnins *et al.*, 2018). Through the increasing understanding of mechanisms applied by ROs as well as the growing amount of ROs discovered, a lot of research towards

protein engineering of ROs has been conducted (Ang, Obbard and Zhao, 2007; Vézina, Barriault and Sylvestre, 2007; Kagami *et al.*, 2008; Gally, Nestl and Hauer, 2015). Gally *et al.* showed that the exchange of a methionine residue towards smaller amino acids like alanine within the active site of several ROs, the regioselectivity can be significantly shifted (Gally, Nestl and Hauer, 2015). Ang *et al.* performed saturation mutagenesis of the active site of the aniline dioxygenase from *Acinetobacter* sp. strain YAA, thus, widening the substrate scope for the acceptance of 2-isopropylaniline as well as increasing the activity of the wild-type (WT) enzyme towards already accepted substrates (Ang, Obbard and Zhao, 2007).

Recently, Halder *et al.* used a semi-rational engineering approach to determine mutations affecting substrate specificity, regioselectivity as well as stereoselectivity of naphthalene dioxygenase from *Pseudomonas* sp. strain NCIB 9816-4 (Halder, Nestl and Hauer, 2018). Furthermore, Halder *et al.* confirmed findings by Parales *et al.* which discovered that a phenyl residue at F352 plays a major role for the enantiomeric purity of the products (enantiomeric excess (*ee*) >9 %) (Parales *et al.*, 2000).

1.2.1 Classification of ROs

Over the past decades, several different RO classification systems have been proposed (Mason, 1992; Gibson and Parales, 2000; Nam *et al.*, 2001; Schmidt and Shaw, 2001; Kweon *et al.*, 2008). ROs can be classified as two or three component systems (Ferraro, Gakhar and Ramaswamy, 2005). The first classification by Batie *et al.* was based on these components forming the electron transport chain towards the terminal oxygenase (Batie, Ballou and Correll, 1992). Nam *et al.* created a classification based on pairwise sequence alignments and phylogenetic analyses (Nam *et al.*, 2001). Due to constraints detected in the classification by Nam *et al.*, a dynamic classification system was proposed by Kweon *et al.* (Kweon *et al.*, 2008). Ferraro *et al.* describe a classification scheme based on RO components (IA, IB, IIA, IIB and III) and a classification based on RO families (naphthalene, toluene/biphenyl, benzoate and phthalate) (Ferraro, Gakhar and Ramaswamy, 2005). Regarding the classification based on the electron-transfer components, two component systems are class IA and IB and three component systems are

grouped into IIA, IIB and III (Table 1). ROs are differentiated by the reductase and iron-sulfur cluster type. Classes IA and IB contains reductases with plant-type iron-sulfur clusters and either a flavin mononucleotide (FMN) or flavin adenine dinucleotide (FAD). The reductases of the three component ROs all contain a FAD (IIA, IIB, II). Additionally, class III ROs have a Rieske-type iron-sulfur cluster incorporated. Conversely, the ferredoxin component of IIA contains a plant-type iron-sulfur cluster, whereas, IIB and III contain Rieske-types. Accordingly, all oxygenase components contain a Rieske-type iron-sulfur cluster and Fe(II) (Ferraro, Gakhar and Ramaswamy, 2005).

TABLE 1 - RO classification as proposed by Ferraro *et al.* (Ferraro, Gakhar and Ramaswamy, 2005).

system	class	reductase	ferredoxin	oxygenase	example
2-component	IA	FMN $[2Fe\text{-}2S]_P$	-	$[2Fe\text{-}2S]_R$ Fe(II)	phthalate dioxygenase
	IB	FAD $[2Fe\text{-}2S]_P$	-	$[2Fe\text{-}2S]_R$ Fe(II)	benzoate dioxygenase
3-component	IIA	FAD	$[2Fe\text{-}2S]_P$	$[2Fe\text{-}2S]_R$ Fe(II)	dibenzofuran dioxygenase
	IIB	FAD	$[2Fe\text{-}2S]_R$	$[2Fe\text{-}2S]_R$ Fe(II)	cumene dioxygenase
	III	FAD $[2Fe\text{-}2S]_R$	$[2Fe\text{-}2S]_R$	$[2Fe\text{-}2S]_R$ Fe(II)	naphthalene dioxygenase

$_P$ plant-type iron sulfur cluster
$_R$ Rieske-type iron sulfur cluster

1.2.2 Catalytic Mechanism and Structure of ROs

Many enzymes containing iron-sulfur clusters can be found in nature. Usually grouped by the nature of their iron-sulfur cluster, ROs belong to the [2Fe-2S] cluster containing enzymes. In contrast to the [2Fe-2S] clusters described as plant-type and adrenodoxin, where the [2Fe-2S] cluster is coordinated by four cysteine residues, the Rieske-type iron-sulfur clusters are coordinated by two cysteine and two histidine residues. ROs build an intricate electron transport chain, utilizing a cofactor in form of nicotinamide adenine dinucleotide (phosphate) (NAD(P)H) to activate molecular oxygen (Figure 2). Depending on the RO components involved in the electron transport, ROs can consist of two or three component systems, as described earlier. Two-component ROs compromise a reductase and a terminal oxygenase. The reductase oxidizes NAD(P)H to $NAD(P)^+$, resulting in a direct electron supply for the terminal oxygenase, which converts the substrate by hydroxylation. Regarding the three-component ROs, a ferredoxin acts as an intermediate

electron shuttle, which transports electrons between the reductase and the terminal oxygenase (Ferraro, Gakhar and Ramaswamy, 2005).

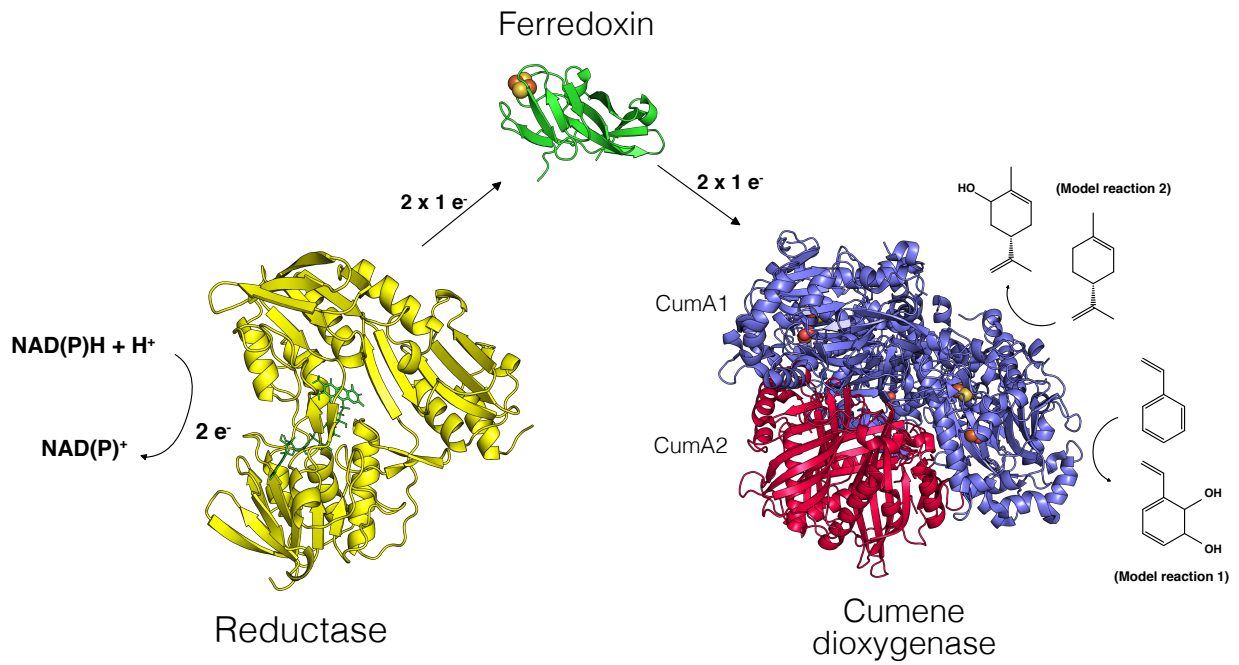

FIGURE 2 - Electron transfer chain of CDO, adapted from three-component ROs as proposed by Ferraro *et al.* (Ferraro, Gakhar and Ramaswamy, 2005).

The oxygen introduction catalyzed by ROs has been studied extensively, in particular using the naphthalene dioxygenase (NDO) as a model system to describe the mechanism involved (Wackett, 2002; Ferraro, Gakhar and Ramaswamy, 2005; Bugg and Ramaswamy, 2008; Barry and Challis, 2013). The oxygenation is a two-step process. First, molecular oxygen is activated, and secondly, the oxygen is incorporated into the substrate. After electron shuttle to the terminal oxygenase, the electron is accepted by the [2Fe-2S] Rieske cluster and transported to the mononuclear iron, where it is used for catalysis. Figure 3 shows the arrangement of the Rieske [2Fe-2S] and non-heme iron(II) clusters (Barry and Challis, 2013). The Rieske [2Fe-2S] cluster is coordinated by two histidine and two cysteine residues, whereas the non-heme iron(II) cluster is coordinated by a 2-His-1-carboxylate facial triad. In other words, the non-heme iron(II) cluster is incorporated in the catalytic site via two histidine and an aspartate residue (or glutamate residue). Both clusters are connected by a bridging aspartate residue. Due to the exposure

of the face of the mononuclear iron of the non-heme iron cluster in the hydrophobic active site, oxygen can bind and react with the substrate. For example, *cis*-dihydroxylation of the substrate is initiated through the side-on binding of molecular oxygen to the non-heme iron(II) cluster. In contrast to heme-dependent iron enzymes, up to three exogenous ligands are able to bind to the mononuclear iron in the active site, resulting in a variety of additional possible reactions (monohydroxylation, C-N-bond cleavage, O/N-demethylation, desaturation, N-oxygenation and C-C bond formation reactions) (Bassan, Borowski and Siegbahn, 2004; Ferraro, Gakhar and Ramaswamy, 2005; Lee and Zhao, 2006; Capyk *et al.*, 2009; D'Ordine *et al.*, 2009; Sydor *et al.*, 2011; Yoshiyama-Yanagawa *et al.*, 2011; Summers *et al.*, 2012; Barry and Challis, 2013; Kalnins *et al.*, 2018).

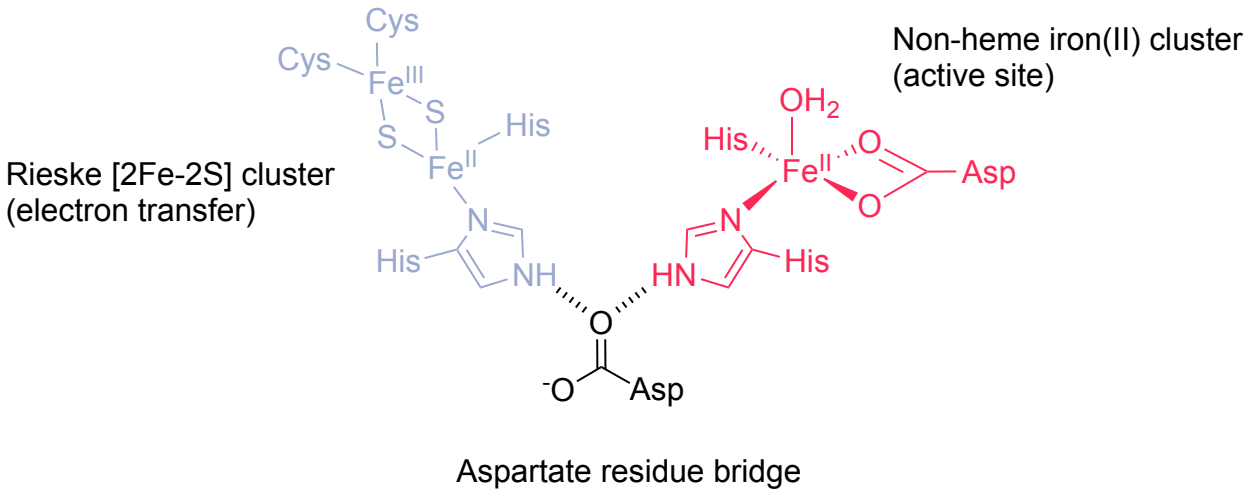

FIGURE 3 - Architecture of the [2Fe-2S] Rieske cluster (blue) and the non-heme iron centers (red) bridged by an aspartate residue (black), adapted from Barry and Challis (Barry and Challis, 2013).

For a deeper understanding of the mechanism involved in catalysis, one has to discuss the structure of the terminal oxygenase, which consists of an α- and β-subunit, arranged in an $\alpha_3\beta_3$ hexameric fashion (Colbert *et al.*, 2000; Dong *et al.*, 2005; Ferraro, Gakhar and Ramaswamy, 2005; Friemann *et al.*, 2009). Insights in solved crystal structures of ROs show that the distance between the Rieske [2Fe-2S] and the non-heme iron(II) clusters is closer between adjacent α subunits (~12 Å) and not within each subunit (~45 Å). Hence, suggesting that, the electron transfer between the Rieske [2Fe-2S] and non-heme iron(II) clusters takes place between adjacent α -subunits (Ferraro, Gakhar and

Ramaswamy, 2005; Barry and Challis, 2013). The function of the β-subunit is mainly attributed to that being of a structural purpose in ROs. However, it has been shown that for certain biphenyl dioxygenases the β-subunit plays a role in substrate specificity, as well as, activity (Hurtubise, Barriault and Sylvestre, 1998; Ferraro, Gakhar and Ramaswamy, 2005).

1.2.3 CUMENE DIOXYGENASE (CDO)

During this project, the cumene dioxygenase (CDO) from *Pseudomonas fluorescens* IP01 was investigated as model enzyme. To date, little examination of the CDO enzyme system has been performed (Aoki *et al.*, 1996; Habe *et al.*, 1996; Takami *et al.*, 1999; Dong *et al.*, 2005; Gally, Nestl and Hauer, 2015). The gene cluster encoding CDO (cumA1, A2 A3, A4) was first discovered by Aoki *et al.* in 1996 (Aoki *et al.*, 1996). Aoki *et al.* examined the degradation of cumene by *P. fluorescens* IP01 and recombinant *E. coli* containing genes encoding cumene-oxidizing enzymes. The gene cluster encoding for CDO was investigated using deletion analysis of each gene. Furthermore, sequence analysis showed a similar distribution, arrangement and homology of the CDO gene cluster with the toluene dioxygenase and biphenyl dioxygenase gene clusters (Aoki *et al.*, 1996). Different ROs can have substantial variations in their sequences, nevertheless, their structures show a high conservation (Dong *et al.*, 2005; Ferraro, Gakhar and Ramaswamy, 2005).

When creating a phylogenetic tree of cumA1 with sequences of terminal oxygenase from different ROs (obtained from Swiss-Prot), the resulting bootstrapped tree shows that cumA1 can be grouped to the biphenyl-2,3-dioxygenases, as shown in Figure 4. CumA1 shows the highest relation to the biphenyl-2,3-dioxygenases from *Pseudomonas sp.* KKS102, *Comamonas testosteroni*, *Paraburkholderia xenovorans* LB400 and *Pseudomonas pseudoalcaligenes* in descending order. The group of biphenyl-2,3-dioxygenases is most commonly related to the group of naphthalene dioxygenases. Whereas, biphenyl-2,3-diol 1,2-dioxygenases and catechol 2,3-dioxygenases build a distinct separate group.

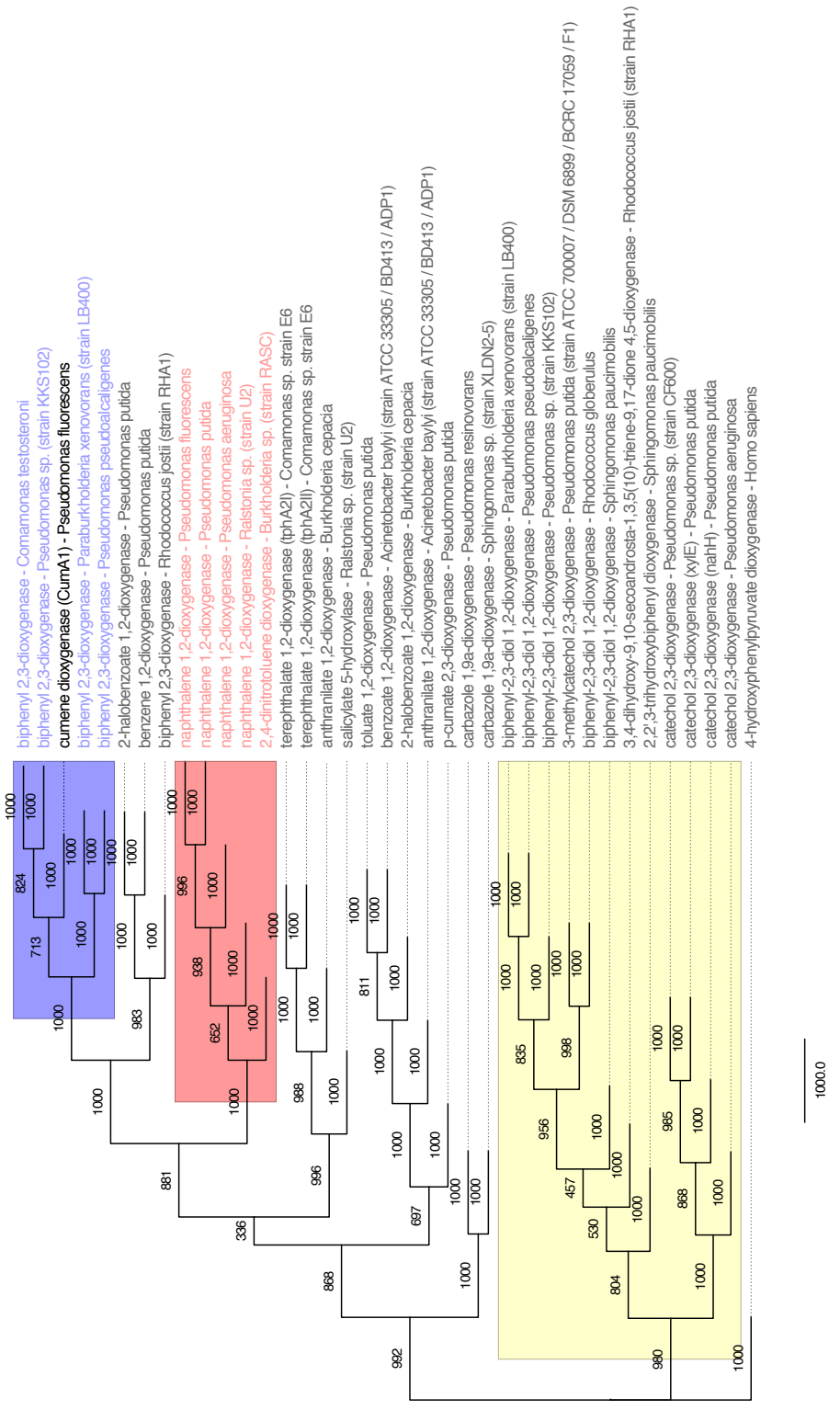

FIGURE 4 - Bootstrapped phylogenetic tree of CumA1 after a multiple sequence alignment with ROs obtained from SWISS-Prot. In (blue) the group of biphenyl 2,3-dioxygenases containing CumA1 from CDO. In (red) the group of NDO. In (yellow), a cluster of biphenyl-2,3-diol 1,2-dioxygenases and catechol 2,3-dioxygenases can be seen.

Further insight in the relatedness of different ROs can be provided by investigating their structural similarity (Ferraro, Gakhar and Ramaswamy, 2005). Ferraro *et al.* presented that the structure of the α-subunits of different ROs (*e.g.* NDO, BPDO, CARDO, CDO) show a high structural conservation at the N-terminal region of the protein, which contains the Rieske-cluster binding domain. However, an increased structural variability can be detected near the mononuclear iron-binding site. Although the β-subunits of different terminal oxygenases showed a low sequence homology a high structural conservation could be observed (Ferraro, Gakhar and Ramaswamy, 2005).

CDO belongs to the class of IIB ROs, which consists of a three-component electron transfer chain (Figure 2). The reductase oxidizes NAD(P)H to $NAD(P)^+$ and stores two electrons on a flavin. Ferredoxin shuttles then one electron at a time to the oxygenase, where the actual oxygenation reaction takes place. The crystal structure of the terminal oxygenase of CDO was solved in 2005 by Dong et al (Dong *et al.*, 2005). The terminal oxygenase of CDO consists of an α- and β- subunit in an $\alpha_3\beta_3$ arrangement (Figure 5). Whereas the α-subunit is the catalytic component, containing the iron cluster in its active site, the β-subunit determines the substrate specificity (Dong *et al.*, 2005; Ferraro, Gakhar and Ramaswamy, 2005)

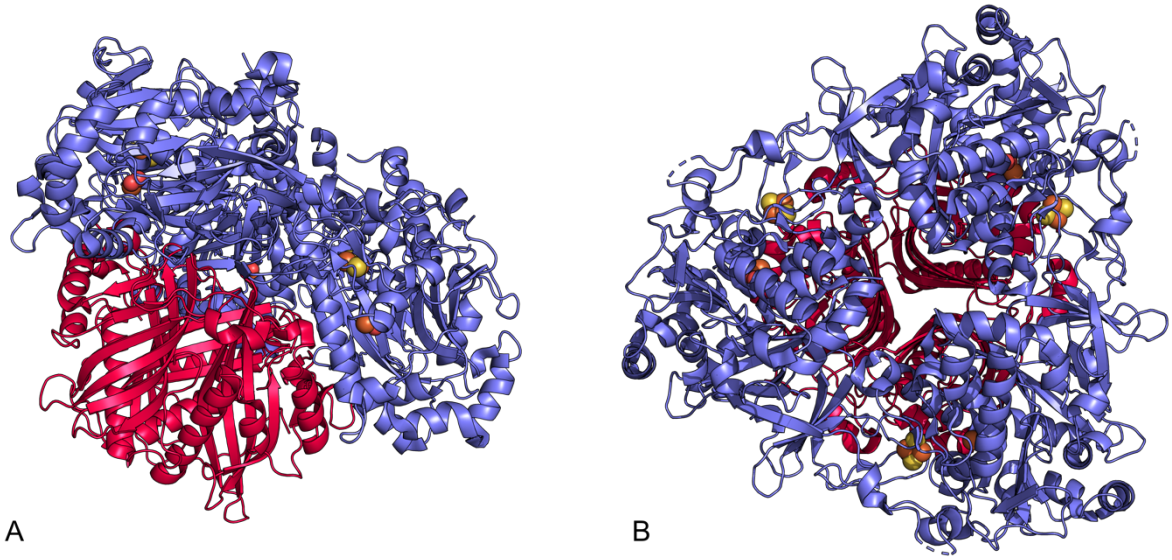

FIGURE 5 - Structure of the $\alpha_3\beta_3$ arrangement of the terminal oxygenase of CDO. (blue) the α-subunits and (red) the β-subunits. (A) shows the side view, (B) shows the top view. Visualized using PyMOL (DeLano, 2000; Dong *et al.*, 2005).

The substrate specificity of CDO was first investigated by Aoki *et al.* (Aoki *et al.*, 1996). Out of 24 hydrocarbons examined, *meta*-cleavage products were detected for 18. Notably, recombinant *E. coli* JM109 harboring CDO were able to form *meta*-cleavage compounds although they could not be utilized as substrate for growth in *P. fluorescens* IP01 (*e.g.* styrene, biphenyl) (Aoki *et al.*, 1996). Takami *et al.* investigated the substrate scope of CDO, in respect to chlorinated alkenes (Takami *et al.*, 1999). They showed that CDO was capable of oxygenating non-chlorinated and chlorinated alkenes. Interestingly, alkenes with a chlorine substitution on the double-bonded carbon atoms were monooxygenated at this position (Takami *et al.*, 1999). Gally *et al.* first established a protein engineering approach to improve selectivities and conversions of CDO towards various olefins, for example the hydroxylation of styrene, limonene, indene or 7-methyl-3-methyleneocta-1,6-diene (Gally, Nestl and Hauer, 2015). By site-directed mutagenesis, the active site of CDO was modified to investigate a shift in regio- and enantioselectivity. Selected amino acid exchanges were inspected, whereas the decreasing size of the side-chains of selected amino acid residues correlated with a shift in regioselectivity as well as stereoselectivity. Namely, the exchange of a methionine residue to an alanine residue (M232A) increased the conversion of styrene to 1-phenylethane-1,2-diol from 0.3 % to 92 %. (Figure 6). Additionally, the stereospecificity for (*R*)-1-phenylethane-1,2-diol was increased by 52 % to an *ee* of 95 %. To conclude, Gally *et al.* demonstrated that the selectivities as well as the activity of CDO variant M232A can be increased for various different aliphatic compounds, including the conversion of limonene to carveol (Figure 7) by rational protein design (Gally, Nestl and Hauer, 2015).

Model reaction 1:

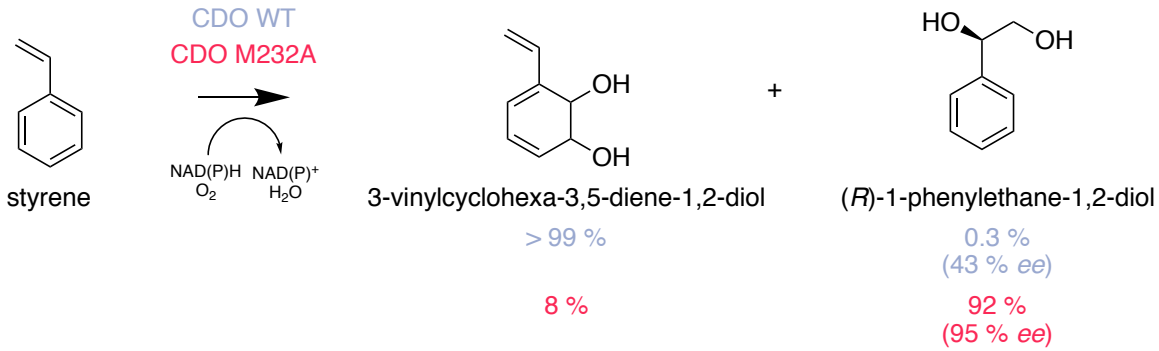

FIGURE 6 - As Model reaction 1 the conversion of styrene to the arene-1,2-dihydrodiol and alkene-1,2-diol has been investigated.

Model reaction 2:

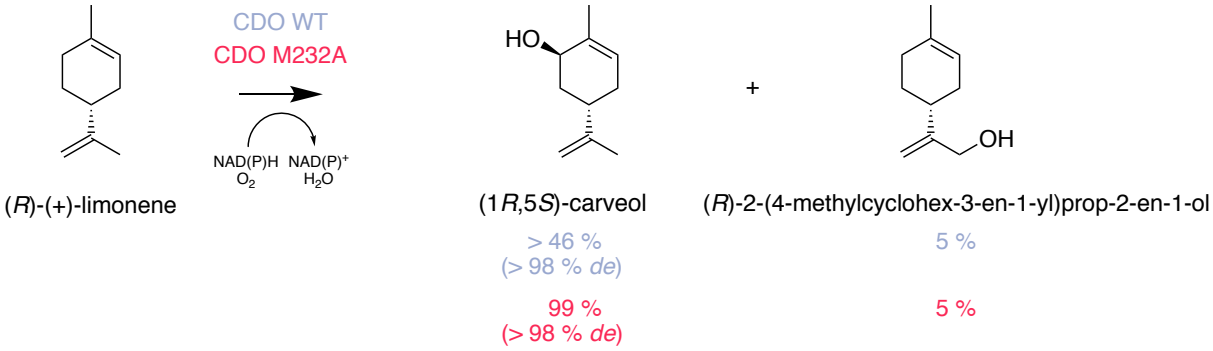

FIGURE 7 - As Model reaction 2 the Conversion of (*R*)-(+)-limonene to (1*R*,5*S*)-carveol and (*R*)-2-(4-methylcyclohex-3-en-1-yl)prop-2-en-1-ol has been investigated.

1.3 Cofactor Regeneration

A major constraint when using oxidoreductases is represented by an efficient cofactor supply. Due to the high cost of reductive cofactors, namely NAD(P)H, different considerations and concepts have been discussed in recent years (Martínez *et al.*, 2017; Dong *et al.*, 2018). Major considerations of cofactor regeneration come in the choice between the use of whole-cells vs. isolated enzymes, as well as, the establishment of cascade reactions to perform cofactor recycling (Duetz, Van Beilen and Witholt, 2001; De Carvalho, 2011; Ricca, Brucher and Schrittwieser, 2011; Schrittwieser *et al.*, 2011; Denard, Hartwig and Zhao, 2013; Oberleitner *et al.*, 2013). Oxidoreductases utilize

different cofactors, in the form of loosely bound nicotinamides (NAD(P)H) or flavins (FAD/FMN) and heme groups, which can be incorporated within the enzyme (De Carvalho, 2011; Gamenara *et al.*, 2012; Dong *et al.*, 2018). These cofactors must be regenerated, since they promote the transfer of hydrogen species, electrons as well as the formation of radical species (Gamenara *et al.*, 2012).

The catalytic activity of oxidoreductases can be directly connected to the supply of cofactors (Gamenara *et al.*, 2012). Using whole-cell biocatalysts, the need for cofactor regeneration is alleviated since the cells have the ability to perform cofactor recycling, for example, the recycling of NADPH using the pentose phosphate pathway and NADH mainly using glycolysis (Schmidt *et al.*, 2015). Notwithstanding, in whole-cell biotransformations a major part of the chemical energy is used up in respiration. Consequently, additional cofactor recycling systems, *e.g.* alcohol dehydrogenases are usually co-expressed to assist in cofactor regeneration, especially for NADPH-dependent enzymatic reactions. In contrast, the use of isolated enzymes demands the supply of external cofactors in stochiometric amounts. Moreover, the use of whole-cell biocatalysts additionally protects the enzyme within the cell environment and diminishes cofactor loss, thus, conserving the stability and activity of the enzyme, which may be reduced in isolated enzyme catalysis. However, the use of whole-cells as catalysts creates numerous challenges compared to isolated enzymes. For example, process engineering requirements given in form of cultivation and downstream processing. Additionally, the whole-cell biocatalysts may perform undesired side-reactions, which need to be controlled or reduced. Furthermore, substrate and product transport through the cell membrane can represent a reaction limiting factor (De Carvalho, 2011; Gamenara *et al.*, 2012; Dong *et al.*, 2018). It has been shown that crude cell extract containing ROs is highly unstable (Catterall and Williams, 1971; Sauber *et al.*, 1977). Catterall and Williams proposed an inactivation of the enzyme in crude extract by molecular oxygen, which can be reactivated through reducing agents like Fe(II) and NADH (Catterall and Williams, 1971). On the other hand, stability can be increased dramatically by purification of the enzyme (Sauber *et al.*, 1977). Sauber *et al.* determined that pyrazon dioxygenase lost its activity in crude cell extract within a day,

with the addition of stabilizing agents, *e.g.* 1,4-dithiothreitol the activity after 3 days storage at 4 °C was still at 90 %, whereas purified enzyme was highly stable at 4 °C (Sauber *et al.*, 1977; De Carvalho, 2011; Gamenara *et al.*, 2012; Dong *et al.*, 2018).

To overcome cofactor regeneration issues, various approaches have been applied in form of enzymatic, chemical, electrochemical and photochemical regeneration (Gamenara *et al.*, 2012). For example, regeneration of a cofactor using an auxiliary substrate, where the cofactor is regenerated, utilizing the same enzyme as used for catalysis. In contrast, enzyme-assisted cofactor regeneration employs a second enzyme as well as an auxiliary substrate. For the regeneration of cofactors using chemical methods, typically molecular hydrogen is used as reducing agent, in combination with a transitional metal catalyst, *e.g.* ruthenium, to facilitate reduction of the cofactor. Electrochemical cofactor regeneration shows a promising alternative, since the supply of redox equivalents is mass free. However, major drawbacks arise due to the specialized equipment required, as well as, cofactor dimerization, due to the high potential needed. Photochemical methods for cofactor recycling utilize light irradiation and a mediator compound to initiate electron transfer from an electron donor to the cofactor. All these cofactor regeneration methods are still predominantly investigated in a research setting and further development is still needed for the establishment of cofactor generation strategies in a general setting (Gamenara *et al.*, 2012).

1.4 Light-driven Biocatalysis

Regarding oxidoreductases, various systems for the photochemical regeneration of redox cofactors have been established (Hollmann *et al.*, 2007; Taglieber *et al.*, 2008; Hemschemeier, Melis and Happe, 2009; Park *et al.*, 2015; Zachos *et al.*, 2015; Adam *et al.*, 2017; Lee *et al.*, 2017, 2018; Zhang and Hollmann, 2018). Photochemical regeneration of cofactors exploits the ability of light irradiation to initiate electron transfer reactions (Gamenara *et al.*, 2012; Lee *et al.*, 2018). This is usually performed with the help of so-called light-active substances, also known as photosensitizers or photomediators. Photosensitizers include dyes (*e.g.* methylene blue, FMN), organometallic compounds (*e.g.*

$[Ru(bpy)_3]^{2+}$) as well as semiconductors (*e.g.* TiO_2, Fe_2O_3). Through light irradiation the photosensitizer is activated (Figure 8). This activation results in electrons reaching higher energy states and thus creating an electron demand. To fill the created electron demand, a sacrificial electron donor is needed, in the form of *e.g.* water, ethylenediaminetetraacetic acid (EDTA) or triethanolamine (TEA). Finally, the photoactivated electron is transferred to the active site of the redox enzyme where the actual catalysis takes place (Gamenara *et al.*, 2012; Lee *et al.*, 2018).

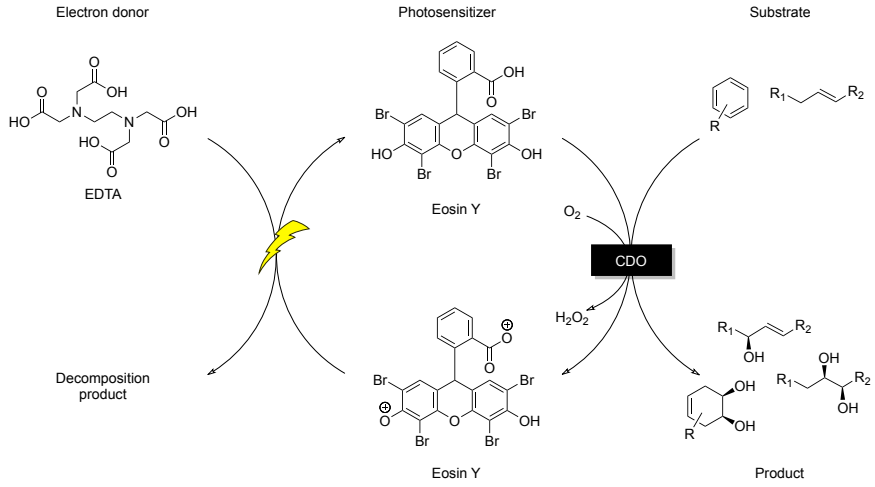

FIGURE 8 – Schematic representation of the photobiocatalytic electron supply from the electron donor EDTA to the photocatalyst EY, which supplies CDO with electrons.

One approach to tackle the cofactor regeneration issue and to eliminate the need for expensive redox cofactors comes in the form of photocatalytic reactions, *e.g.* the light-driven Baeyer-Villiger oxidation of ketones described by Hollmann *et al.* (Hollmann *et al.*, 2007). In this pioneering study, NAD(P)H was replaced as a cofactor with a catalytic cycle utilizing light, a sacrificial electron donor (EDTA) and a flavin (FMN/FAD) (Hollmann *et al.*, 2007). Moreover, Lee *et al.* performed photocatalytic C-C double bond reductions using an ene-reductase (Lee *et al.*, 2017). Adam *et al.* established an *in vitro* photobiocatalytic process for hydrogen production (Adam *et al.*, 2017). Mifsud *et al.* examined the use of water as a sacrificial electron donor in photobiocatalysis (Mifsud *et al.*, 2014). Park *et al.* used eosin Y (EY) as a mediator for photoactivated cytochrome P450 catalysis (Park *et al.*, 2015). Furthermore, Zachos *et al.* describe an *in-situ* photocatalytic method of H_2O_2 generation coupled to a fatty acid decarboxylase, which was used for the

conversion of natural fatty acids into terminal alkenes (Zachos *et al.*, 2015). Apart from Park *et al.*, who performed whole-cell photobiocatalysis with a cytochrome P450 enzyme, all attempts in photobiocatalysis to date were examined as *in vitro* systems (Park *et al.*, 2015). Interestingly, the only other major form of *in vivo* photobiocatalysis is performed by coupling oxidoreductases to the photosynthesis of cyanobacteria (Köninger *et al.*, 2016; Hoschek, Bühler and Schmid, 2017).

1.4.1 Side Product Formation

A common undesired effect of oxidoreductases is the so called uncoupling, which results in side reactions (Holtmann and Hollmann, 2016). For example, molecular oxygen may act as a sink for reducing equivalents, which results in a side reaction in form of H_2O_2 formation. One of the major consequences of uncoupling in biocatalysis is believed to be the formation of radical oxygen species, which influences the stability of the enzyme. Additionally, uncoupling can result in a high consumption of cofactors, resulting in an unnecessary demand of cofactor not being utilized by the target reaction. Uncoupling can be observed in the active site of flavin-dependent as well as heme-dependent monooxygenases. For example, the flavin in flavin-dependent monooxygenases is reduced and reacts with molecular oxygen, which is used by the enzyme for oxygenation. Instead of completing the catalytic cycle, spontaneous uncoupling can occur, resulting in the formation of H_2O_2 (Figure 8). In contrast, heme-dependent monooxygenases follow a different mechanism, where an iron-hydroperoxy complex releases H_2O_2. On the other hand, uncoupling can also result during electron transport chains, *e.g.*, single electron mediators react faster with molecular oxygen, due to the conserved sum of electron spins throughout the reaction. Whereas reactions using a hydride transfer mediator, compromise a change in the sum of electron spins throughout the reaction, resulting in a slower reaction which might be a reason for increased uncoupling (Holtmann and Hollmann, 2016).

Concerning ROs, the type and concentration of the substrate is a factor for the formation of side products, *e.g.* the release of H_2O_2 or other reactive oxygen species (Rivard *et al.*, 2015). Furthermore, ROs can utilize H_2O_2 and substrate for product formation at

decreased rate constants in a so called peroxide shunt reaction (Rivard *et al.*, 2015). Lee showed that O_2 utilization and NADH oxidation by naphthalene dioxygenase (NDO) was partially uncoupled from the substrate oxidation (Neary *et al.*, 2012). Furthermore, up to 50 % of the O_2 utilized was detected as H_2O_2 and had an inhibiting effect on NDO (Neary *et al.*, 2012). Further investigations of the formation/utilization of reactive oxygen species by ROs have to be conducted in order to clarify inhibitory effects or the participation of H_2O_2 in catalysis.

1.5 Thesis Aims

The aim of this thesis was (a) to reduce the complexity of the Rieske oxygenase CDO from *P. fluorescens* IP01, and (b) to establish an *in vitro/vivo* method for the photocatalytic biotransformation of alkenes utilizing CDO from/in recombinant *E. coli* cells. The *in vivo* approach was inspired by the electron transfer system for P450s, as proposed by Park *et al.* (Park *et al.*, 2015). Hence, the goal was to examine the expression of CDO in *E. coli* and to create an engineered variant (CDO M232A), as well as, to provide a proof-of-concept for an alternative cofactor regeneration method *in vitro/vivo*, assisted by light irradiation of photosensitizers which are capable of permeating the cell membrane in whole-cell biotransformations (Figure 9).

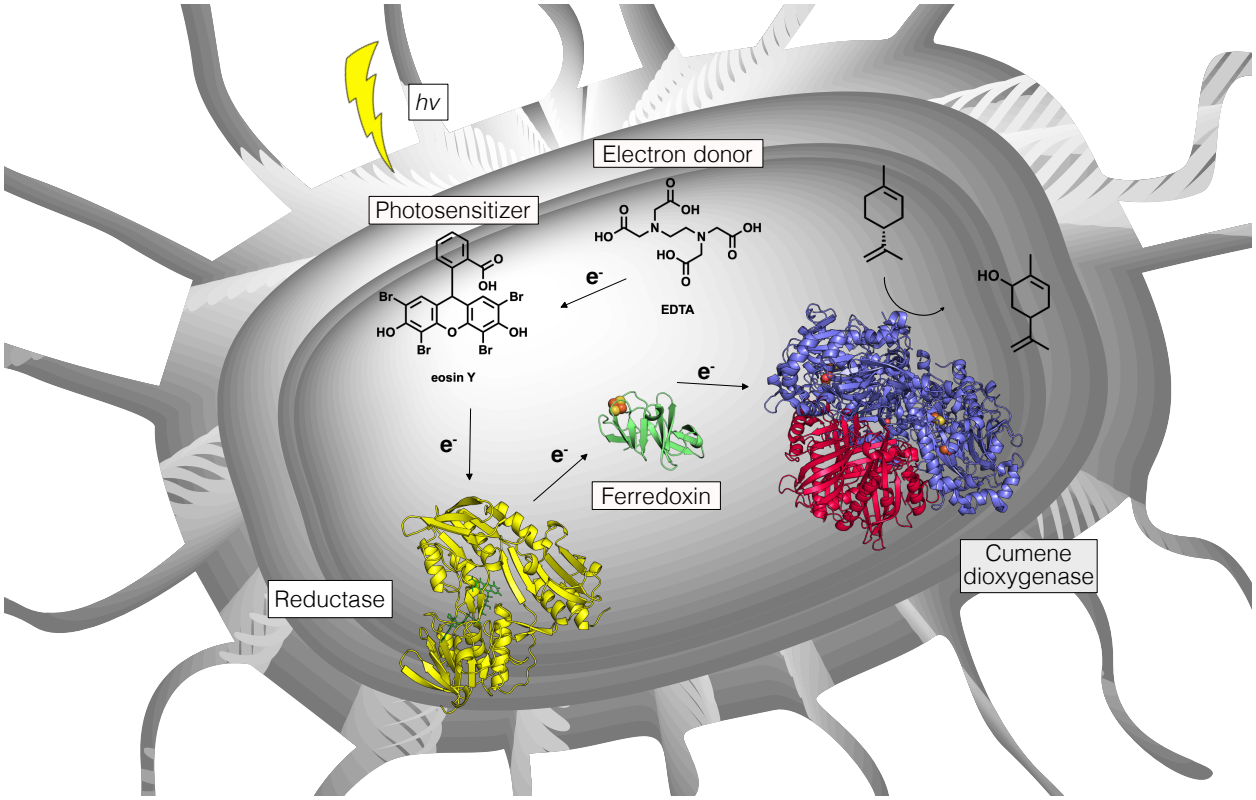

FIGURE 9 – Schematic representation of the proposed *in vivo* photobiocatalytic system using CDO in *E. coli*.

2 RESULTS

2.1 MOLECULAR CLONING OF CONSTRUCTS

A list of all successfully created constructs can be seen in Table 2. Constructs containing the codon-optimized synthetic genes (1-4) were created using restriction/ligation cloning. Constructs 5-16, including the repair of pIP107D, were carried out using Gibson assembly®.

TABLE 2 - Constructs successfully created using standard molecular cloning procedures.

construct	vector	resistance	insert	His-tag
1	pET28a(+)	Km	CumA1	N-term
2	pET28a(+)	Km	CumA2	N-term
3	pET28a(+)	Km	Fd	N-term
4	pET28a(+)	Km	FdR	N-term
5	pETDuet-1	Amp	MCSI: CumA1, CumA2; MCSII: Fd, FdR	-
6	pETDuet-1	Amp	MCSI: CumA1, CumA2; MCSII: Fd	-
7	pETDuet-1	Amp	MCSI: CumA1; MCSII: Fd, FdR	-
8	pETDuet-1	Amp	MCSI: CumA1; MCSII: Fd	-
9	pET28a(+)	Km	CumA1-Fd $(EA_3K)_2$ linker	N-term
10	pETDuet-1	Amp	MCSI: CumA1-Fd $(EA_3K)_2$ linker	N-term
11	pBAD/His A	Amp	CumA1-Fd $(EA_3K)_2$ linker	-
12	pBAD/His A	Amp	CumA1-Fd $(EA_3K)_2$ linker	N-term
13	pBAD/His A	Amp	CumA1-Fd $(EA_3K)_2$ linker	C-term
14	pBAD/His A	Amp	Fd-CumA1 no linker	-
15	pBAD/His A	Amp	Fd-CumA1 $(EA_3K)_2$ linker	-
16	pBAD/His A	Amp	Fd-CumA1 $(G_4S)_2$ linker	-
pIP107D	pUC-based	Amp	CumA1, CumA2, CumA3 and partial CumA4	
pCDO	pUC-based	Amp	CumA1, CumA2, CumA3, CumA4	
pCDOv1	pUC-based	Amp		

2.2 Restriction/Ligation Cloning of Synthetic Genes in pET28a(+)

2.2.1 Amplification of Fd, FdR, CumA1 and CumA2

First, constructs containing the codon-optimized synthetic genes encoding for the four CDO-components containing an N-terminal His-tag for later purification were created. Initially, the amplification of Fd, FdR and CumA1 was performed using Phusion® polymerase in a gradient PCR to investigate different annealing temperatures. After running a 0.75 % agarose gel, only bands for FdR and CumA1 were detected (data not shown). Regarding the annealing temperature, the clearest bands were detected at the temperature calculated by the T_m Calculator tool from Thermo Fischer Scientific, thus subsequent reactions were performed with these calculated annealing temperatures. Using DreamTaq polymerase, Fd was successfully amplified (Figure 10). Since Fd (350 bp) is shorter than FdR (1258 bp) and CumA1 (1401 bp), the following PCR of amplicons (<1000 bp) were performed using DreamTaq polymerase.

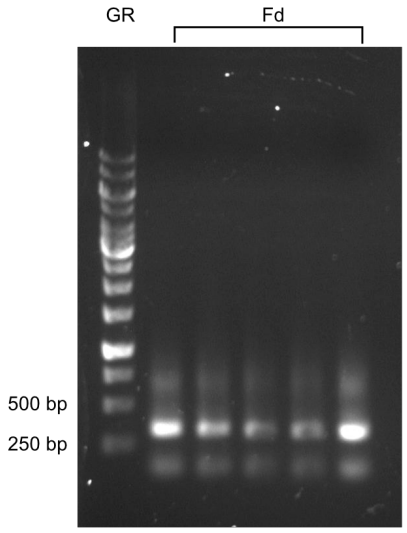

Figure 10 - Control gel of amplified Fd (330 bp) using DreamTaq polymerase at different annealing temperatures. GR = DNA ladder (Generuler™ 1kb DNA ladder).

2.2.2 pET28a(+) constructs containing single genes

After transformation of *E. coli* with the ligated constructs, 450 µL transformation mixture was plated on 4 LB-Km plates, which yielded ~ 20 colonies per plate. 4 colonies per plate were picked for subsequent colony PCR.

2.2.3 Screening using Colony PCR

Colony PCR was performed with 16 colonies picked from plates containing the desired constructs encoding either Fd, FdR or CumA1. For CumA2, 10 colonies were used for colony PCR. Regarding the construct pET28_Fd, 16 hits with an expected size of 623 bp corresponding to the Fd gene were identified *via* the colony PCR. The amplification of FdR resulted in three bands at an expected size of 1556 bp and two bands at ~1000 bp. Regarding CumA1 and CumA2, 13 and 9 hits were detected, respectively. (Figure 11).

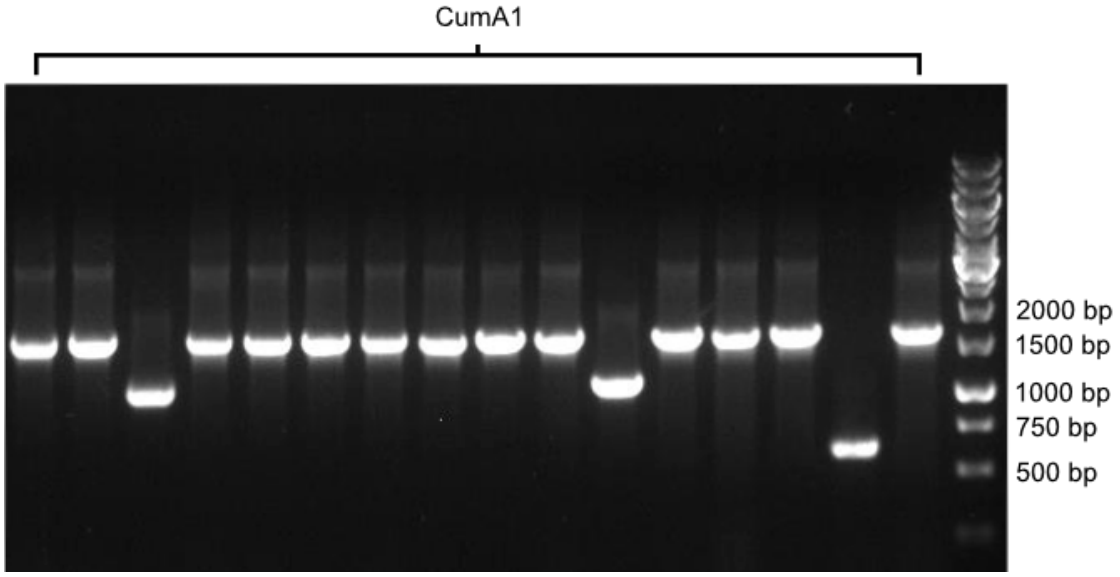

FIGURE 11 - Control gel of Colony PCR amplicons to check construct 1. 16 colonies were picked. 13 *hits* can be detected at the expected size of 1556 bp. DNA ladder (Generuler™ 1kb DNA ladder).

2.2.4 Confirmation of hits

Four hits per gene were sent for sequencing using a primer which binds to the T7 promoter at the start of the multiple cloning site (MCS). In Benchling, multiple sequence alignments were created using MAFFT (Katoh and Standley, 2013). As template, the assembled construct was aligned with the sequencing results as seen in Figure 12. For each sequencing result, at least one out of four matches has been achieved. In general, Sanger sequencing was able to create sufficient results for all constructs, but per sequencing result ~2 nucleotides were mismatched, which might indicate a point mutation, but most likely this is due to the quality of the Sanger sequencing. For further experiments, hits which showed no mismatches were used.

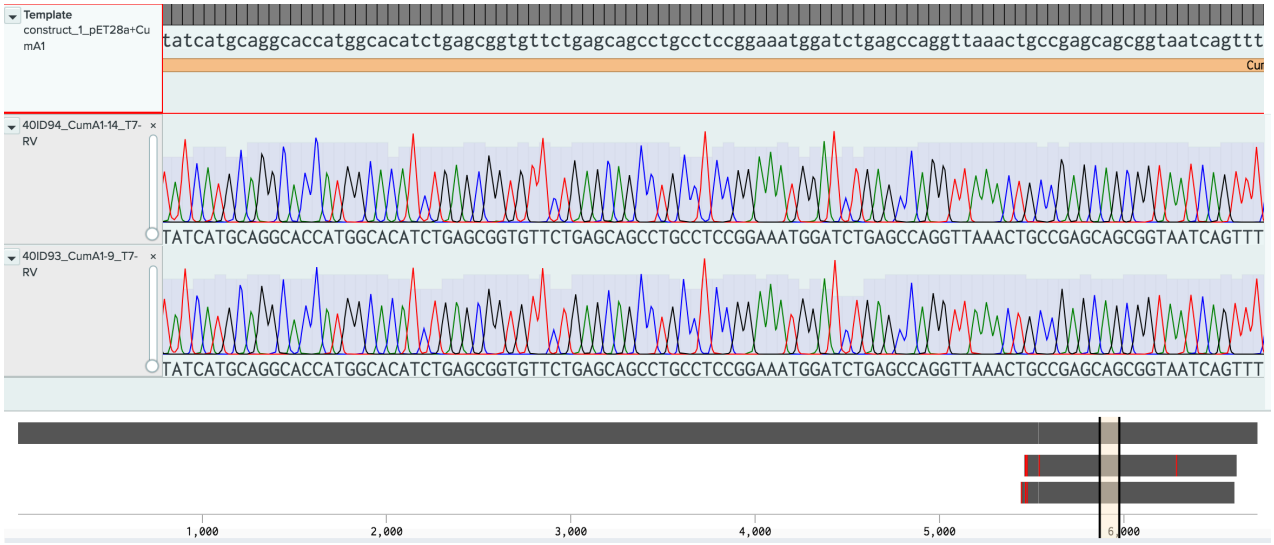

FIGURE 12 - Multiple alignment of construct 1 and sequencing results, using MAFFT v7. Image created using Benchling.

2.3 Gibson Assembly® of Co-expression and Fusion Protein Constructs

For Gibson assembly®, primers were designed which contain ~39 nt overhang complementary between the fragments and ~20 nt for binding to the template (Figure 13). Regarding the pETDuet constructs, a spacer containing a ribosome binding site (RBS) was introduced between genes within the MCSs (Figure 13). The Gibson assembly® fragments were amplified using either DreamTaq or Phusion® polymerase, as described previously. After amplification, the fragments were further processed using two different routes, (a) preparative agarose gel electrophoresis followed by a gel extraction step or, (b) PCR cleanup and fragment size confirmation using an agarose gel. Up to 3 fragments were successfully assembled in one reaction by using this approach. If a construct required more than the assembly of 3 fragments, subsequent assemblies were performed. After transforming chemically competent *E. coli* cells (TOP10/MachI) with the assembly mix, grown colonies were examined using colony PCR and sequencing. Constructs 5-16 were successfully created and confirmed by Sanger sequencing.

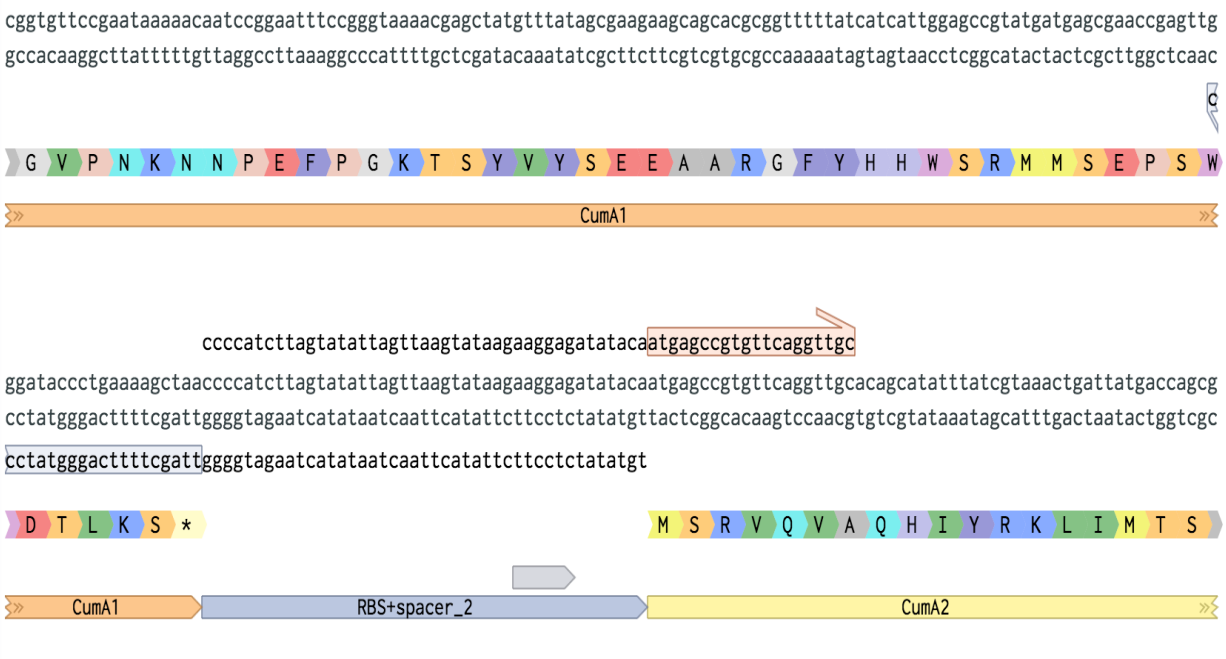

FIGURE 13 - Construct 5: pETDuet + with all genes (MCSI: Fd, FdR MCSII: CumA1, CumA2). Image created using Benchling.

2.4 Reconstruction of Plasmid Encoding CDO Genes

The plasmid pIP107D encoding partially the locus containing all native CDO genes was obtained from Hideaki Nojiri (Tokyo, Japan). The construct contained CumA1, CumA2, CumA3 and partially CumA4 (Figure 14). Since the FdR (CumA4) was missing 433 bp, the construct was repaired using the Gibson assembly®. To obtain the full-length gene of CumA4, the synthetic native gene was ordered and used as the template for the amplification of the insert. As backbone, pIP107D was used. After successful PCR cleanup and assembly, *E. coli* TOP10 cells were transformed with the PCR mix. Afterwards, the correct insertion of the full-length FdR gene into the plasmid was confirmed by sequencing. To confirm the entire construct, primer walking was used to assist in sequencing.

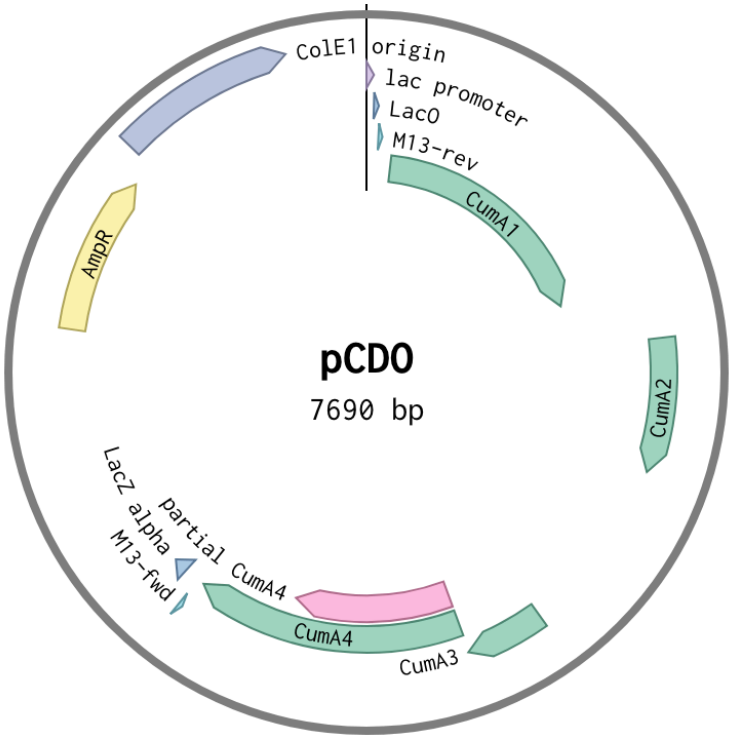

FIGURE 14 -pCDO Construct containing all native CDO genes, vector map created using Benchling.

2.5 GENERATION OF CUMA1 VARIANT M232A

The successful sequencing of pCDO revealed a point mutation in the gene encoding CumA1 resulting in variant V205G. This point mutation was repaired by performing a QuikChange™. Additionally, a QuikChange™ was conducted to create the CumA1 variant M232A, which was previously reported by Gally *et al.* to increase the regio- and stereoselectivity of the CDO (Gally, Nestl and Hauer, 2015). Both mutations were successfully created and confirmed by sequencing.

2.6 Heterologous Protein expression of CDO

2.6.1 Expression of Single Components of CDO

Initial protein expression studies of the created constructs, harboring single components of CDO (Construct 1-4), were investigated using *E. coli* BL21(DE3) as host organism. The expected molecular weights of each protein can be seen in Table 3.

TABLE 3 - Molecular weights of Fd, FdR, CumA1 and CumA2.

component	molecular weight [kDa]
ferredoxin	15.3
cumene dioxygenase β-subunit	26.9
ferredoxin reductase	47.9
cumene dioxygenase α-subunit	55.8

Ferredoxin was detected in the insoluble fraction when performing expression in TB and LB medium (Figure 15, left: expression in TB, right: expression in LB). For FdR, no clear bands could be detected in either experiment (Figure 16). Protein bands at 47 kDA are visible, however, they already occur at t_{0h} which indicates that they are most probably corresponding to *E. coli*-own proteins. It has been previously described that only very weak bands have been detected after the expression of Fd and FdR in *E. coli*, which coincide with our results (Gally, 2016).

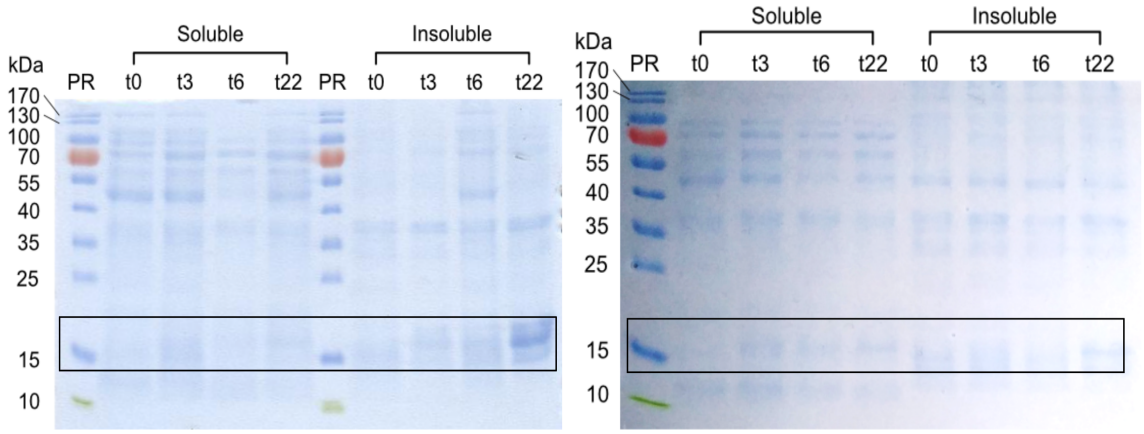

FIGURE 15 - SDS-PAGE of Fd expressed in *E. coli* BL21(DE3) harboring construct 3. Expression in TB is shown left and in LB medium right (Fd MW=15.3 kDA). (t0-t22) represent samples taken at 0, 3, 6 and 22 hours after induction. Protein standard: (PR) PageRuler™ Prestained Protein Ladder (Thermo Scientific™).

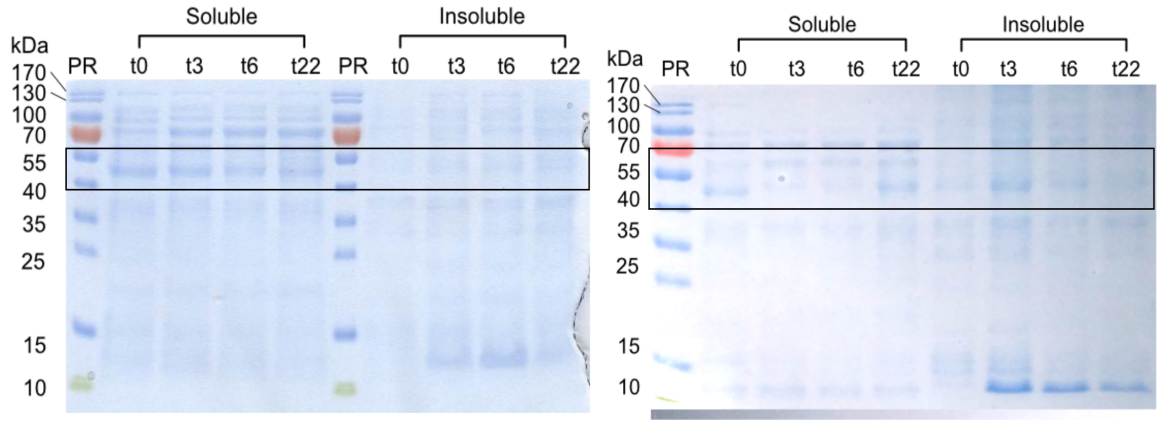

FIGURE 16 - SDS-PAGE of FdR expression in *E.coli* BL21(DE3) harboring construct 4. Expression in TB is shown left and in LB medium right (FdR MW=47.9 kDa). (PR) PageRuler™ (t0-t22) represent samples taken at 0, 3, 6 and 22 hours after induction. Protein standard: (PR) PageRuler™ Prestained Protein Ladder (Thermo Scientific™).

The detection of CumA1 in the insoluble fraction, after expression in TB/LB, indicates inclusion body formation (Figure 17). CumA1 contains a disulfide bridge which could lead to incorrect folding of the protein in *E. coli* BL21(DE3) (Dong *et al.*, 2005). CumA2 was detected in the soluble fraction (Figure 18). Moreover, constructs 1 to 4 have an N-terminal tag attached, which might also influence the correct folding of the proteins (Figure 19). The tag contains 6 x His, a thrombin site and a T7 tag.

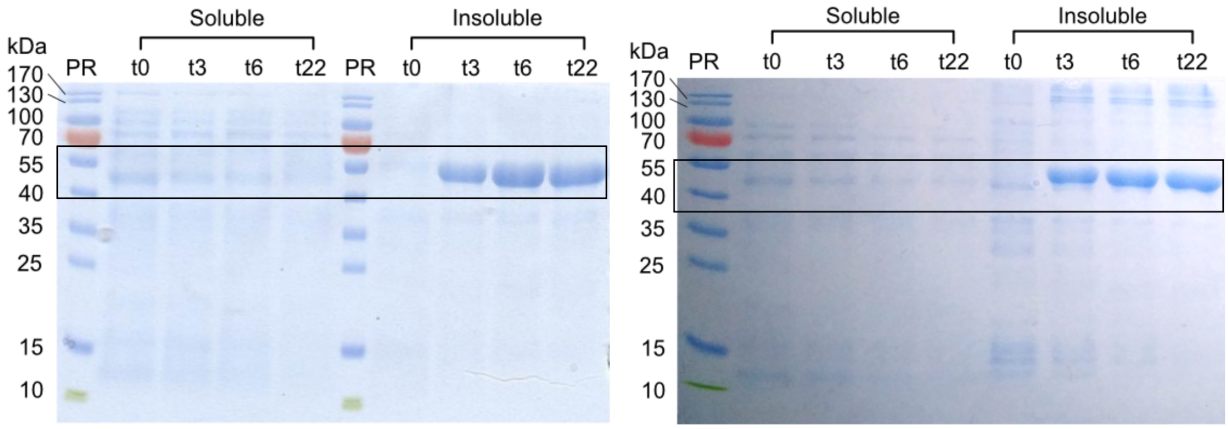

FIGURE 17 - SDS-PAGE of CumA1 expression in *E.coli* BL21(DE3) harboring construct 1. Expression in TB is shown left and in LB medium right (CumA1 MW=55.8 kDa). (t0-t22) represent samples taken at 0, 3, 6 and 22 hours after induction. Protein standard: (PR) PageRuler™ Prestained Protein Ladder (Thermo Scientific™).

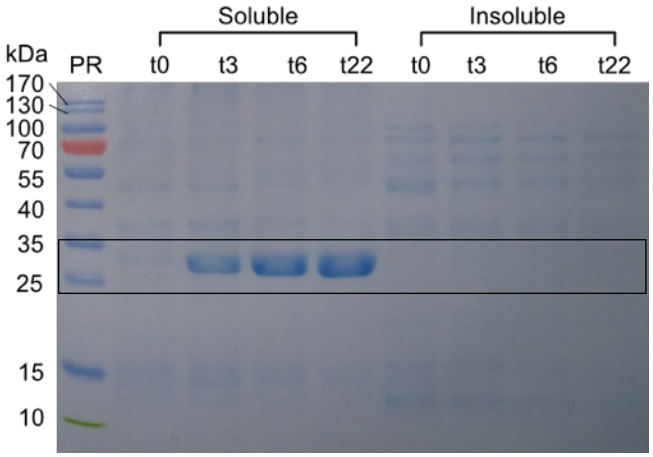

FIGURE 18 - SDS-PAGE of CumA2 expression in *E. coli* BL21(DE3) harboring construct 2 using LB medium (CumA2 MW=26.9 kDa). (t0-t22) represent samples taken at 0, 3, 6 and 22 hours after induction. Protein standard: (PR) PageRuler™ Prestained Protein Ladder (Thermo Scientific™).

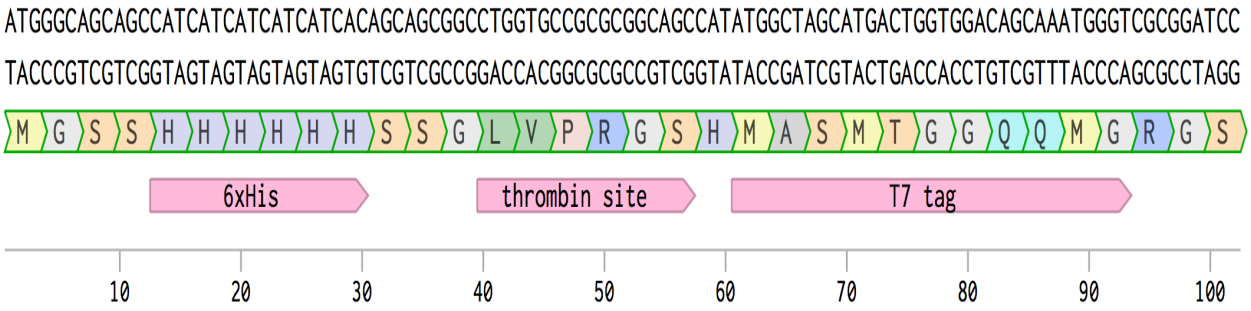

FIGURE 19 - Sequence of N-terminal protein tag. Image created using Benchling.

2.6.2 Heterologous Protein Expression of Co-expression and Fusion Protein Constructs in *E. coli* SHuffle

Since CumA1, Fd and FdR were detected in the insoluble fraction and CumA1 contains a disulfide bridge, co-expression constructs (5-8) were examined by expression of the proteins in *E. coli* SHuffle (see Appendix E). *E. coli* SHuffle is a strain modified by the integration of a disulfide bond isomerase (DsbC) into the genome, to assist in posttranslational disulfide bond formation of recombinant proteins expressed in *E. coli* (Lobstein *et al.*, 2012). Overall, the expression of the proteins encoded in constructs 5-8 in *E. coli* SHuffle was very low to non-detectable. Faint bands corresponding to the desired proteins can be detected for constructs 5 to 8. In contrast, no bands for constructs

containing the fusion protein CumA1-Fd (Constructs 9, 11-13) could be detected. Therefore, the addition of $FeSO_4$ and a later induction time (at an OD_{600} of 1.2) were examined to optimize expression, which did not result in an increased expression level.

Additionally, expression was examined using a pBAD/HisA vector containing CumA1-Fd with and without N-terminal His-tag (Constructs 11-13). Constructs 11-13 contain an arabinose inducible promotor (P_{BAD}), which is tightly regulatable and can reduce inclusion body formation (Guzman *et al.*, 1995). The expression was performed in *E. coli* BL21(DE3) and *E. coli* SHuffle, respectively. Regarding both strains and constructs, a large band was detected in the insoluble fraction.

2.6.3 Chaperone Assisted Heterologous Expression in *E. coli* BL21(DE3)

The expression of CumA1-Fd present in constructs 11-13 was further examined by co-expressing different chaperones to decrease and circumvent, respectively, inclusion body formation. CumA1-Fd was successfully expressed in soluble form by the co-expression of plasmids harboring the chaperones GroEl/GroES (Figure 20, Appendix E). In total, five different plasmids harboring chaperones were investigated for increased yield of soluble protein.

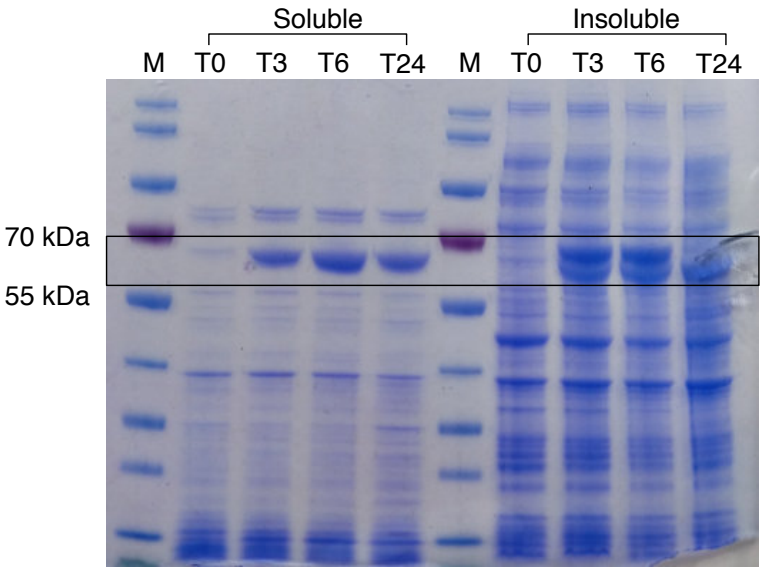

FIGURE 20 - Expression of construct 11 in *E. coli* BL21(DE3), with co-expression of groES-groEL. A band representing CumA1-Fd with MW= 68.5 kDA can be detected in the Soluble fraction 3 hours after induction. Protein standard: (PR) PageRuler™ Prestained Protein Ladder (Thermo Scientific™).

2.6.4 Heterologous Expression and Activity Determination of CDO in *E. coli* JM109

Initially, the implementation of *E. coli* BL21(DE3) for high level recombinant expression of CDO was investigated. Previous examples of recombinant expression of ROs for *e.g.* structural investigation and biocatalysis, were carried out in *E. coli* JM109 (Suenaga, Goto and Furukawa, 2001; Wolfe *et al.*, 2001; Neary *et al.*, 2012). Moreover, it has been shown that *E. coli* JM109 harboring CDO was successfully used for the asymmetric dihydroxylation of olefins (Gally, Nestl and Hauer, 2015). Since *E. coli* BL21(DE3) harboring CDO showed no catalytic activity and most of the expressed protein was detected as inclusion bodies, the use of *E. coli* JM109 was examined for the recombinant expression of CDO. Therefore, the expression of CDO in *E. coli* JM109 harboring pCDOv1 was examined (Figure 21). After optimizing the culture conditions, initial growth was performed in TB medium at 37 °C and expression was subsequently performed at 30 °C. The SDS-PAGE analysis revealed weak bands corresponding to CumA1 M232A and CumA2. Fd and FdR could not be detected by SDS-PAGE. However, *E. coli* JM109 colonies harboring pCDOv1 showed activity when exposed to indole during the solid phase colorimetric assay (Figure 22). *E. coli* JM109 harboring pUC118 (empty vector control) did not show any indigo formation after more than 4 hours. The proposed reaction can be seen in Figure 23. Indole is converted to indoxyl by CDO, through the spontaneous dimerization of indoxyl, indigo is formed. Similarly, liquid cultures of *E. coli* expressing CDO show an indigo coloration. This indigo formation is suggested to be facilitated through the indole generation of the *E. coli* specific tryptophanase, which catalyzes the hydrolysis of tryptophan to indole, pyruvate and ammonia (Wackett, 2002; Li and Young, 2013).

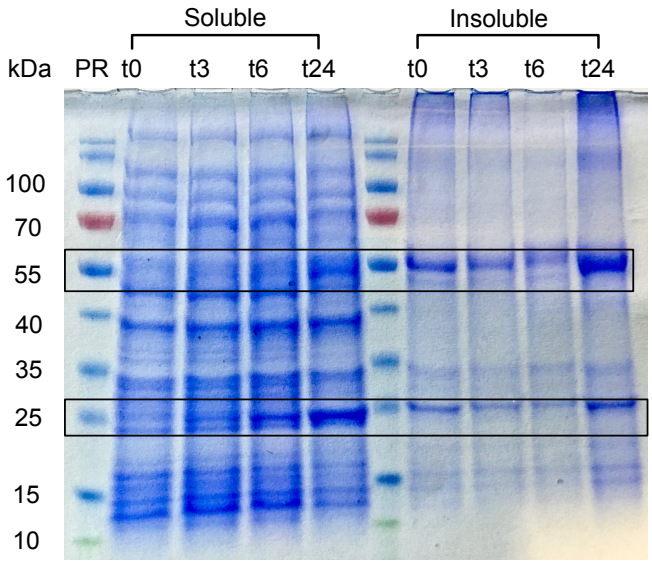

FIGURE 21 - SDS-PAGE of *E. coli* JM109 harboring CDO M232A. weak bands corresponding to CumA1 (55.8 kDA) and CumA2 (26.9 kDa) can be detected. No bands representing Fd and FdR can be found. Protein standard: (PR) PageRuler™ Prestained Protein Ladder (Thermo Scientific™).

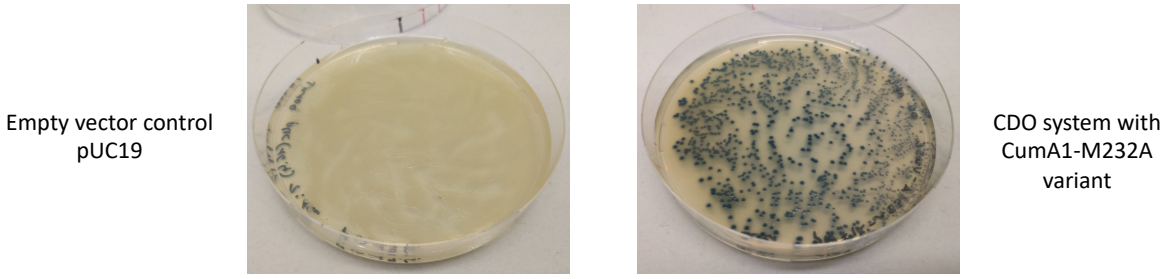

FIGURE 22 - Solid phase colorimetric assay based on indigo formation used to determine the activity of *E. coli* cells harboring CDO. Left: empty vector control showing no indigo formation. Right: *E. coli* JM109 colonies harboring pCDOv1 show indigo formation.

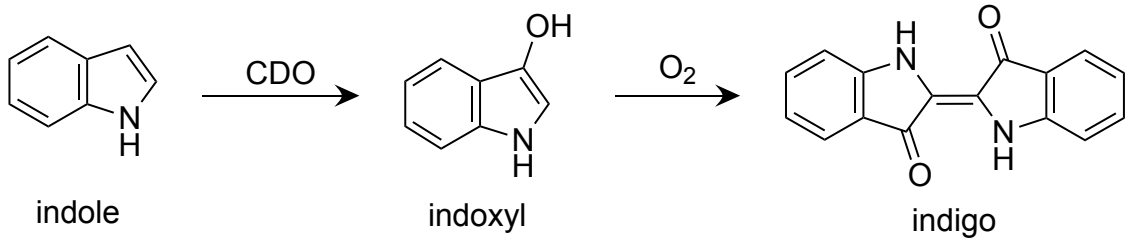

FIGURE 23 - Reaction scheme of indigo formation by *E. coli* cells harboring CDO. Through the hydroxylation of indole, indoxyl is formed which undergoes spontaneous dimerization under aerobic conditions.

2.7 Growth And Activity Determination of *E. coli* Harboring CDO

As mentioned previously, expression studies were performed using the disulfide bond promoting *E. coli* strain SHuffle. Since expression of constructs 5-9 in *E. coli* SHuffle was low to non-detectable, the growth of *E. coli* SHuffle during expression of constructs was examined and compared to the growth of *E. coli* BL21(DE3) during expression of the respective constructs (Figure 24). *E. coli* SHuffle shows a significantly reduced growth, reaching a stationary phase after ~ 9 h (OD_{600} = 3.5-3.9). After 24 hours of growth, *E. coli* SHuffle reached an OD_{600} of 4.3-4.9. *E. coli* BL21(DE3) harboring the equivalent constructs showed a 2-fold higher growth rate than *E. coli* Shuffle, leading to a final OD_{600} of 8-10 after 24 hours.

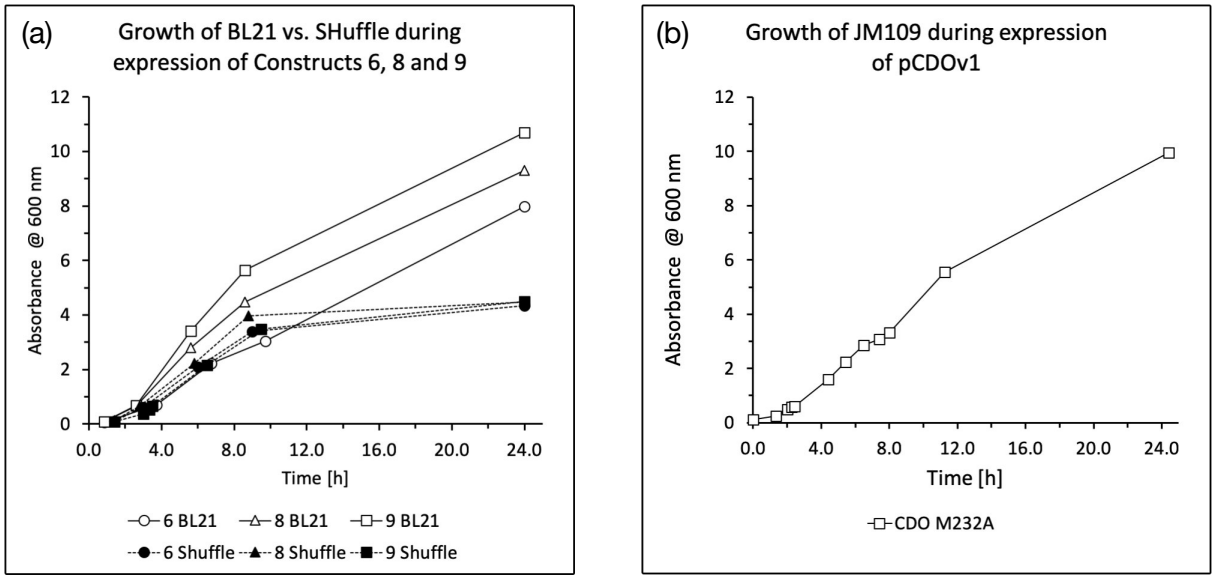

FIGURE 24 - Growth curves of *E. coli* during expression of CDO constructs in TB medium at 30°C. Induction was carried out at an OD_{600}=0.5-0.8. (a) Investigation of *E. coli* BL21(DE3) vs SHuffle harboring constructs 6-9. *E. coli* Shuffle shows a decreased growth, reaching a stationary phase after ~9h and a final OD_{600} of ~4.6. (b) shows the growth of *E. coli* JM109 harboring pCDOv1.

Initially, each expression batch of CDO M232A showed a high variation of indigo formation, which was later determined to be a contamination of cells harboring the empty vector control. After this contamination was removed, activity of the *E. coli* JM109 cells containing overexpressed CDO M232A was further investigated by using different growth media (Figure 25). LB, TB and the autoinduction medium ZYP-5052 were examined. After overexpression of CDO M232A was finished, cells were prepared for whole-cell

biotransformation of (*R*)-(+)-limonene (Figure 7) using D-glucose as substrate for the upkeep of cellular reducing agents (cofactor regeneration). As expected, the highest product formation was obtained by growing the cells in TB medium resulting in approximately 2.5 mM of (1*R*, 5*S*)-carveol at a cell concentration of 25 g_{CWW}/L after 24 hours. Increasing the catalyst concentration does not increase the product formation, which could be due to the cell toxicity of carveol, shift in pH due to higher cell concentration or the biphasic nature of the system (hydrophobic substrate). Furthermore, a possible limiting factor could be O_2, but also the formation of H_2O_2 *via* uncoupling of the reaction could be a key factor in loss of activity.

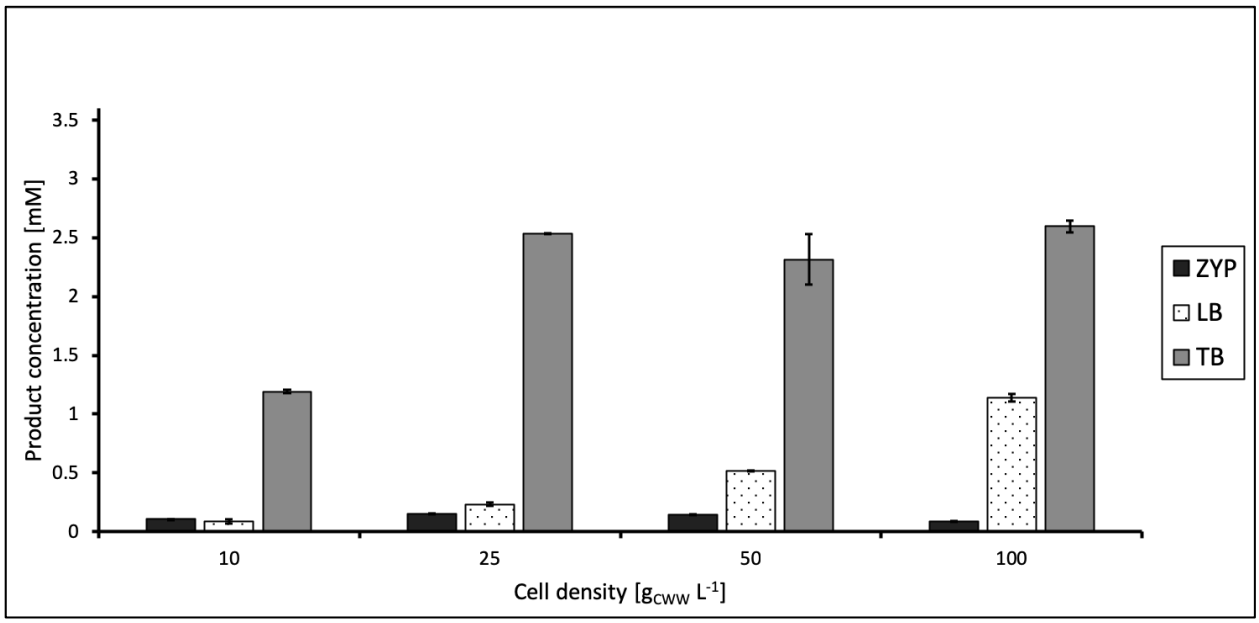

FIGURE 25 - Comparison of the (1*R*,5*S*)-carveol formation after 24 h in D-glucose -supplemented *in vivo* biotransformations using 10 mM (*R*)-(+)-limonene as substrate. *E. coli* JM109 cells have been used after the expression of CDO M232 in different media for 20 hours.

The specific activity of CDO M232A was determined in a kinetic experiment (Figure 26). In the linear phase of the reaction, a specific activity of 0.034 U/mg_{CWW} (1-6h) could be achieved. After 18 hours of reaction, no further product formation was observed, which might indicate a loss of activity due to the instability of the catalyst. CDO may be effected by a shift in pH due to acetate formation of *E. coli* (Potuzak *et al.*, 2008). Furthermore, it has been determined that carveol concentrations over 5 mM can act toxic on *E. coli* JM109 cells, which may explain the loss of activity after 18 h (Gally, 2016).

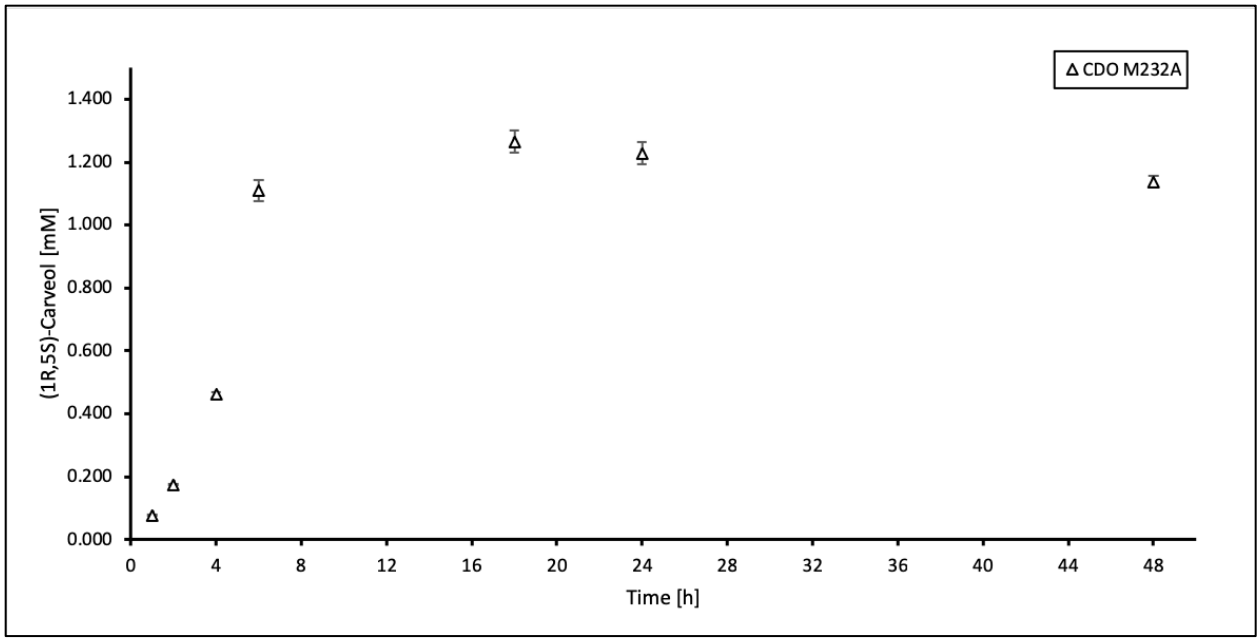

FIGURE 26 – Product formation of the whole-cell biotransformation of (*R*)-(+)-limonene to (1*R*,5*S*)-carveol catalyzed by CDO M232A. Reaction conditions: 100 g_{CWW}/L, 10 mM substrate, 20 mM D-glucose at 30 °C. Time points were taken after 1, 2, 4, 6, 18, 24 and 48 hours. The activity was calculated for the linear phase 1-6 h (specific activity = 0.034 U/mg_{CWW}).

2.8 LIGHT-DRIVEN BIOCONVERSION OF STYRENE AND (*R*)-(+)-LIMONENE

2.8.1 GENERAL SETUP

Table 4 shows a summary of the performed light-driven reactions. *In vitro* photocatalytic reactions were investigated by applying the combination CFE/FMN/EDTA. The CFE was prepared from *E. coli* BL21(DE3) harboring constructs containing codon-optimized CDO components and fusion protein variations (constructs 5-13). *In vivo* light-driven biotransformations were investigated with whole-cells or lyophilized cells as catalyst, FMN/EY/RB as photosensitizer and EDTA/TEA as electron donor, respectively.

TABLE 4 – Light-driven reaction setups.

function	component	final concentration
catalyst	cell-free extract	250 μL/mL
	whole-cells	10-200 g_{CWW}/L
	lyophilized cells	5 mg/mL
photosensitizer	FMN	0.1 mM
	EY	
	RB	
electron donor	EDTA	5 mM
	TEA	
substrate	styrene	10 mM
	(*R*)-(+)-limonene	
optionally:	catalase	1 mg/mL

Throughout this thesis, different light reactor concepts were established for the light-driven bioconversions. The initial *in vitro* photobiocatalytic reactions were performed using the light reactor concept depicted in Figure 27 A. As photobioreactor, a water bath lined with LED strips on a heated magnetic stirrer plate was setup. *In vitro* photobiocatalytic reactions were performed in 4 mL vials with a reaction volume of 1 mL, resulting in a 3 mL headspace for oxygen supply. To ensure that oxygen was not a limiting factor, commercially available balloons filled with pure O_2 were attached using a syringe and vial caps containing a membrane. Due to the high volatility of the used substrates, evaporation was a major problem and led to a non-closed mass balance of the reaction components after catalysis. Thus, a 3D printed light-reactor, capable of carrying 20 mL vials, was designed and built (Figure 27 B, C). At a final reaction volume of 1-1.5 mL, the resulting increased headspace (18.5-19 mL) was deemed appropriate for O_2 supply. The 3D printed light-reactor was constructed out of PLA and lined with LED strips. During catalysis, the reactor was placed in an incubation shaker to provide constant temperature and shaking.

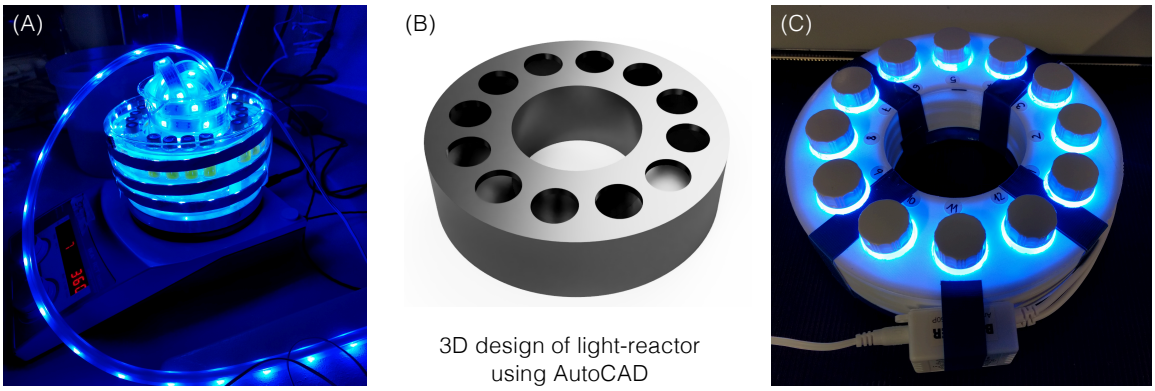

FIGURE 27 - Different light reactor concepts: (A) initial light reactor setup: water bath lined with LED strips and a 3D-printed 4 mL glass vial rack. (B) 3D concept of light reactor, made with AutoCAD. (C) Final 3D-printed light reactor holding 20 mL vials and lined with led strips.

2.8.2 *IN VITRO* PHOTOBIOCATALYSIS USING CFE

Initially, the photobiocatalytic conversion of styrene to 3-vinylcyclohexa-3,5-diene-1,2-diol and 1-phenyl-1,2-ethanediol catalyzed by the CDO WT was examined. Reactions were performed by utilizing CFE of constructs 5 to 8 (which harbor different combinations of the CDO components) expressed in *E. coli* BL21(DE3). The light-reactor setup used for the initial reactions can be seen in Figure 27. No product formation was detected with the combination of FMN as photosensitizer and EDTA as electron donor using CFE. Furthermore, no product formation was observed for CFE containing the fusion proteins of CumA1 and Fd (CumA1-Fd/Fd-CumA1). All other photosensitizer and electron donors, respectively, were not investigated at this time.

2.8.3 LIGHT-DRIVEN *IN VIVO* BIOTRANSFORMATION OF (*R*)-(+)-LIMONENE

Since no product formation was detected for the *in vitro* photobiocatalytic conversion of styrene by using CFE containing CDO and no product standard for 3-vinylcyclohexa-3,5-diene-1,2-diol was commercially available, further photobiocatalytic reactions have been conducted for the conversion of (*R*)-(+)-limonene to (1*R*,5*S*)-carveol catalyzed by CDO M232A. Thus, the plasmid containing the native genes of CDO (pIP107D) was repaired and the CumA1 M232A variant was created to increase enantioselectivity. During the repair of pIP107D, a solid phase colorimetric assay based on

indigo formation was used to confirm the activity of *E. coli* cells harboring CDO (Figure 22). Due to the successful whole-cell biotransformation of (*R*)-(+)-limonene with *E. coli* JM109 containing overexpressed CDO further investigations of a light-driven whole-cell approach were applied using *E. coli* JM109 with native genes.

Three photosensitizers were tested for the biotransformation of (*R*)-(+)-limonene, namely, FMN, EY and RB. As electron donor, TEA and EDTA were investigated. Quantitative detection was performed on a chiral column (Hydrodex-β-6TBDM). To verify the activity of CDO M232, control reactions were performed in parallel to each light-driven reaction by glucose supplementation showing the maximum amount of (1*R*,5*S*)- and (1*S*,5*S*)-carveol which can be obtained from this batch of whole-cell catalysts. Therefore, glucose supplemented reactions were examined using GC-FID, as seen in Figure 28.

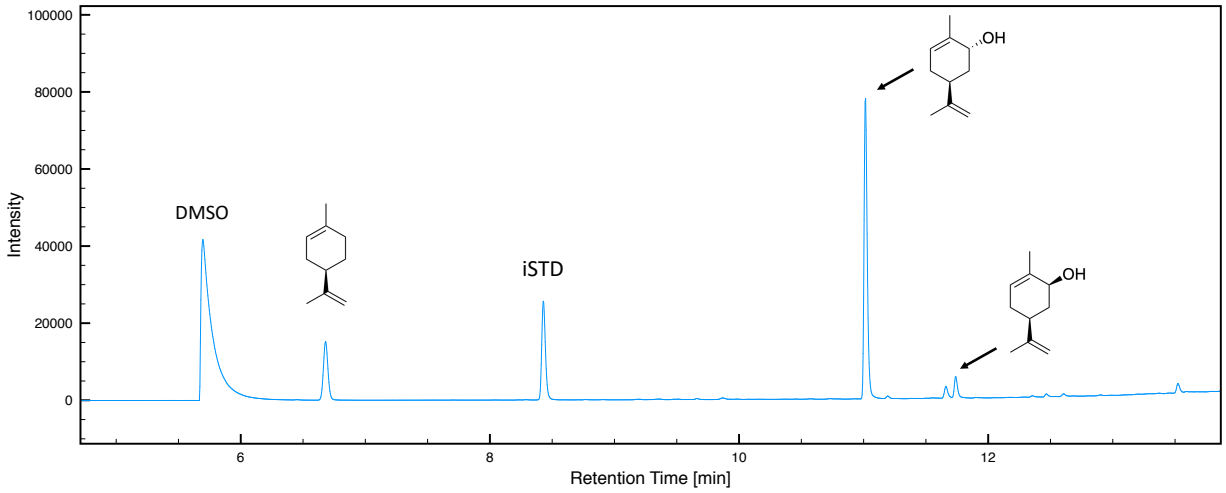

FIGURE 28 - GC-FID (chiral) chromatogram showing the detection of (*R*)-(+)-limonene and carveol after 24 h of whole-cell biotransformation using *E. coli* JM109 harboring CDO M232A with D-glucose supplementation. In total, a conversion of 26 % corresponding to 2.6 mM (1*R*,5*S*)-carveol was achieved.

Due to the highly insoluble substrate, the addition of DMSO as co-solvent to the reaction mixture was investigated, which showed no effects for glucose supplemented reactions, but resulted in additional decomposition products in light-driven reactions. After extensive examination of the *in vivo* photobiocatalytic cofactor regeneration for CDO, the first successful light-driven whole-cell biotransformation was achieved using EY/EDTA and RB/EDTA. The highest achieved product formation by CDO M232 in control reactions (D-glucose supplemented) was 2.6 mM (1*R*,5*S*)-carveol (*ee* >86 %) after 24 hours. For

light-driven CDO M232A reactions, 86 μM (1*R*,5*S*)-carveol (*ee* >99 %) was formed with EDTA/EY and 52 μM (*ee* >99 %) with EDTA/RB (Table 5). Control reactions without photosensitizer, electron donor or biocatalyst showed no product formation. The proposed *ee* of >99 % for (1*R*,5*S*)-carveol needs to be further examined, since very low amounts of product were formed, and (1*S*,5*S*)-carveol might be present, but under the detection limit of the applied GC-FID method.

TABLE 5 -Highest formation of (1*R*,5*S*)-carveol after 24h biotransformation in D-glucose supplemented reactions and light-driven reactions using *E. coli* JM109 harboring CDO M232A.

catalyst	cofactor	concentration [mM]
whole-cells (CDO M232A, 100 g_{CWW}/L)	D-glucose [a]	2.646 (*ee* 86 %)
	EDTA[b]/EY[c]	0.086 (*ee* >99 %)
	EDTA[b]/RB[c]	0.052 (*ee* >99 %)

[a] conc. D-glucose: 20 mM
[b] conc. EDTA: 5 mM
[c] conc. photosensitizer: 0.1 mM

Figure 29 shows the detection of (1*R*,5*S*)-carveol formation after 24 h in light-driven biotransformations with EY/EDTA. As only a small amount of (1*R*,5*S*)-carveol is formed, no peak corresponding to (1*S*,5*S*)-carveol could be detected since it is probably under the detection limit, as discussed previously. To examine the applicability of lyophilized whole-cells, cells expressing CDO were lyophilized and light-driven reactions were setup as described earlier. No product formation could be detected with lyophilized cells.

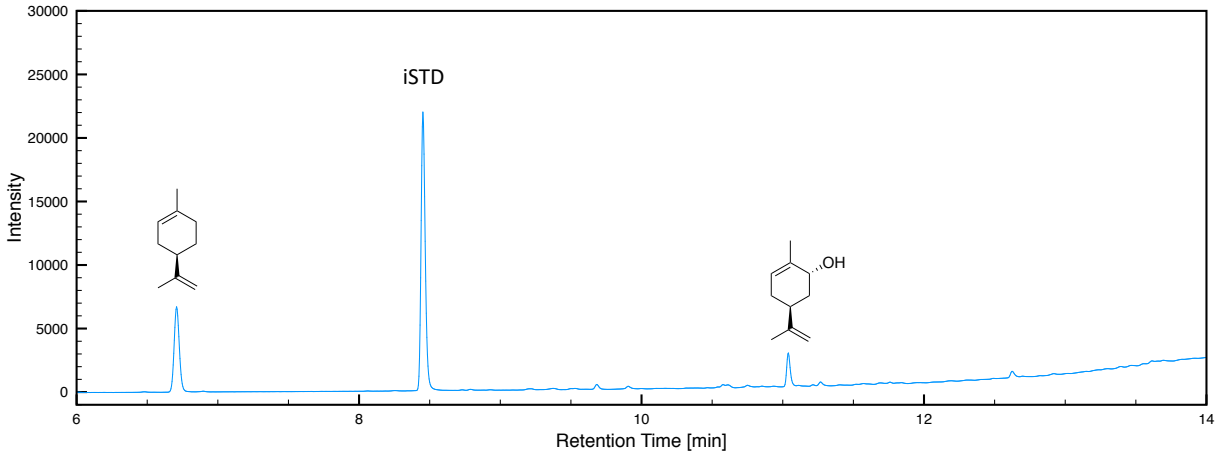

FIGURE 29 - GC-FID (chiral) chromatogram showing the detection of (*R*)-(+)-limonene and (1*R*,5*S*)-carveol after 24 h of light-driven whole-cell biotransformation using *E. coli* JM109 harboring CDO M232A with EY and EDTA. In total, a conversion of 0.9 % corresponding to 86 μM (1*R*,5*S*)-carveol was achieved.

Since only (-)-carveol (mixture of isomers) was commercially available as a standard for quantitative analysis, qualitative confirmation was performed using GC-MS (chromatograms can be found in Appendix F). A similarity search of the corresponding peaks at 4.25 min (determined at a probability of 92 %) revealed that the target was carveol (Figure 30). The formation of the desired product (1*R*,5*S*)-carveol was finally confirmed by chiral GC-FID analysis.

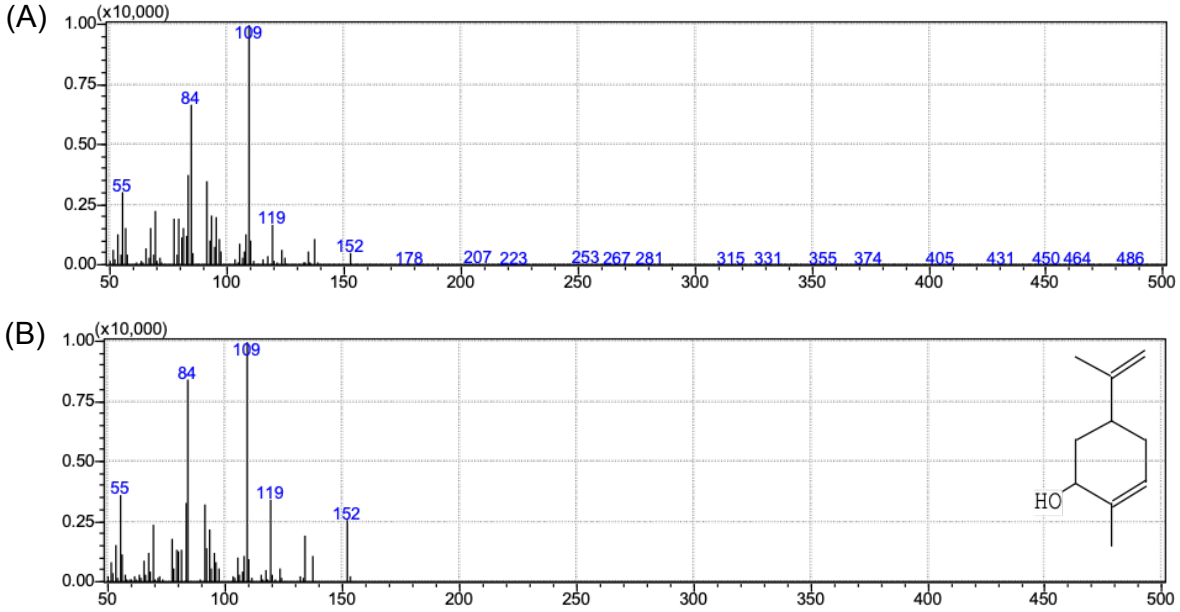

FIGURE 30 – (A) Mass spectrum of the target peak detected at ~4.25 min corresponding to (1*R*-5*S*)-carveol. (B) Mass spectrum of *trans*-carveol obtained after performing a similarity search, resulting in a similarity of 92% towards the mass spectrum of the target peak.

After successful proof-of-concept of the light-driven *in vivo* reactions, reaction rates of whole-cell biotransformations with and without DMSO have been recorded. Figure 31 shows the formation of (1*R*,5*S*)-carveol within 24 hours. Although reactions containing DMSO show in general a higher product formation than reactions without DMSO, the obtained results are not consistent since both studies were performed in different batches. Moreover, a high variation of activity was encountered between the batches. In addition, it was observed that the product formation did not increase after one hour of reaction, indicating that more time points directly after starting the reaction must be taken. Due to time constraints this could not be evaluated further.

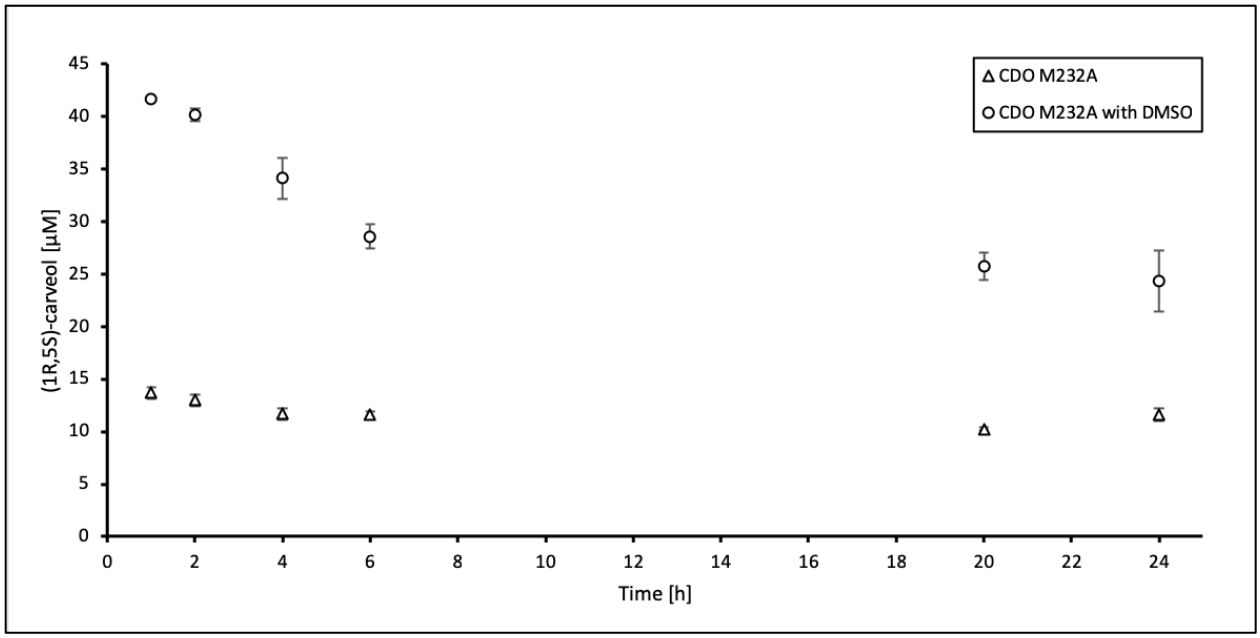

FIGURE 31 - Reaction rate of light-driven whole-cell biotransformations of 10 mM (*R*)-(+)-limonene to (1*R*,5*S*)-carveoL catalyzed by CDO M232A. Reaction conditions: 100 g_{cww}/L CDO M232A, 5 mM EDTA and 0.1 mM EY at 30 °C and irradiation with white light. Time points taken after 1, 2, 4, 6, 20 and 24 hours, with and without DMSO addition to dissolve (*R*)-(+)-limonene.

3 DISCUSSION

ROs can catalyze the chemo-, regio- and stereoselective oxyfunctionalization of a large number of alkenes and arenes (Ferraro, Gakhar and Ramaswamy, 2005; Gally, Nestl and Hauer, 2015). Nevertheless, common issues in redox biocatalysis are the requirement of cofactors, which create an economical challenge for the implementation of oxidoreductases in industrial processes (Dong *et al.*, 2018). In this study, an alternative light-driven cofactor supply was established for the whole-cell regio- and stereospecific hydroxylation of arenes by *E. coli* harboring the CDO from *P. fluorescens* IP01. The outline of this project was a) to examine the expression and activity of CDO in glucose supplemented reactions, b) to examine the simplification of the electron transfer system and c) to establish a photobiocatalytic process for the regeneration of cofactors in a whole-cell approach.

3.1 CLONING AND EXPRESSION OF CDO FOR *IN VITRO* PHOTOBIOCATALYSIS

CDO consists of three components involved in the electron transfer chain (Aoki *et al.*, 1996; Habe *et al.*, 1996; Ferraro, Gakhar and Ramaswamy, 2005). Nevertheless, two component ROs can be found in nature , for example, the benzoate dioxygenase and phthalate dioxygenase (Ferraro, Gakhar and Ramaswamy, 2005). Thus, the simplification of the system for the photobiocatalytic approach was investigated. Figure 32 shows a schematic representation of the pETDuet-based co-expression constructs containing different combinations of the CDO components. Since the β-subunit determines the substrate specificity, and omitting it might broaden the substrate scope, constructs 7 and 8 were constructed without CumA2. Furthermore, it has been demonstrated that photocatalysts (*e.g.* FMN, EY and RB) are capable of playing a key role as shuttles to supply a diverse variety of enzymes with electrons (Girhard *et al.*, 2013; Bissaro *et al.*, 2016; Rauch *et al.*, 2017; Biegasiewicz *et al.*, 2018; Huijbers *et al.*, 2018; Kim *et al.*, 2018; Zhang *et al.*, 2018). Therefore, constructs without FdR were created to examine the direct electron transfer from the photocatalyst to the ferredoxin (Figure 32).

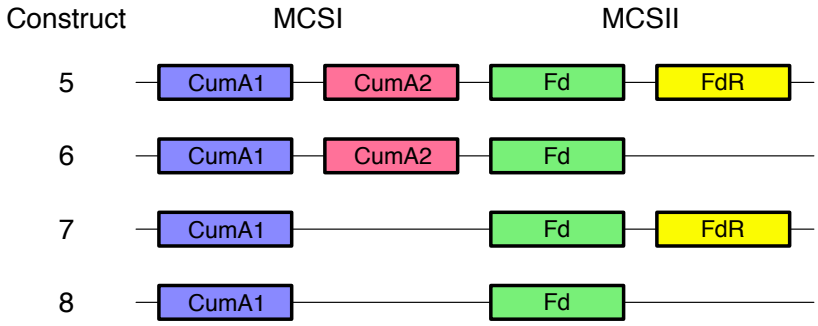

FIGURE 32 - Comparison of pETDuet-based co-expression constructs 5 to 8 harboring CDO components in two multiple cloning sites, each regulated by a lacO promoter. Boxes represent the genes of the CDO components.

By using standard molecular cloning techniques, various constructs containing components of CDO were created and investigated. Initially, the expression of the CDO components in *E. coli* BL21 was investigated. Therefore, constructs were created harboring codon-optimized single components of CDO, namely FdR, Fd, CumA1 and CumA2 (constructs 1-4). Expression studies revealed, that only the β-subunit of the terminal oxygenase (CumA2) was expressed in soluble form. It was previously reported that the expression of iron-sulfur clusters present in recombinant enzymes may entail difficulties (Jaganaman *et al.*, 2007; Gally, Nestl and Hauer, 2015). Jaganaman *et al.* detected that during the expression of the phthalate dioxygenase (PDO) from *Burkholderia cepacia* in recombinant *E. coli*, a shift in pH could affect the loss of the iron-sulfur cluster within the ferredoxin (Jaganaman *et al.*, 2007). Additionally, previous work by others confirmed that the detection of Fd and FdR using SDS-PAGE was inconclusive, which confers with the findings in this project (Gally, 2016). Furthermore, constructs 1 to 4 contain a His-tag, thrombin site and T7 tag, which could promote inclusion body formation of CumA1, as well as, effect the tertiary protein structure, thus leading to a loss of enzyme activity (Rosano and Ceccarelli, 2014).

Since CumA1 contains a disulfide bridge, for heterologous expression of CDO was further investigated in *E. coli* SHuffle ((Dong *et al.*, 2005)). *E. coli* SHuffle is engineered to promote the formation of disulfide bonds in the cytoplasm (Lobstein *et al.*, 2012). The correct folding of proteins containing disulfide bonds is achieved through the knockout of

the thioredoxin reductase (*trxB*) and glutathionine-disulfide reductase (*gor*), which would create a reductive environment for heterologous protein expression. Furthermore, the introduction of DsbC in *E. coli* SHuffle, a disulfide bond isomerase, increases oxidative folding of proteins (Lobstein *et al.*, 2012). Nevertheless, the expression of CDO in *E. coli* SHuffle did not increased the detectable amount of soluble enzyme. However, the growth of *E. coli* SHuffle during CDO expression showed an up to 2-fold decreased growth over 24 h compared to *E. coli* BL21(DE3) harboring the same constructs, which suggests a cause for decreased levels of heterologous protein expression.

In addition to constructs 5-8, the creation of a fusion protein between the α-subunit of the terminal oxygenase (CumA1) and the ferredoxin (Fd) was investigated. Therefore, constructs 9 to 16 were created using three different expression vectors, namely, pET28a(+), pETDuet-1 and pBAD/His A. The pBAD/His A expression vector was chosen because of its arabinose inducible promoter (P_{BAD}), which can be tightly regulated, and thus resulting in the reduced formation of inclusion bodies (Guzman *et al.*, 1995). Fusion proteins with either N- or C-terminal attachment of the Fd at the CumA1 were examined. Additionally, the fusion proteins were created with and without N/C-terminal His-tags to allow for purification and to be able to examine the effects of soluble expression. Nevertheless, the expression of all His-tag variations (-/N/C-terminal) of the fusion proteins showed no effects on soluble expression levels in *E. coli* BL21 and *E. coli* SHuffle.

To overcome the formation of inclusion bodies, the co-expression of various chaperones was examined. The best result could be obtained by co-expressing the chaperones GroEL-GroES in *E. coli* BL21(DE3). This resulted not only in the detection of soluble CumA1, but also in the production of soluble fusion proteins. The GroE chaperonins bind to proteins in non-native conformation and under ATP hydrolysis invoke the correct folding of these (Xu and Sigler, 1998).

3.2 *IN VITRO* PHOTOBIOCATALYSIS

Although soluble expression of CumA1 was achieved, *in vitro* photobiocatalysis and *in vivo* glucose supplemented reactions showed no product formation. Initial *in vitro* photobiocatalytic approaches were performed using CFE of *E. coli* BL21, harboring co-expression constructs 5-8, with FMN (photocatalyst) and EDTA (sacrificial electron donor). The combination of CFE/FMN/EDTA led to no detectable product formation for the conversion of styrene to 3-vinylcyclohexa-3,5-diene-1,2-diol, under blue light excitation. Furthermore, the fact that already in the *in vivo* reactions supplemented with glucose no activity could be detected suggests that also no conversion could be achieved in the photobiocatalytic reaction.

An explanation for inactive CDO in the initial experiments could be that codon-optimized genes have been used, which may lead to issues in co-translational folding. Codon bias does not only play an important role in heterologous protein expression levels, but rare codons can regulate translation rates, and thus can provide sufficient time for co-translational folding and incorporation of cofactors (Quax *et al.*, 2015). Due to that, the codon-optimized CDO variants may have no activity due to limitations encountered during the incorporation of the Rieske-type iron-sulfur cluster (2Fe-2s) and the ferrous oxide (Fe(II)) within the active site. Furthermore, it has been observed that ROs show inactivation due to reducing agents found in CFE, which could support these findings (Catterall and Williams, 1971; Sauber *et al.*, 1977). Nevertheless, further studies on the growth and expression of *E. coli* harboring ROs need to be performed. For example, the periplasmic expression of CDO could lead to an increase of correct-folded and thus active enzyme due to the oxidative environment found in the periplasm (Humphreys *et al.*, 2000; Chen, 2012).

3.3 Heterologous Expression of Active CDO M232A for *In Vivo* Photobiocatalysis

Since no activity was detected using CFE containing CDO, a whole-cell approach was examined for further development of the light-driven cofactor regeneration system. In previous studies, heterologous expression of CDO was carried out in *E. coli* JM109 using native genes (Aoki *et al.*, 1996; Habe *et al.*, 1996; Gally, Nestl and Hauer, 2015). Therefore, the pUC-based plasmid pIP107D, harboring a part of the PSECUMA locus, containing CumA1, CumA2, Fd and FdR, was used in the following experiments. Interestingly, an open reading frame (ORF3) can be detected between the genes encoding for CumA2 and Fd. Already in 1996, Aoki *et al.* and Habe *et al.* discussed the presence of this ORF3, which can also be found in the gene cluster encoding for the biphenyl dioxygenase from *Pseudomonas putida* KF715 (Aoki *et al.*, 1996; Habe *et al.*, 1996; Pflugmacher, Averhoff and Gottschalk, 1996). The function of ORF3 is, up to now, still unknown and must be further investigated since it could play a role for the activity of CDO.

Gally *et al.* successfully performed semi-rational design of CDO to improve conversion and enantioselectivity by introducing the mutation M232A in CumA1 (Gally, Nestl and Hauer, 2015). Hence, CDO M232A was examined for further development of the light-driven cofactor regeneration system. During expression of CDO M232A in *E. coli* JM109, a clear indigo formation in the culture could be detected, which suggests the expression of active CDO. In addition, the activity of CDO M232A was routinely confirmed by using an agar-plate assay based on indigo formation. When colonies of *E. coli* JM109 harboring active CDO, a blue color formation was observed after exposure to indole. This activity assay is based on the hydrolysis of tryptophan by *E. coli* using a tryptophanase, which results in the formation of indole for metabolic purposes and signaling (Li and Young, 2013). Accordingly, the indigo formation in cultures expressing CDO suggests that the formed indole is converted to indoxyl by active CDO, which further undergoes dimerization to form indigo.

3.3.1 Activity Determination of *E. coli* JM109 harboring CDO M232A

After the successful heterologous expression of active CDO M232A in *E. coli* JM109 using native genes (non-codon-optimized), the *in vivo* photobiocatalytic cofactor regeneration of CDO M232A was established. The conversion of styrene can entail the formation of radicals under exposure of light, which polymerizes and thus cannot be detected by GC-FID or GC-MS. Furthermore, the detection of products formed during the conversion of styrene proved to be challenging by GC-FID analyses. Moreover, 3-vinylcyclohexa-3,5-diene-1,2-diol could not be quantified due to the lack of a commercial standard. Thus, the *in vivo* photobiocatalytic reactions were performed using the transformation of (*R*)-(+)-limonene to (+)-carveol as a model reaction.

The mutation M232A is proposed to increase the conversion of (*R*)-(+)-limonene from 46 % up to 99 % (Gally, Nestl and Hauer, 2015). However, the transformation of (*R*)-(+)-limonene to (+)-carveol in glucose supplemented reactions by CDO M232A did not validate these previous findings. After 24 h of reaction, a final product formation of 2.6 mM (1*R*,5*S*)-carveol (*ee* 86 %) was detected, which results in a conversion of 26 % (substrate: 10 mM (*R*)-(+)-limonene). The glucose supplemented reactions showed a specific activity of 0.034 U/mg_{CWW} in the first 6 h. However, after 18 h of reaction no increase in product formation could be detected anymore, which suggests a loss of enzyme activity. The rapid loss of activity during the reaction could be explained by the indigo formation during cultivation, which reduces the total turnover number of the CDO. The utilization of a tryptophanase deficient *E. coli* strain could prevent the formation of indole during cultivation, this in turn could increase the total turnover number of CDO.

Furthermore, the microbial toxicity of limonene and carveol are factors affecting *in vivo* biocatalysis using *E. coli* (Sivropoulou *et al.*, 1996; Di Pasqua *et al.*, 2007; Alonso-Gutierrez *et al.*, 2013; Chubukov *et al.*, 2015; Lopez-Romero *et al.*, 2015). Microbial limonene toxicity can be caused by two reasons (Di Pasqua *et al.*, 2007; Chubukov *et al.*, 2015). First, the hydrophobicity of limonene can impact the structure of cellular membranes, thus acting antimicrobial and altering the structure of the outer cell membrane of *E. coli* (Di Pasqua *et al.*, 2007). Secondly, a major attribution to the cell

toxicity is the formation of limonene hydroperoxide, which can be detected as a contaminant in limonene stocks and is formed under aerobic conditions within several weeks during handling of limonene stocks. The use of an limonene hydroperoxide resistant *E. coli* strain containing the alkyl hydroperoxidase AhpC L177Q could reduce antimicrobial effects during the conversion of limonene (Chubukov *et al.*, 2015). In regard to carveol, Lopez *et al.* determined the minimum inhibitory concentration (MIC) and the minimal bactericidal concentration (MBC) for *E. coli* (Lopez-Romero *et al.*, 2015). Carveol showed an inhibiting effect at a concentration of 200 μg/mL and a bactericidal concentration at 1500 μg/mL (Lopez-Romero *et al.*, 2015). Hence, the 2.6 mM of carveol formed in the glucose supplemented reactions would result in 395.8 $\mu g_{carveol}$/mL, which could additionally explain the reduced yields.

3.4 Photobioreactor Design

Initially, the photobiocatalytic reactions have been performed in 4 mL screw-capped vials with O_2-filled balloons attached via a needle. This reactor setup led to a fast evaporation of the substrate due to their high volatility. To ensure sufficient O_2 supply, a 3D-printed photobioreactor laced with LEDs was created, which was capable of carrying 20 mL vials, ensuring sufficient O_2 supply when performing reactions at a final reaction volume of ~1.5 mL. Nevertheless, the 3D-printed photobioreactor did not contain active cooling elements, thus, heating and cooling was performed by placing the reactor in a shaker. Irradiation with blue light did not increase the temperature within the reactor. On the other hand, irradiation with white light showed a significant increase in temperature within the reactor, which created the need for adjusting the temperature of the shaker to 25 °C to ensure a constant temperature of 30 °C within the reactor. The increase in temperature under white light irradiation is probably attributable to all three LEDs (RGB) being used, compared to blue light irradiation using only 1 out of 3 LEDs. Although LEDs generally do not generate substantial amounts of heat, the reactor did not contain sufficient openings for heat exchange. Hence, a 3D-printed reactor with a mesh casing could provide the necessary structure for mounting the LEDs, as well as sufficient thermal

conductivity. Alternatively, the incorporation of a cooling system could be useful for further optimization of the photobioreactor.

3.5 *IN VIVO* PHOTOBIOCATALYSIS

After successfully expressing CDO M232A and determining the activity, the *in vivo* photobiocatalytic approach was established. Hence, the photosensitizers FMN, EY and RB were examined for their capability of acting as intermediate electron shuttles. Moreover, EDTA as well as TEA have been investigated as sacrificial electron donors in the desired *in vivo* photobiocatalytic approach. The successful conversion of (*R*)-(+)-limonene was achieved using the combination of EY/EDTA and RB/EDTA under white light irradiation. Using EY/EDTA, 86 μM of (1*R*,5*S*)-carveol (*ee* >99 %) was formed after 24 h. The combination of RB/EDTA led to a product formation of 52 μM (*ee* >99 %) after 24 h, whereas, glucose supplemented reactions showed the highest product formation of 2.6 mM. However, the use of RB resulted in the formation of various byproducts, which seem to be unspecific hydroxylation products. In addition, the conversion using lyophilized cells harboring CDO M232A was examined, which showed no product formation. A possible reason for no product formation could be the high concentration of lyophilized cells applied, suggesting the formation of dark zones, showing decreased light irradiation.

Previously, Park *et al.* described a light-driven whole-cell photobiocatalytic approach using cytochrome P450s (in *E. coli*) for the direct activation of the heme domain of the enzyme (Park *et al.*, 2015). Park *et al.* described the *O*-dealkylation of 7-ethoxycoumarin and the hydroxylation of marketed drugs (*e.g.* omeprazole) using EY (photocatalyst) and TEA (electron donor), reaching a product formation of up to ~75 μM for the hydroxylation of omeprazole (Park *et al.*, 2015). However, the use of TEA (sacrificial electron donor) with EY and CDO M232A did not result in the conversion of (*R*)-(+)-limonene by CDO M232A.

Interestingly, current literature searches revealed that to date, only few photobiocatalytic whole-cell approaches in *E. coli* are reported (Park *et al.*, 2015; Honda *et al.*, 2016). In contrast to Park *et al.*, Honda *et al.* demonstrate the formation of H_2 using TiO_2 (photocatalyst), methylviologen (electron donor) and *E. coli* harboring a [FeFe]-

hydrogenase (Honda *et al.*, 2016). Current photobiocatalytic systems are usually established as *in vitro* systems or using photosynthetic organisms for the upkeep of redox cofactors (*e.g.* in cyanobacteria) (Köninger *et al.*, 2016; Hoschek, Bühler and Schmid, 2017; Lee *et al.*, 2017). Systems not relying on oxygenases show promising conversion rates in whole-cell photobiocatalytic conversions with cyanobacteria. Köninger *et al.* showed that the double-bond reduction of 2-methyl-N-methylmaleimide by *Synechocystis* sp. PCC 6803 (harboring the ene-reductase YqjM from *Bacillus subtilis*) could reach a conversion rate of up to 10.5 mM/h at a cell density of 1.8 g_{CDW}/L (Köninger *et al.*, 2016). Alternatively, Hoschek *et al.* describe the hydroxylation of fatty acid methyl esters by *Synechocystis* sp. PCC 6803 harboring AlkBGT, an alcohol monooxygenase from *P. putida*. With this system, they reached a product formation of 54 μM after 30 min (reaction volume 1 mL, biocatalyst loading 2 g_{CDW}/L) (Hoschek, Bühler and Schmid, 2017). In contrast, the in this thesis reported photobiocatalytic *in vivo* reaction with CDO M232A using EY and EDTA (with addition of DMSO) showed a product formation of 42 μM after 1 h (reaction volume 1 mL, biocatalyst loading 100 g_{CWW}/L).

The low product yields of the light-driven *in vivo* CDO M232A system may be explained by the formation of undesired side reactions, *e.g.* the formation of radical oxygen species (uncoupling), which can effect enzyme stability and also acts as an electron sink (Holtmann and Hollmann, 2016; van Schie *et al.*, 2018; Zhang and Hollmann, 2018). Radical oxygen species may be formed by the photocatalyst, but also by the biocatalyst (Neary *et al.*, 2012; van Schie *et al.*, 2018). Nevertheless, the addition of catalase to the light-driven biotransformations did not result in increased product formation. Furthermore, the use of whole-cells may protect the CDO from radical oxygen species, which represents a further advantage of the *in vivo* photobiocatalytic system. Notwithstanding, the inhibitory effects of the substrate and the product represents more likely a reason for the reduced activity (as described previously).

To further increase the conversion in the photobiocatalytic whole-cell approach, different parameters could be targeted. For instance, the choice of substrate and buffer as well as the light source could lead to further understanding of the established system. Moreover,

the use of a tryptophanase knockout strain might further increases yields due to the increasing total turnover number of CDO. Due to time constraints, further investigation of the fusion protein constructs in the whole-cell light-driven approach could not be investigated. Therefore, the simplified system and the simplification of CDO using native instead of codon-optimized genes has to be examined in more detail in future studies. Nonetheless, this study clearly demonstrates the proof-of-concept for the light-driven *in vivo* cofactor supply of CDO, thus facilitating light-driven stereoselective hydroxylation reactions.

4 CONCLUSION

To conclude, this study gives a proof-of-concept for the *in vivo* photobiocatalytic conversion of (*R*)-(+)-limonene to (1*R*,5*S*)-carveol using the cumene dioxygenase (CDO) from *P. fluorescens* IP01 in *E. coli* JM109. CDO was chosen due to its potential of catalyzing the asymmetric *cis*-dihydroxylation of alkenes, which shows a promising alternative to conventional chemical synthesis routes. The establishment of an *in vitro* and *in vivo* photobiocatalytic system was investigated. Current findings revealed that the use of codon-optimized CDO in recombinant *E. coli* did not result in the expression of active enzyme. Nevertheless, expression optimization led to the successful heterologous expression of soluble protein using the co-expression of chaperones, namely GroEL/GroES. The use of native CDO resulted in the establishment of a whole-cell photobiocatalytic system. Due to the instability of CDO in CFE, the *in vitro* approach did not result in the conversion of (*R*)-(+)-limonene to (1*R*,5*S*)-carveol. However, an alternative light-driven *in vivo* cofactor regeneration without the addition of glucose was demonstrated in *E. coli* JM109 harboring CDO. The use of EY/RB (photosensitizer), EDTA (electron donor) and light irradiation resulted in the conversion of (*R*)-(+)-limonene, yielding 86 μM (1*R*,5*S*)-carveol. Photobiocatalysis was performed in a novel 3D-printed photobioreactor established during this study. Further optimization of the *in vivo* system could lead to the establishment of feasible light-driven cofactor regeneration alternatives for the supply of redox equivalents.

5 MATERIALS AND METHODS

5.1 DEVICES AND CHEMICALS

Unless otherwise stated, standard laboratory devices were used for the experiments performed in this thesis. All chemicals and compounds were obtained from Sigma-Aldrich Inc. or Carl-Roth GmbH.

5.2 MICROBIOLOGICAL METHODS

5.2.1 LIST OF STRAINS

For routine cloning and expression, chemically competent *E. coli* strains were used. All strains used for this thesis are listed below (Table 6).

TABLE 6 - Strains used for molecular cloning and protein expression.

strain	genotype	description/use	source
JM109	endA1, recA1, gyrA96, thi, hsdR17 (rk-, mk+), relA1, supE44, Δ(lac-proAB), [F´ traD36, proAB, laqIqZΔM15]	routine cloning and expression	New England Biolabs, Inc.
TOP10	F- mcrA Δ(mrr-hsdRMS-mcrBC) φ80(lacZ)ΔM15 Δ lacX74 recA1 araD139 Δ(araleu)7697 galU galK rpsL (StrR) endA1 nupG	routine cloning and expression	Thermo Fisher Scientific
Mach1	F- φ80(lacZ)ΔM15 ΔlacX74 hsdR(rK-mK+) ΔrecA1398 endA1 tonA	routine cloning, fast growth	Thermo Fisher Scientific
BL21(DE3)	F- ompT hsdSB (rBmB-) gal dcm (DE3)	high level expression of recombinant proteins	Thermo Fisher Scientific
SHuffle	F´ lac, pro, lacIq / Δ(ara-leu)7697 araD139 fhuA2 lacZ::T7 gene1 Δ(phoA)PvuII phoR ahpC* galE (or U) galK λatt::pNEB3-r1-cDsbC (SpecR, lacIq) ΔtrxB rpsL150(StrR) Δgor Δ(malF)3	co-expression of DsbC as a chaperone for folding of recombinantly expressed proteins which contain disulfide bonds	New England Biolabs, Inc.

5.2.2 General Purpose Media

For transformation and cultivation of *E. coli*, lysogeny broth (LB), terrific broth (TB) and super optimal broth with catabolite repression (SOC) were prepared (Table 7). LB and TB medium was autoclaved after addition of all components. SOC was sterile filtered and stored at 5 °C. 10x SOC was diluted with LB medium to create a 1x LB-SOC mixture, ready for use. Agar plates were created using LB medium containing 1.5 % agar and 0.5 mg/mL kanamycin or ampicillin.

TABLE 7 - General media composition.

LB medium	TB medium	SOC (10x)
0.5 g yeast extract	24 g yeast extract	0.1 g KCl
1 g tryptone	12 g tryptone	1 g $MgCl_2$
1 g NaCl	8 g glycerol	1 g $MgSO_4$
1 L ddH_2O	1 L ddH_2O	2 g glucose monohydrate
		50 mL ddH_2O

5.2.3 Autoinduction Medium - ZYP-5052

ZYP-5052 medium was prepared for auto-induced protein expression as described by Studier (Studier, 2005). 20x ZYP salts, 20x ZYP sugars and 100x $MgSO_4$ solutions were prepared as seen in Table 8. ZYP salt and sugar solutions were prepared at a final volume of 400 mL and autoclaved. The 100x $MgSO_4$ solution was sterile filtered through a 0.2 μM filter. For 800 mL medium, 8 g tryptone and 4 g yeast extract were dissolved in a final volume of 712 mL ddH_2O and subsequently autoclaved. After cooling, 40 mL 20x ZYP salts, 40 mL 20x ZYP sugars and 8 mL 100x $MgSO_4$ were added to reach a final volume of 800 mL.

TABLE 8 - Stock solutions for ZYP-5052 autoinduction medium.

20x ZYP salts (400 mL)	**20x ZYP sugars (400 mL)**	**100x $MgSO_4$ (50 mL)**
54 g KH_2PO_4	40 g glycerol	2.46 g $MgSO_4$
143 g Na_2HPO_4	4.4 g glucose-Monohydrate	
26.4 g $(NH_4)_2SO_4$	16 g lactose	

5.2.4 Over-Night Cultures

Over-night cultures (ONCs) were prepared in 15 mL or 50 mL falcons by inoculating 5-10 mL LB medium, containing kanamycin or ampicillin at a final concentration of 0.05 or 0.1 mg/mL, respectively. Inoculation was performed with a colony obtained from an agar plate or 5 μL of a glycerol stock. After 16 h at 37 °C, the ONC was used for further experiments.

5.2.5 Glycerol Stocks

For preparation of glycerol stocks, a 60 % glycerol in ddH_2O solution was created and autoclaved. Each glycerol stock was prepared by mixing 1 mL of an ONC with 1 mL of the glycerol solution (60 %) to reach a final concentration of 30 % glycerol. Next, the mixture was stored in cryotubes at -80 °C until further use.

5.3 Molecular Biological Methods

5.3.1 Primers

All primers were obtained from IDT (integrated DNA technologies, Inc.). A full list of primers can be found in Appendix A. For amplification of DNA fragments, primers were designed with an average length of ~20 nucleotides (nt) and a melting temperature (T_m) difference of less than 5 °C. The annealing temperature was calculated using the T_m Calculator from Thermo Fisher Scientific. For amplification of Gibson assembly® fragments, primers with a length of ~59 nt were designed. Gibson assembly primers contained a template binding region of ~20 nt and an overhang of ~40 nt.

To fix a random mutation in pCDO and introduce a mutation at M232A in CumA1, primers were designed according to the Stratagene QuikChange™ protocol (Appendix A).

5.3.2 List of Plasmids

Standard vectors were employed for cloning of all constructs (pET28a(+), pBAD/His A, pETDuet-1, pJET1.2, pUC118) (Table 9, 10). CumA4 was inserted in pJET1.2 for amplification of the gene. All vector maps can be found in Appendix B.

Additionally, a plasmid compromising of a pUC based vector and the partial locus of P. fluorescence containing CumA1, CumA2, CumA3 and CumA4 (partial), kindly provided by Prof. Hideaki Nojiri, University of Tokyo was used and modified (Table 11).

TABLE 9 - Plasmid containing codon-optimized synthetic genes.

construct	vector	resistance	insert	**His-tag**
1	pET28a(+)	Km	CumA1	N-term
2	pET28a(+)	Km	CumA2	N-term
3	pET28a(+)	Km	Fd	N-term
4	pET28a(+)	Km	FdR	N-term
5	pETDuet-1	Amp	MCSI: CumA1, CumA2; MCSII: Fd, FdR	-
6	pETDuet-1	Amp	CumA1, MCSI: CumA2; MCSII: Fd	-
7	pETDuet-1	Amp	MCSI: CumA1; MCSII: Fd, FdR	-
8	pETDuet-1	Amp	MCSI: CumA1; MCSII: Fd	-

TABLE 10 - Plasmids containing fusion proteins.

construct	vector	resistance	insert	linker	His-tag
9	pET28a(+)	Km	CumA1-Fd	$(EA_3K)_2$	N-term
10	pETDuet-1	Amp	MCSI: CumA1-Fd	$(EA_3K)_2$	N-term
11	pBAD/His A	Amp	CumA1-Fd	$(EA_3K)_2$	-
12	pBAD/His A	Amp	CumA1-Fd	$(EA_3K)_2$	N-term
13	pBAD/His A	Amp	CumA1-Fd	$(EA_3K)_2$	C-term
14	pBAD/His A	Amp	Fd-CumA1	-	-
15	pBAD/His A	Amp	Fd-CumA1	$(EA_3K)_2$	-
16	pBAD/His A	Amp	Fd-CumA1	$(G_4S)_2$	-

TABLE 11 - Plasmids containing the complete native CDO system. pIP107D was obtained from Prof. Hideaki Nojiri.

construct	vector	resistance	insert
pIP107D	pUC-based	Amp	CumA1, CumA2, CumA3 and partial CumA4
pCDO	pUC-based	Amp	CumA1, CumA2, CumA3, CumA4
pCDOv1	pUC-based	Amp	pCDO, with M232A mutation in CumA1

5.3.3 SYNTHETIC GENES

Codon-optimized synthetic genes compromising of Fd, FdR, CumA1 and CumA2 were ordered from GeneArt (Thermo Fisher Scientific, Regensburg, Germany). The genes were codon-optimized for *E. coli* using the company-own algorithm. Additionally, they contained restriction sites for *Bam*HI or *Hind*III at the 5' end and a *Not*I restriction site at the 3' end (Table 12).

TABLE 12 - Synthetic genes and restriction sites.

gene	size	restriction sites (5' - 3')
Fd	350 bp	*BamH*I - *Not*I
FdR	1258 bp	*Hind*III - *Not*I
CumA1	1401 bp	*BamH*I - *Not*I
CumA2	627 bp	*BamH*I - *Not*I

5.3.4 Design of Molecular Cloning Experiments and Computational Modelling

Molecular cloning experiments were designed using Benchling (accessed *via*: https://benchling.com). The different plasmids were created using different molecular cloning strategies. The initial constructs (1-4) containing the synthetic genes in pET28a(+) were created using restriction and ligation. The remaining constructs in pETDuet-1, pBAD/His A and pIP107D were created/modified using the Gibson assembly® approach (Gibson *et al.*, 2009). Alignment of sequences obtained during cloning was carried out in Benchling using MAFFT v7 or Clustal OMEGA (Sievers *et al.*, 2011; Katoh and Standley, 2013).

Since no crystal structures of Fd and FdR in the CDO system were available, homology models were built using YASARA (Version 16.7.22) (Krieger and Vriend, 2014). A model of the Rieske-type ferredoxin associated with CDO was created using the 1.6 Å resolution X-ray structure of the ferredoxin associated with the biphenyl dioxygenase from *Paraburkholderia xenovorans* (strain LB400) (PDD code: 1FQT) (Colbert *et al.*, 2000). The structural refinement was performed by energy minimization and molecular dynamics simulations in a water box. The resulting model was qualified as “good” with a final Z-score of -0.489by YASARA.

For the reductase (FdR), a model was created using the 1.8 Å resolution X-ray structure of the Toluene 2,3-Dioxygenase Reductase from *P. putida* F1 (PDB code: 3EF6) (Friemann *et al.*, 2009). The structural refinement was performed by energy minimization and molecular dynamics simulations in a water box. The resulting model was qualified as “good” with a final overall Z-score of -0.887 by YASARA. Visualization of models was

performed using PyMOL (The PyMOL Molecular Graphics System, Version 2.0 Schrödinger, LLC.).

5.3.5 Restriction/Ligation Cloning of Synthetic Genes in pET28a(+)

After amplification of each synthetic gene (see Polymerase Chain Reaction), the PCR product was digested with the appropriate restriction enzymes for 2.5 h at 37 °C (Table 12). After a final heat inactivation at 80 °C for 10 min, the gene fragments were cleaned with the Wizard SV Gel and PCR cleanup (Promega). Additionally, pET28a(+) was digested using *BamH*I/*Hind*III and *Not*I. The digested plasmids were separated using a 0.75 % agarose gel (see Agarose Gel Electrophoresis). After electrophoresis, the corresponding bands were excised and cleaned (see Gel Extraction). The digested backbones and inserts were ligated as seen in Table 13. After ligation, chemically competent *E. coli* TOP10 cells were transformed with the ligation mixture and streaked on LB-Km plates and incubated over-night at 37 °C. To validate the constructs, colony PCR was performed, and the hits were sequenced (see Colony PCR, DNA Sequencing).

TABLE 13 - Ligation procedure.

ligation reaction components	ligation conditions
1-2 μL Vector-DNA (50 ng)	2h 20°C
3-4 μL Insert-DNA (37.5 ng)	4h 16°C
0.7 μL T4-Ligase buffer 10x	3h 14°C
0.5 μL T4-Ligase	3h 12°C
0.8 μL ddH_2O	2h 10 °C
	10 min 72 °C

5.3.6 Gibson Assembly® Cloning of Co-expression and Fusion Protein Constructs

Constructs 5-16 were created using Gibson assembly® (Gibson *et al.*, 2009). Gibson assembly fragments were amplified by PCR (see 5.3.13), cleaned and assembled. After assembly, chemically competent *E. coli* TOP10/Mach1 cells were transformed with the assembly mixture, followed by Colony PCR and/or sequencing.

Gibson assembly fragments were created using PCR (see section 5.3.13). The PCR product was separated by a preparative agarose gel, and the respective bands were excised and cleaned (see section 5.3.12). Alternatively, the PCR product was cleaned by digestion of the plasmid DNA using *Dpn*I followed by a cleaning step, using the Wizard SV Gel and PCR cleanup kit (Promega). For the digestion with *Dpn*I, 1 µL was added to 50 µL PCR product and incubated at 37 °C for 2 h, followed by a heat inactivation at 80 °C for 10 min.

For the assembly, an equimolar amount of DNA was added to 15 µL assembly mix (final volume 20 µL) and incubated for 1 h at 50°C. At least 100 ng of the smallest fragment was used in the mix. After assembly, the mix was either stored at -20 °C or immediately used for the transformation of chemically competent *E. coli* TOP10/Mach1. The transformed cells were streaked on LB plates, containing the respective antibiotic, and incubated over-night at 37 °C. To validate the constructs, colony PCR was performed, and the hits were sequenced (see sections 5.3.14 and 5.3.15).

5.3.7 Reconstruction of Plasmid Encoding CDO

The plasmid pIP107D that was obtained from Hideaki Nojiri lacked a part of the reductase gene (CumA4). The reconstruction of CumA4 was performed by Gibson assembly®. The Gibson assembly fragments were amplified by PCR. Reactions were set up as described in Tables 17 - 20 (see 5.3.13). The backbone was amplified using pIP107D as template and using Phusion® High-Fidelity DNA Polymerase. The CumA4 insert was amplified using the native CumA4 gene as template and with DreamTaq DNA Polymerase. After synthesis, PCR reactions were pooled to a final volume of 150 µL and digested using 3 µL *Dpn*I and incubated at 37 °C for 2 h, followed by a heat inactivation at 80 °C for 10 min. After *Dpn*I digest the DNA concentrations of the fragments were measured using a NanoDrop™ 2000/2000c Spectrophotometer (Thermo Fisher Scientific). For the assembly, an equimolar amount of DNA was added to 15 µL assembly mix (final volume 20 µL) and incubated for 1 h at 50 °C. At least 100 ng of the smallest fragment was used in the mix. After assembly, 3 µL of the assembly mix were used for transformation of 50 µL

chemically competent *E. coli* TOP10 or Mach1 cells and plated on LB agar (1.5 %) supplemented with 100 µg/mL ampicillin. The correct reconstruction of CumA4 was confirmed by DNA sequencing after isolation of the plasmids from overnight cultures of grown colonies.

5.3.8 QUIKCHANGE™ OF CUMA1

To fix a random mutation in CumA1 (G205V) and introduce a mutation (M232A) site-directed mutagenesis was performed according to the Stratagene QuikChange™ protocol. Each QuikChange™ was performed as described in Tables 14 and 15. After synthesis of the mutated strands, the methylated parental strands were digested using *Dpn*I. For the digestion with *Dpn*I, 1 µL was added to 50 µL PCR product and incubated at 37 °C for 2 h, followed by a heat inactivation at 80 °C for 10 min.

TABLE 14 - QuikChange reaction.

QuikChange™	final volume 50 µL
5 µL	10x Pfu Buffer
1.25 µL	dNTP mix, 2 mM each
0.5 µL	FW primer (10 µM)
0.5 µL	RV primer (10 µM)
0.2 µL	Template
	10x Pfu DNA pol.
0.34 µL	(0.625 U)
47.71 µL	ddH_2O

TABLE 15 - QuikChange program.

PCR program	temperature	time
initial	95 °C	1 min
denaturation		
25 cycles:		
denaturation	95 °C	30 s
annealing	62 °C	40 s
extension	72 °C	3 min
final	72 °C	10 min
extension		

5.3.9 TRANSFORMATION OF CHEMICAL COMPETENT *E. COLI* CELLS

50 µL of chemo-competent *E. coli* cells were transformed with 2 µL plasmid DNA and incubated for 30 min on ice. After a heat shock at 42 °C for 42 s, 400 µL LB-SOC was added and the cells were incubated at 37 °C for 1 h. Finally, the cells were used to inoculate 5 mL liquid culture, and streaked out on LB plates, containing the corresponding antibiotic. Regarding kanamycin and ampicillin, final concentrations of 0.05 and 0.1 mg/mL medium were used, respectively.

5.3.10 Plasmid Isolation

Plasmid isolation was performed according to the manual with either the GeneJET Plasmid Miniprep Kit (Thermo Fisher Scientific) or the Wizard Plus SV Minipreps DNA Purification System (Promega Corporation).

5.3.11 Agarose Gel Electrophoresis

Agarose gels were created using TAE buffer at a final agarose concentration of 0.75/1 % (w/v) agarose, depending on the expected size of the DNA. A 50x TAE buffer was created and diluted to 1x for use (Table 16). For visualization, 8 μL ethidium bromide or 5 μL GelRed® Nucleic Acid Gel Stain (Biotium Inc.) were added to a 200 mL gel prior to cooling. All gels were run at 200 V and 400 mA until the bands were clearly separated (~40 min). Visualization was performed using the G:BOX F3 gel documentation system (Syngene, United Kingdom).

TABLE 16 - TAE buffer.

50x TAE buffer	final concentration 1x
242 g Tris	40 mM Tris
57.1 mL glacial acetic acid	20 mM acetic acid
100 mL of 500 mM EDTA (pH 8.0)	1 mM EDTA
to a final volume of 1 L with ddH_2O	

5.3.12 Gel Extraction

DNA Gel extraction was performed by cutting out the corresponding band and using the Wizard SV Gel and PCR cleanup kit (Promega) following the manufacturer's protocol.

5.3.13 Polymerase Chain Reaction

All genes and Gibson assembly fragments were amplified by a classical polymerase chain reaction (PCR). The initial reaction was tested using a gradient PCR at the calculated annealing temperature +/- 5 °C. PCR was either performed with DreamTaq polymerase

(Thermo Fisher Scientific) or Phusion® polymerase (New England Biolabs). Reactions were set up as described in Table 17 to Table 20.

TABLE 17 - DreamTaq PCR.

DreamTaq	final volume 25 µL
2.5 µL	10x DreamTaq Buffer
2.5 µL	dNTP mix, 2 mM each
1.25 µL	FW primer (10 µM)
1.25 µL	RV primer (10 µM)
0.3 µL	Template
0.125 µL	DreamTaq DNA pol. (0.625 U)
17.075 µL	ddH_2O

TABLE 18 - DreamTaq PCR program.

PCR program	temperature	time
initial denaturation	95 °C	1 min
30 cycles:		
denaturation	95 °C	30 s
annealing	55-72 °C	30 s
extension	72 °C	1 min
final extension	72 °C	1 min

TABLE 19 - Phusion PCR.

Phusion	final volume 25 µL
5 µL	5x Phusion HF buffer
0.5 µL	dNTP mix, 10 mM each
1.25 µL	FW primer (10 µM)
1.25 µL	RV primer (10 µM)
0.75 µL	template
0.25 µL	Phusion DNA pol.
16 µL	ddH_2O

TABLE 20 - Phusion PCR program.

PCR program	temperature	time
initial denaturation	98 °C	30 s
30 cycles:		
denaturation	98 °C	10 s
annealing	45-72 °C	30 s
extension	72 °C	30 s
final extension	72 °C	5 min

5.3.14 Colony PCR

10 to 15 colonies per construct were picked. Colony PCR was carried out using Maxima Hot Start Green PCR Master Mix (Thermo Fisher Scientific). Each picked colony was suspended in 15 µL reaction mixture containing 7.5 µL Maxima Master Mix (2x), 1.5 µL forward primer (5 µM), 1.5 µL reverse primer (5 µM) and 5 µL H_2O. The PCR program used can be seen in Table 21.

TABLE 21 - Colony PCR Program.

PCR program	temperature	time
initial denaturation	98 °C	4 min
30 cycles:		
denaturation	95 °C	30 s
annealing	45-72 °C	30 s
extension	72 °C	1 min/kb
final extension	72 °C	5 min

5.3.15 DNA SEQUENCING

To validate each cloning experiment, isolated plasmid was sequenced by Sanger Sequencing, which was performed by Eurofins GATC Biotech GmbH or Microsynth AG. The respective sequencing primers were either provided by the sequencing company or synthesized previously (see 5.3.1).

5.4 BIOCHEMICAL METHODS

5.4.1 HETEROLOGOUS EXPRESSION OF CDO IN *E. COLI*

Heterologous expression of CDO was performed in *E. coli* BL21(DE3), SHuffle and JM109. Transformation of chemically competent *E. coli* cells was performed as described previously (see 5.3.9). 200/400 mL of TB/LB/ZYP-5052 medium was inoculated with 5 mL overnight culture (ONC), or to an OD_{600} of 0.1. The cultures were incubated at 37 °C. After reaching an OD_{600} of 0.6-0.8 the cells were induced with IPTG at a final concentration of 0.2 mM IPTG or 0.5 mg/mL L-arabinose. After induction, the cells were incubated at 25 or 30 °C. The cells were harvested after 6-24 h after induction. Successful light-driven *in vivo* biotransformation was performed by heterologous expression at 30 °C for 20 h.

Expression studies were performed up to 24 h after induction. Moreover, the addition of $FeSO_4$ (final concentration 1 mM) and a chaperone plasmid set (Takara Bio Inc., France) was examined. $7/OD_{600}$ mL samples were taken at induction, as well as 3, 6 and 22/24 hours after induction. Each sample was centrifuged (3220 g, 10 min, 5 °C), the supernatant removed, and the pellet frozen until protein analysis using sodium dodecyl sulfate - polyacrylamide gel electrophoresis (SDS-PAGE) was performed.

5.4.2 Buffer Preparation

1 L 0.1 M sodium-phosphate buffer (pH 7.2) was used for sample preparation and biotransformation (BT). For buffer preparation, 0.2 M stock solutions of NaH_2PO_4 and Na_2HPO_4 were prepared (Table 22). Next, 195 mL NaH_2PO_4 (0.2M), 305 mL Na_2HPO_4 (0.2 M) and 500 mL H_2O were mixed to reach an initial pH of 7. The final pH of 7.2 was achieved by addition of NaOH.

TABLE 22 - Stock solutions for sodium-phosphate buffer.

0.2 M sodium phosphate, mono-sodium salt	0.2 M sodium phosphate, di-sodium salt
26.6 g $NaH_2PO_4 \cdot 1\ H_2O$	53.62 g $Na_2HPO_4 \cdot 7\ H_2O$
1 L ddH_2O	1 L ddH_2O

5.4.3 Sodium Dodecyl Sulfate - Polyacrylamide Gel electrophoresis (SDS-PAGE)

SDS-PAGE was performed using gels created as seen below or with pre-cast gels (NuPAGE 4-12 % Bis-Tris Gel, Thermo Fisher Scientific).

5.4.3.1 Buffers and gel preparation

A sample buffer was created containing:

- 1.25 mL 0.5 M TRIS-HCl (pH 6.8)
- 2 mL 10 % SDS-solution -> 10 g SDS in 100 mL
- 0.5 mL β-mercaptoethanol
- 2.5 mL glycerol
- 3.75 mL ddH_2O

10x SDS-Running Buffer, TRIS Buffer A and TRIS Buffer B were created as seen in Table 23. All pH values were adjusted using HCl and NaOH. SDS-PAGE was performed using a 12.5 % running gel and a 4 % stacking gel (Table 24). First, the running gel was poured, and isopropanol was used to cover the gel. After polymerization of the running gel, the isopropanol was removed, and the stacking gel was poured.

TABLE 23 - Buffers for SDS-PAGE.

10x SDS-Running Buffer	Tris Buffer A	Tris Buffer B
30 g Tris (1.5 M)	45.68 g Tris (1.5 M)	15.4 g Tris (0.5 M)
144 g glycine	1 g SDS (4 %)	0.25 g SDS (0.1 %)
10 g SDS (4%)		
in 1 L ddH_2O	in 250 mL ddH_2O	in 250 mL ddH_2O
pH=8.3	pH=8.8	pH=6.8

TABLE 24 - SDS-PA gel composition.

compound	running gel (12.5 %)	stacking gel (4 %)
Tris buffer A	2 mL	-
Tris buffer B	-	1 mL
acrylamide (30 %)	3.33 mL	0.53 mL
ddH_2O	2.67 mL	2.47 mL
APS	40 µL	40 µL
TEMED	4 µL	4 µL

5.4.3.2 SAMPLE PREPARATION

The obtained cell pellets were resuspended in 500 µL sodium phosphate buffer and sonicated on ice (see 5.5.1). After centrifugation (16.000 g, 15 min, 25 °C) the supernatant (soluble fraction) was stored for further analysis. The insoluble fraction was washed by resuspending the pellet in 500 µL sodium-phosphate buffer and centrifuged (16.000 g, 10 min, 25 °C). After washing, the supernatant was removed, and the pellet was resuspended in 500 µL sodium-phosphate buffer (insoluble fraction).

5 µL sample buffer and 15 µL sample (soluble/insoluble fraction) were incubated at 95 °C for 5 min before being loaded on a gel. Each gel was run for 55 min at 200 V and 60 mA (per gel). After electrophoresis, the gel was stained using Coomassie staining solution and destained using destaining solution (Table 25) as follows:

1. rinse gel with ddH_2O
2. add destaining solution
3. incubate on shaker 1 h
4. remove staining solution
5. wash with dH_2O
6. add fresh staining solution
7. incubate 1 h
8. remove staining solution and rinse with dH_2O

TABLE 25 - Solutions used for staining of SDS-PA gel.

Coomassie staining solution	destaining solution
1 g Coomassie Brilliant Blue G250	100 mL acetic acid
100 mL acetic acid (conc.)	300 mL ethanol
300 mL ethanol	600 mL ddH_2O
600 mL ddH_2O	

5.4.4 Solid Phase Colorimetric Assay based on Indigo Formation

For a qualitative analysis of cells expressing active CDO, the formation of indigo was observed by addition of indole. The assay was performed as described by Gally (Gally, 2016). A Whatman filter paper was bathed in a 10% solution of indole in acetone. After the filter was dry it was placed in the lid of an agar plate containing *E. coli* colonies and incubated at room temperature, until indigo formation was observed.

5.4.5 Light Reactor Construction

A 3D printed light reactor was created for the implementation of light-driven biotransformations. Using Fusion 360 (Autodesk Inc.) a model was designed. The designed model was 3D printed using the Ultimaker^2 (Ultimaker B.V.) with polylactide (PLA). The interior of the light reactor was lined with conventional LED strips (RGB, 12 V).

5.4.6 Biotransformation (BT)

In vivo and *in vitro* BT of styrene and (*R*)-(+)-limonene utilizing cell-free extract (CFE) and whole-cells were performed. First, *E. coli* cells harboring the respective constructs were cultivated and heterologous expression of CDO was performed (see 5.4.1). 6 to 24 h after induction, the cells were harvested and washed with SPB. First, the cultures were centrifuged for 20 min at 3580 g. Washing was performed with 30-50 mL SPB, followed by an additional centrifugation step for 20 min at 3580 g. Finally, the cells were resuspended to a cell wet weight (CWW) of 200 g_{CWW}/L in SPB for further use.

Light-driven reactions, supplemented with photosensitizers and electron donors, were performed at 30 °C in a water-bath lined with LED strips or in the 3D printed light reactor. Reactions without light excitation, which were supplemented with cofactors

(NADPH/D-glucose), were performed in a shaker at 30 °C. Biotransformations were set up as seen in tables 26 and 27 at a total volume of 1/1.5 mL in 2/20 mL screw capped glass vials.

To ensure O_2 supply, balloons filled with O_2 were attached to the 2 mL vials using a syringe and caps containing a membrane. 10 mM of the respective substrate were used. Additionally, due to the highly insoluble substrates, substrate stocks containing 250 mM of the respective substrate in DMSO were used.

An initial sample of 500 µL was taken at $t_{0\,h}$ and analyzed using GC. After 1, 2, 4, 6, 18, 24, 48 or 72 h the reaction mixture was immediately extracted and analyzed using GC or frozen for later analysis (see 5.4.7).

5.4.6.1 LIGHT-DRIVEN BIOTRANSFORMATION

Light-driven reactions were examined using cell-free extract, whole-cells and lyophilized cells. Flavin mononucleotide (FMN), eosin Y (EY) and rose bengal (RB) were investigated as photosensitizer. Furthermore, ethylenediaminetetraacetic acid (EDTA) and triethanolamine (TEA), respectively, were supplemented as electron donor. Additionally, the addition of catalase was tested. Excitation was performed using white or blue light. Table 26 shows all examined components.

TABLE 26 - Light-driven reaction scheme.

function	component	final concentration
catalyst	cell-free extract	250 µL/mL
	whole-cells	10-200 g_{CWW}/L
	lyophilized cells	5 mg/mL
photosensitizer	FMN	
	EY	0.1 mM
	RB	
electron donor	EDTA	5 mM
	TEA	
substrate	styrene	10 mM
	(*R*)-(+)-limonene	
optionally:	catalase	1 mg/mL

5.4.6.2 COFACTOR SUPPLEMENTED BIOTRANSFORMATION

In contrast to light-driven reactions, cofactor or D-glucose supplemented reactions, without light excitation were carried out. Reactions performed with lysate were supplemented with NADPH as a cofactor, whereas, biotransformations performed with whole-cells were supplemented with D-glucose (Table 27).

TABLE 27 - Cofactor supplemented reaction scheme.

function	component	final concentration
catalyst	cell-free extract	250 μL/mL
	whole-cells	10-200 g_{CWW}/L
	lyophilized cells	5 mg/mL
cofactor	NADPH	50 mM
	D-glucose	20 mM
substrate	styrene	10 mM
	(*R*)-(+)-limonene	

5.4.7 GAS CHROMATOGRAPHY - FLAME IONIZATION/MASS SPECTROMETRY

GC methods were established for the qualitative and quantitative analyses of substrate and product. Quantitative analysis was performed using GC-FID, utilizing a chiral or achiral column. Qualitative analysis of substrate and product was performed using GC-MS.

5.4.7.1 ORGANIC PHASE EXTRACTION

Organic phase extraction of the biotransformation samples was performed using dichloromethane (DCM). First, a spatula tip of NaCl was added to 500 μL sample and briefly vortexed. The sample was extracted with 500 μL DCM containing 2 mM acetophenone. Extraction was performed by adding DCM, vortexing the mixture for 10 s, followed by a centrifugation step for 2 min at 16000 g. The lower phase was transferred to an Eppendorf tube containing a spatula tip of $MgSO_4$. After vortexing for 10 s, the samples were centrifuged for 10 min at 16000 g. After centrifugation 200 μL sample was transferred to a 2 mL GC-vial, containing a 250 μL inlet, and analyzed.

5.4.7.2 GC-FID

Achiral quantitative analysis was performed on a Shimadzu GC-2010 Plus with a Zebron ZB-5 capillary column with nitrogen as carrier gas. Chiral quantitative analysis was performed on a Shimadzu Nexis GC-2030 equipped with a Hydrodex-β-6TBDM capillary column. For each substrate and respective product, a method was established. This enabled the detection of styrene conversion to 3-vinylcyclohexa-3,5-diene-1,2-diol or 1-phenyl-1,2-ethanediol in one method and (*R*)-(+)-limonene to carveol in the second established method. Parameters and GC temperature programs can be found in Appendix C.

5.4.7.3 GC-MS

GC-MS analyses were performed on a Shimadzu GCMS-QP2010 SE using a Zebron ZB-5MSi capillary column. Helium was used as carrier gas. Mass spectra were determined in scan mode at a range from 50 to 500 m/z. Additional parameters can be seen in Table 33 (Appendix C).

5.4.7.4 Calibration

A calibration curve for quantitative analysis using GC-FID was performed. Calibrations were only created for styrene, 1-phenyl-1,2-ethanediol, (*R*)-(+)-limonene and (-)-carveol (mixture of isomers) since 3-vinylcyclohexa-3,5-diene-1,2-diol could not be obtained commercially. Each calibration consisted of a mixture of the respective compounds in DCM containing 2 mM acetophenone as internal standard. The calibration curve was created for a concentration range from 0.1 to 10 mM of the respective analyte. The respective calibration curves can be found in Appendix D.

5.5 Biophysical Methods

5.5.1 Cell Disruption

For the cell disruption process, 100 g_{CWW}/L cells in SPB were sonicated on ice. For SDS-PAGE samples, the cells were sonicated using a small probe for 2 x 60 s (duty cycle: 40, output control: 4). Larger volumes (~25 mL) for biotransformation were sonicated

using a larger probe 2 x 3 min (duty cycle: 40, output control: 4). The sonication was increased if the solution was not visibly clearer.

After cell disruption, the lysate was centrifuged for 20 min at 3580 g to remove cell debris. The supernatant was sterile filtered for use in biotransformation reactions.

5.5.2 Lyophilization of Cells

Lyophilization of whole-cells was performed by freezing 200 g_{CWW}/L cell suspension in a glass piston in liquid nitrogen. After freezing, the cells were lyophilized for 24 h using the AdVantage Pro Freeze Dryer/Lyophilizer with Intellitronics Controller (SP Scientific) connected to a vacuum pump (Model: VP-60X, SP Scientific). The lyophilized cells were stored at -80 °C until further use.

6 REFERENCES

Adam, D., Bösche, L., Castañeda-Losada, L., Winkler, M., Apfel, U. P. and Happe, T. (2017) 'Sunlight-Dependent Hydrogen Production by Photosensitizer/Hydrogenase Systems', *ChemSusChem*, 10(5), pp. 894–902. doi: 10.1002/cssc.201601523.

Alonso-Gutierrez, J., Chan, R., Batth, T. S., Adams, P. D., Keasling, J. D., Petzold, C. J. and Lee, T. S. (2013) 'Metabolic engineering of Escherichia coli for limonene and perillyl alcohol production', *Metabolic Engineering*. Elsevier, 19, pp. 33–41. doi: 10.1016/j.ymben.2013.05.004.

Ang, E. L., Obbard, J. P. and Zhao, H. (2007) 'Probing the molecular determinants of aniline dioxygenase substrate specificity by saturation mutagenesis', *FEBS Journal*, 274(4), pp. 928–939. doi: 10.1111/j.1742-4658.2007.05638.x.

Aoki, H., Kimura, T., Habe, H., Yamane, H., Kodama, T. and Omori, T. (1996) 'Cloning, Nucleotide Sequence, and Characterization of the Genes Encoding Enzymes Involved in the Degradation of Cumene to 2-Hydroxy-6-Oxo-7-Methylocta-2,4-Dienoic Acid in Pseudomonas fluorescens IP01', *Journal of Fermentation and Bioengineering*, 81(3), pp. 187–196. doi: 10.1016/0922-338X(96)82207-0.

Barry, S. M. and Challis, G. L. (2013) 'Mechanism and catalytic diversity of rieske non-heme iron-dependent oxygenases', *ACS Catalysis*, 3(10), pp. 2362–2370. doi: 10.1021/cs400087p.

Bassan, A., Borowski, T. and Siegbahn, P. E. M. (2004) 'Quantum chemical studies of dioxygen activation by mononuclear non-heme iron enzymes with the 2-His-1-carboxylate facial triad', *Dalton Transactions*, (20), pp. 3153–3162. doi: 10.1039/b408340g.

Batie, C. I., Ballou, D. P. and Correll, C. C. (1992) 'Phthalate Dioxygenase Reductase and Related Flavin-Iron-Sulfur-Containing Electron Transferases', *Chemistry and Biochemisty of Flavoenzymes*, pp. 544–554.

Biegasiewicz, K. F., Cooper, S. J., Emmanuel, M. A., Miller, D. C. and Hyster, T. K. (2018) 'Catalytic promiscuity enabled by photoredox catalysis in nicotinamide-dependent oxidoreductases', *Nature Chemistry*. Springer US, 10(7), pp. 770–775. doi: 10.1038/s41557-018-0059-y.

Bissaro, B., Forsberg, Z., Ni, Y., Hollmann, F., Vaaje-Kolstad, G. and Eijsink, V. G. H. (2016) 'Fueling biomass-degrading oxidative enzymes by light-driven water oxidation', *Green Chemistry*. Royal Society of Chemistry, 18(19), pp. 5357–5366. doi: 10.1039/c6gc01666a.

Bornscheuer, U. T., Huisman, G. W., Kazlauskas, R. J., Lutz, S., Moore, J. C. and Robins, K. (2012) 'Engineering the third wave of biocatalysis', *Nature*. Nature Publishing Group, 485(7397), pp. 185–194. doi: 10.1038/nature11117.

Boyd, D. R., Sharma, N. D., Bowers, N. I., Brannigan, I. N., Groocock, M. R., Malone, J. F., McConville, G. and Allen, C. C. R. (2005) 'Biocatalytic asymmetric dihydroxylation of conjugated mono-and poly-alkenes to yield enantiopure cyclic cis-diols', *Advanced Synthesis and Catalysis*, 347(7–8), pp. 1081–1089. doi: 10.1002/adsc.200505033.

Bugg, T. D. and Ramaswamy, S. (2008) 'Non-heme iron-dependent dioxygenases: unravelling catalytic mechanisms for complex enzymatic oxidations', *Current Opinion in Chemical Biology*, 12(2), pp. 134–140. doi: 10.1016/j.cbpa.2007.12.007.

Capyk, J. K., D'Angelo, I., Strynadka, N. C. and Eltis, L. D. (2009) 'Characterization of 3-ketosteroid 9α-hydroxylase, a Rieske oxygenase in the cholesterol degradation pathway of Mycobacterium tuberculosis', *Journal of Biological Chemistry*, 284(15), pp. 9937–9946. doi: 10.1074/jbc.M900719200.

De Carvalho, C. C. C. R. (2011) 'Enzymatic and whole cell catalysis: Finding new strategies for old processes', *Biotechnology Advances*. Elsevier Inc., 29(1), pp. 75–83. doi: 10.1016/j.biotechadv.2010.09.001.

Catterall, G. F. and Williams, P. A. (1971) 'Some properties of the naphthalene oxygenase from Pseudomonas sp. NCIB 9816', *Journal of General Microbiology*, 67(1), pp. 117–124. doi: 10.1099/00221287-67-1-117.

Chen, Q., Wang, C. H., Deng, S. K., Wu, Y. D., Li, Y., Yao, L., Jiang, J. D., Yan, X., He, J. and Li, S. P. (2014) 'Novel three-component Rieske non-heme iron oxygenase system catalyzing the N-dealkylation of chloroacetanilide herbicides in sphingomonads DC-6 and DC-2', *Applied and Environmental Microbiology*, 80(16), pp. 5078–5085. doi: 10.1128/AEM.00659-14.

Chen, R. (2012) 'Bacterial expression systems for recombinant protein production: *E. coli* and beyond', *Biotechnology Advances*. Elsevier Inc., 30(5), pp. 1102–1107. doi: 10.1016/j.biotechadv.2011.09.013.

Choi, J. M., Han, S. S. and Kim, H. S. (2015) 'Industrial applications of enzyme biocatalysis: Current status and future aspects', *Biotechnology Advances*. Elsevier Inc., 33(7), pp. 1443–1454. doi: 10.1016/j.biotechadv.2015.02.014.

Chubukov, V., Mingardon, F., Schackwitz, W., Baidoo, E. E. K., Alonso-Gutierrez, J., Hu, Q., Lee, T. S., Keasling, J. D. and Mukhopadhyay, A. (2015) 'Acute limonene toxicity in Escherichia coli is caused by limonene hydroperoxide and alleviated by a point mutation in alkyl hydroperoxidase AhpC', *Applied and Environmental Microbiology*, 81(14), pp. 4690–4696. doi: 10.1128/AEM.01102-15.

Colbert, C. L., Couture, M. M. J., Eltis, L. D. and Bolin, J. T. (2000) 'A cluster exposed: Structure of the rieske ferredoxin from biphenyl dioxygenase and the redox properties of Rieske Fe-S proteins', *Structure*, 8(12), pp. 1267–1278. doi: 10.1016/S0969-2126(00)00536-0.

D'Ordine, R. L., Rydel, T. J., Storek, M. J., Sturman, E. J., Moshiri, F., Bartlett, R. K., Brown, G. R., Eilers, R. J., Dart, C., Qi, Y., Flasinski, S. and Franklin, S. J. (2009) 'Dicamba Monooxygenase: Structural Insights into a Dynamic Rieske Oxygenase that Catalyzes an Exocyclic Monooxygenation', *Journal of Molecular Biology*. Elsevier Ltd, 392(2), pp. 481–497. doi: 10.1016/j.jmb.2009.07.022.

DeLano, W. L. (2000) *{T}he {P}y{MOL} {M}olecular {G}raphics {S}ystem*, *DeLano Scientific*.

Denard, C. A., Hartwig, J. F. and Zhao, H. (2013) 'Multistep one-pot reactions combining biocatalysts and chemical catalysts for asymmetric synthesis', *ACS Catalysis*, 3(12), pp. 2856–2864. doi: 10.1021/cs400633a.

Dong, J. J., Fernández-Fueyo, E., Hollmann, F., Paul, C. E., Pesic, M., Schmidt, S., Wang, Y., Younes, S. and Zhang, W. (2018) 'Biocatalytic Oxidation Reactions: A Chemist's Perspective', *Angewandte Chemie, International Edition*, 57(30), pp. 9238–9261. doi: 10.1002/anie.201800343.

Dong, X., Fushinobu, S., Fukuda, E., Terada, T., Nakamura, S., Shimizu, K., Nojiri, H., Omori, T., Shoun, H. and Wakagi, T. (2005) 'Crystal structure of the terminal oxygenase component of cumene dioxygenase from Pseudomonas fluorescem IP01', *Journal of Bacteriology*, 187(7), pp. 2483–2490. doi: 10.1128/JB.187.7.2483-2490.2005.

Dror, A. and Fishman, A. (2012) 'Engineering Non-Heme Mono- and Dioxygenases for Biocatalysis', *Computational and Structural Biotechnology Journal*. Research Network of Computational and Structural Biotechnology (RNCSB) Organization, 2(3), p. e201209011. doi: 10.5936/csbj.201209011.

Duetz, W. A., Van Beilen, J. B. and Witholt, B. (2001) 'Using proteins in their natural environment: Potential and limitations of microbial whole-cell hydroxylations in applied biocatalysis', *Current Opinion in Biotechnology*, 12(4), pp. 419–425. doi: 10.1016/S0958-1669(00)00237-8.

Ferraro, D. J., Gakhar, L. and Ramaswamy, S. (2005) 'Rieske business: Structure-function of Rieske non-heme oxygenases', *Biochemical and Biophysical Research Communications*, 338(1), pp. 175–190. doi: 10.1016/j.bbrc.2005.08.222.

Friemann, R., Lee, K., Brown, E. N., Gibson, D. T., Eklund, H. and Ramaswamy, S. (2009) 'Structures of the multicomponent Rieske non-heme iron toluene 2,3-dioxygenase enzyme system', *Acta Crystallographica, Section D: Biological Crystallography*. 2008/12/19. International Union of Crystallography, 65(Pt 1), pp. 24–33. doi: 10.1107/S0907444908036524.

Gally, C. (2016) *Enzymatic asymmetric dihydroxylation of alkenes*.

Gally, C., Nestl, B. M. and Hauer, B. (2015) 'Engineering Rieske Non-Heme Iron Oxygenases for the Asymmetric Dihydroxylation of Alkenes', *Angewandte Chemie, International Edition*, 54(44), pp. 12952–12956. doi: 10.1002/anie.201506527.

Gamenara, D., Seoane, G., Méndez, P. S., Domínguez de María, P. and de María, P. D. (2012) *Redox Biocatalysis: Fundamentals and Applications*. Wiley.

Gibson, D. G., Young, L., Chuang, R.-Y., Venter, J. C., Hutchison, C. A. and Smith, H. O. (2009) 'Enzymatic assembly of DNA molecules up to several hundred kilobases', *Nature Methods*. Nature Publishing Group, 6(5), pp. 343–345. doi: 10.1038/nmeth.1318.

Gibson, D. T. and Parales, R. E. (2000) 'Aromatic hydrocarbon dioxygenases in environmental biotechnology', *Current Opinion in Biotechnology*, 11(3), pp. 236–243. doi: 10.1016/S0958-1669(00)00090-2.

Girhard, M., Kunigk, E., Tihovsky, S., Shumyantseva, V. V. and Urlacher, V. B. (2013) 'Light-driven biocatalysis with cytochrome P450 peroxygenases', *Biotechnology and Applied Biochemistry*, 60(1), pp. 111–118. doi: 10.1002/bab.1063.

Groeneveld, M., van Beek, H. L., Duetz, W. A. and Fraaije, M. W. (2016) 'Identification of a novel oxygenase capable of regiospecific hydroxylation of D-limonene into (+)-trans-carveol', *Tetrahedron*, 72(46), pp. 7263–7267. doi: 10.1016/j.tet.2015.12.061.

Guzman, L. M., Belin, D., Carson, M. J., Beckwith, J., Guzman, L., Belin, D. and Carson, M. J. (1995) 'Tight regulation , modulation , and high-level expression by vectors containing the arabinose PBAD promoter . These include : Tight Regulation , Modulation , and High-Level Expression by Vectors Containing the Arabinose P BAD Promoter', *Journal of Bacteriology*, 177(14), pp. 4121–4130. doi: 10.1098/rstb.1976.0083.

Habe, H., Kasuga, K., Nojiri, H., Yamane, H. and Omori, T. (1996) 'Analysis of cumene (isopropylbenzene) degradation genes from Pseudomonas fluorescens IP01', *Applied and Environmental Microbiology*, 62(12), pp. 4471–4477.

Halder, J. M., Nestl, B. M. and Hauer, B. (2018) 'Semirational Engineering of the Naphthalene Dioxygenase from Pseudomonas sp. NCIB 9816-4 towards Selective Asymmetric Dihydroxylation', *ChemCatChem*, 10(1), pp. 178–182. doi: 10.1002/cctc.201701262.

Hemschemeier, A., Melis, A. and Happe, T. (2009) 'Analytical approaches to photobiological hydrogen production in unicellular green algae', *Photosynthesis Research*, 102(2), pp. 523–540. doi: 10.1007/s11120-009-9415-5.

Hollmann, F., Taglieber, A., Schulz, F. and Reetz, M. T. (2007) 'A light-driven stereoselective biocatalytic oxidation', *Angewandte Chemie, International Edition*, 46(16), pp. 2903–2906. doi: 10.1002/anie.200605169.

Holtmann, D. and Hollmann, F. (2016) 'The Oxygen Dilemma: A Severe Challenge for the Application of Monooxygenases?', *ChemBioChem*, pp. 1391–1398. doi: 10.1002/cbic.201600176.

Honda, Y., Hagiwara, H., Ida, S. and Ishihara, T. (2016) 'Application to Photocatalytic H2 Production of a Whole-Cell Reaction by Recombinant Escherichia coli Cells Expressing [FeFe]-Hydrogenase and Maturases Genes', *Angewandte Chemie, International Edition*, 55(28), pp. 8045–8048. doi: 10.1002/anie.201600177.

Hoschek, A., Bühler, B. and Schmid, A. (2017) 'Overcoming the Gas-Liquid Mass Transfer of Oxygen by Coupling Photosynthetic Water Oxidation with Biocatalytic Oxyfunctionalization', *Angewandte Chemie, International Edition*, 56(47), pp. 15146–15149. doi: 10.1002/anie.201706886.

Huijbers, M. M. E., Zhang, W., Tonin, F. and Hollmann, F. (2018) 'Light-Driven Enzymatic Decarboxylation of Fatty Acids', *Angewandte Chemie, International Edition*, pp. 13648–13651. doi: 10.1002/anie.201807119.

Humphreys, D. P., Sehdev, M., Chapman, A. P., Ganesh, R., Smith, B. J., King, L. M.,

Glover, D. J., Reeks, D. G. and Stephens, P. E. (2000) 'High-level periplasmic expression in Escherichia coli using a eukaryotic signal peptide: Importance of codon usage at the 5' end of the coding sequence', *Protein Expression and Purification*, 20(2), pp. 252–264. doi: 10.1006/prep.2000.1286.

Hurtubise, Y., Barriault, D. and Sylvestre, M. (1998) 'Involvement of the Terminal Oxygenase β Subunit in the Biphenyl Dioxygenase Reactivity Pattern toward Chlorobiphenyls', *Journal of Bacteriology*, 180(22), pp. 5828–5835.

Jaganaman, S., Pinto, A., Tarasev, M. and Ballou, D. P. (2007) 'High levels of expression of the iron-sulfur proteins phthalate dioxygenase and phthalate dioxygenase reductase in Escherichia coli', *Protein Expression and Purification*, 52(2), pp. 273–279. doi: 10.1016/j.pep.2006.09.004.

Kagami, O., Shindo, K., Kyojima, A., Takeda, K., Ikenaga, H., Furukawa, K. and Misawa, N. (2008) 'Protein engineering on biphenyl dioxygenase for conferring activity to convert 7-hydroxyflavone and 5,7-dihydroxyflavone (chrysin)', *Journal of Bioscience and Bioengineering*, 106(2), pp. 121–127. doi: 10.1263/jbb.106.121.

Kalnins, G., Sevostjanovs, E., Hartmane, D., Grinberga, S. and Tars, K. (2018) 'CntA oxygenase substrate profile comparison and oxygen dependency of TMA production in Providencia rettgeri', *Journal of Basic Microbiology*, 58(1), pp. 52–59. doi: 10.1002/jobm.201700428.

Katoh, K. and Standley, D. M. (2013) 'MAFFT multiple sequence alignment software version 7: Improvements in performance and usability', *Molecular Biology and Evolution*, 30(4), pp. 772–780. doi: 10.1093/molbev/mst010.

Kim, J., Lee, S. H., Tieves, F., Choi, D. S., Hollmann, F., Paul, C. E. and Park, C. B. (2018) 'Biocatalytic C=C Bond Reduction through Carbon Nanodot-Sensitized Regeneration of NADH Analogues', *Angewandte Chemie, International Edition*, pp. 13825–13828. doi: 10.1002/anie.201804409.

Köninger, K., Gómez Baraibar, Á., Mügge, C., Paul, C. E., Hollmann, F., Nowaczyk, M. M. and Kourist, R. (2016) 'Recombinant Cyanobacteria for the Asymmetric Reduction of C=C Bonds Fueled by the Biocatalytic Oxidation of Water', *Angewandte Chemie, International Edition*, 55(18), pp. 5582–5585. doi: 10.1002/anie.201601200.

Krieger, E. and Vriend, G. (2014) 'YASARA View - molecular graphics for all devices - from smartphones to workstations', *Bioinformatics (Oxford, England)*, 30(20), pp. 2981–2982. doi: 10.1093/bioinformatics/btu426.

Kweon, O., Kim, S. J., Baek, S., Chae, J. C., Adjei, M. D., Baek, D. H., Kim, Y. C. and Cerniglia, C. E. (2008) 'A new classification system for bacterial Rieske non-heme iron aromatic ring-hydroxylating oxygenases', *BMC Biochemistry*, 9(1), pp. 1–20. doi: 10.1186/1471-2091-9-11.

Lee, J. and Zhao, H. (2006) 'Mechanistic studies on the conversion of arylamines into arylnitro compounds by aminopyrrolnitrin oxygenase: identification of intermediates and kinetic studies', *Angewandte Chemie, International Edition*, 45(4), pp. 622–625. doi:

10.1002/anie.200502903.

Lee, S. H., Choi, D. S., Kuk, S. K. and Park, C. B. (2018) 'Photobiocatalysis: Activating Redox Enzymes by Direct or Indirect Transfer of Photoinduced Electrons', *Angewandte Chemie, International Edition*, 57(27), pp. 7958–7985. doi: 10.1002/anie.201710070.

Lee, S. H., Choi, D. S., Pesic, M., Lee, Y. W., Paul, C. E., Hollmann, F. and Park, C. B. (2017) 'Cofactor-Free, Direct Photoactivation of Enoate Reductases for the Asymmetric Reduction of C=C Bonds', *Angewandte Chemie, International Edition*, 56(30), pp. 8681–8685. doi: 10.1002/anie.201702461.

Li, G. and Young, K. D. (2013) 'Indole production by the tryptophanase TnaA in Escherichia coli is determined by the amount of exogenous tryptophan', *Microbiology*, 159(Pt_2), pp. 402–410. doi: 10.1099/mic.0.064139-0.

Lipscomb, J. D. and Hoffman, B. M. (2005) 'Allosteric control of O2reactivity in Rieske oxygenases', *Structure*, 13(5), pp. 684–685. doi: 10.1016/j.str.2005.04.003.

Lobstein, J., Emrich, C. A., Jeans, C., Faulkner, M., Riggs, P. and Berkmen, M. (2012) 'SHuffle, a novel Escherichia coli protein expression strain capable of correctly folding disulfide bonded proteins in its cytoplasm', *Microbial Cell Factories*. BioMed Central Ltd, 11(1), p. 753. doi: 10.1186/1475-2859-11-56.

Lopez-Romero, J. C., González-Ríos, H., Borges, A. and Simões, M. (2015) 'Antibacterial Effects and Mode of Action of Selected Essential Oils Components against Escherichia coli and Staphylococcus aureus', *Evidence-based Complementary and Alternative Medicine*, 2015. doi: 10.1155/2015/795435.

Martínez, A. T., Ruiz-Dueñas, F. J., Camarero, S., Serrano, A., Linde, D., Lund, H., Vind, J., Tovborg, M., Herold-Majumdar, O. M., Hofrichter, M., Liers, C., Ullrich, R., Scheibner, K., Sannia, G., Piscitelli, A., Pezzella, C., Sener, M. E., Kılıç, S., van Berkel, W. J. H., Guallar, V., Lucas, M. F., Zuhse, R., Ludwig, R., Hollmann, F., Fernández-Fueyo, E., Record, E., Faulds, C. B., Tortajada, M., Winckelmann, I., Rasmussen, J. A., Gelo-Pujic, M., Gutiérrez, A., del Río, J. C., Rencoret, J. and Alcalde, M. (2017) 'Oxidoreductases on their way to industrial biotransformations', *Biotechnology Advances*, 35(6), pp. 815–831. doi: 10.1016/j.biotechadv.2017.06.003.

Mason, J. (1992) 'The Electron-Transport Proteins of Hydroxylating Bacterial Dioxygenases', *Annual Review of Microbiology*, 46(1), pp. 277–305. doi: 10.1146/annurev.micro.46.1.277.

Mehrman, S. J., Abdel-Magid, A. F., Maryanoff, C. A. and Medaer, B. P. (2004) 'Non-Salen Metal-Catalyzed Asymmetric Dihydroxylation and Asymmetric Aminohydroxylation of Alkenes. Practical Applications and Recent Advances', in *Organometallics in Process Chemistry*. Berlin, Heidelberg: Springer Berlin Heidelberg, pp. 153–180. doi: 10.1007/b11773.

Mifsud, M., Gargiulo, S., Iborra, S., Arends, I. W. C. E., Hollmann, F. and Corma, A. (2014) 'Photobiocatalytic chemistry of oxidoreductases using water as the electron donor', *Nature Communications*. England: Nature Publishing Group, 5, p. 3145. doi:

10.1038/ncomms4145.

Nam, J.-W., Nojiri, H., Yoshida, T., Habe, H., Yamane, H. and Omori, T. (2001) 'New Classification System for Oxygenase Components Involved in Ring-Hydroxylating Oxygenations', *Bioscience, Biotechnology, and Biochemistry*, 65(2), pp. 254–263. doi: 10.1271/bbb.65.254.

Neary, N. M., El-Maouche, D., Hopkins, R., Libutti, S. K., Moses, A. M. and Weinstein, L. S. (2012) 'Development and Treatment of Tertiary Hyperparathyroidism in Patients with Pseudohypoparathyroidism Type 1B', *The Journal of Clinical Endocrinology & Metabolism*, 97(9), pp. 3025–3030. doi: 10.1210/jc.2012-1655.

Nojiri, H., Habe, H. and Omori, T. (2001) 'Bacterial degradation of aromatic compounds via angular dioxygenation', *The Journal of General and Applied Microbiology*, 47(6), pp. 279–305. doi: 10.2323/jgam.47.279.

Oberleitner, N., Peters, C., Muschiol, J., Kadow, M., Saß, S., Bayer, T., Schaaf, P., Iqbal, N., Rudroff, F., Mihovilovic, M. D. and Bornscheuer, U. T. (2013) 'An enzymatic toolbox for cascade reactions: A showcase for an in vivo redox sequence in asymmetric synthesis', *ChemCatChem*, 5(12), pp. 3524–3528. doi: 10.1002/cctc.201300604.

Parales, R. E., Resnick, S. M., Yu, C. L., Boyd, D. R., Sharma, N. D. and Gibson, D. T. (2000) 'Regioselectivity and enantioselectivity of naphthalene dioxygenase during arene cis-dihydroxylation: Control by Phenylalanine 352 in the α subunit', *Journal of Bacteriology*, 182(19), pp. 5495–5504. doi: 10.1007/s003300000593.

Park, J. H., Lee, S. H., Cha, G. S., Choi, D. S., Nam, D. H., Lee, J. H. J. K., Lee, J. H. J. K., Yun, C. H., Jeong, K. J. and Park, C. B. (2015) 'Cofactor-free light-driven whole-cell cytochrome P450 catalysis', *Angewandte Chemie, International Edition*, 54(3), pp. 969–973. doi: 10.1002/anie.201410059.

Di Pasqua, R., Betts, G., Hoskins, N., Edwards, M., Ercolini, D. and Mauriello, G. (2007) 'Membrane toxicity of antimicrobial compounds from essential oils', *Journal of Agricultural and Food Chemistry*, 55(12), pp. 4863–4870. doi: 10.1021/jf0636465.

Pflugmacher, U., Averhoff, B. and Gottschalk, G. (1996) 'Cloning, sequencing, and expression of isopropylbenzene degradation genes from Pseudomonas sp. strain JR1: Identification of isopropylbenzene dioxygenase that mediates trichloroethene oxidation', *Applied and Environmental Microbiology*, 62(11), pp. 3967–3977.

Potuzak, M., Nichols, A. R. L., Dingwell, D. B. and Clague, D. A. (2008) 'Hyperquenched volcanic glass from Loihi Seamount, Hawaii', *Earth and Planetary Science Letters*, 270(1–2), pp. 54–62. doi: 10.1016/j.epsl.2008.03.018.

Quax, T. E. F., Claassens, N. J., Söll, D. and van der Oost, J. (2015) 'Codon Bias as a Means to Fine-Tune Gene Expression', *Molecular Cell*, 59(2), pp. 149–161. doi: 10.1016/j.molcel.2015.05.035.

Rauch, M., Schmidt, S., Arends, I. W. C. E., Oppelt, K., Kara, S. and Hollmann, F. (2017) 'Photobiocatalytic alcohol oxidation using LED light sources', *Green Chemistry*. Royal

Society of Chemistry, 19(2), pp. 376–379. doi: 10.1039/c6gc02008a.

Ricca, E., Brucher, B. and Schrittwieser, J. H. (2011) 'Multi-enzymatic cascade reactions: Overview and perspectives', *Advanced Synthesis and Catalysis*, 353(13), pp. 2239–2262. doi: 10.1002/adsc.201100256.

Rivard, B. S., Rogers, M. S., Marell, D. J., Neibergall, M. B., Chakrabarty, S., Cramer, C. J. and Lipscomb, J. D. (2015) 'Rate-Determining Attack on Substrate Precedes Rieske Cluster Oxidation during Cis-Dihydroxylation by Benzoate Dioxygenase', *Biochemistry*, 54(30), pp. 4652–4664. doi: 10.1021/acs.biochem.5b00573.

Rosano, G. L. and Ceccarelli, E. A. (2014) 'Recombinant protein expression in Escherichia coli: Advances and challenges', *Frontiers in Microbiology*, 5(APR), pp. 1–17. doi: 10.3389/fmicb.2014.00172.

Sauber, K., Fröhner, C., Rosenberg, G., Eberspächer, J. and Lingens, F. (1977) 'Purification and Properties of Pyrazon Dioxygenase from Pyrazon-Degrading Bacteria', *European Journal of Biochemistry*. Wiley/Blackwell (10.1111), 74(1), pp. 89–97. doi: 10.1111/j.1432-1033.1977.tb11370.x.

van Schie, M. M. C. H., Younes, S. H. H., Rauch, M. C. R., Pesic, M., Paul, C. E., Arends, I. W. C. E. and Hollmann, F. (2018) 'Deazaflavins as photocatalysts for the direct reductive regeneration of flavoenzymes', *Molecular Catalysis*, 452(February), pp. 277–283. doi: 10.1016/j.mcat.2018.04.015.

Schmidt, C. L. and Shaw, L. (2001) 'A comprehensive phylogenetic analysis of rieske and rieske-type iron-sulfur proteins', *Journal of Bioenergetics and Biomembranes*, 33(1), pp. 9–26. doi: 10.1023/A:1005616505962.

Schmidt, S., Scherkus, C., Muschiol, J., Menyes, U., Winkler, T., Hummel, W., Gröger, H., Liese, A., Herz, H. G. and Bornscheuer, U. T. (2015) 'An enzyme cascade synthesis of ε-caprolactone and its oligomers', *Angewandte Chemie, International Edition*, 54(9), pp. 2784–2787. doi: 10.1002/anie.201410633.

Schrittwieser, J. H., Sattler, J., Resch, V., Mutti, F. G. and Kroutil, W. (2011) 'Recent biocatalytic oxidation-reduction cascades', *Current Opinion in Chemical Biology*, 15(2), pp. 249–256. doi: 10.1016/j.cbpa.2010.11.010.

Sharpless, K. B., Amberg, W., Bennani, Y. L., Crispino, G. A., Hartung, J., Jeong, K. S., Kwong, H. L., Morikawa, K., Wang, Z. M., Xu, D. and Zhang, X. L. (1992) 'The Osmium-Catalyzed Asymmetric Dihydroxylation: A New Ligand Class and a Process Improvement', *Journal of Organic Chemistry*, 57(10), pp. 2768–2771. doi: 10.1021/jo00036a003.

Sievers, F., Wilm, A., Dineen, D., Gibson, T. J., Karplus, K., Li, W., Lopez, R., McWilliam, H., Remmert, M., Söding, J., Thompson, J. D. and Higgins, D. G. (2011) 'Fast, scalable generation of high-quality protein multiple sequence alignments using Clustal Omega', *Molecular Systems Biology*, 7(1), pp. 539–539. doi: 10.1038/msb.2011.75.

Sivropoulou, A., Papanikolaou, E., Nikolaou, C., Kokkini, S., Lanaras, T. and Arsenakis, M. (1996) 'Antimicrobial and Cytotoxic Activities of Origanum Essential Oils', *Journal of*

Agricultural and Food Chemistry, 44(5), pp. 1202–1205. doi: 10.1021/jf950540t.

Studier, F. W. (2005) 'Protein production by auto-induction in high-density shaking cultures', *Protein Expression and Purification*, 41(1), pp. 207–234. doi: 10.1016/j.pep.2005.01.016.

Suenaga, H., Goto, M. and Furukawa, K. (2001) 'Emergence of Multifunctional Oxygenase Activities by Random Priming Recombination', *Journal of Biological Chemistry*, 276(25), pp. 22500–22506. doi: 10.1074/jbc.M101323200.

Summers, R. M., Louie, T. M., Yu, C. L., Gakhar, L., Louie, K. C. and Subramanian, M. (2012) 'Novel, highly specific N-demethylases enable bacteria to live on caffeine and related purine alkaloids', *Journal of Bacteriology*, 194(8), pp. 2041–2049. doi: 10.1128/JB.06637-11.

Sydor, P. K., Barry, S. M., Odulate, O. M., Barona-Gomez, F., Haynes, S. W., Corre, C., Song, L. and Challis, G. L. (2011) 'Regio- and stereodivergent antibiotic oxidative carbocyclizations catalysed by Rieske oxygenase-like enzymes', *Nature Chemistry*. Nature Publishing Group, 3(5), pp. 388–392. doi: 10.1038/nchem.1024.

Taglieber, A., Schulz, F., Hollman, F., Rusek, M. and Reetz, M. T. (2008) 'Light-driven biocatalytic oxidation and reduction reactions: Scope and limitations', *ChemBioChem*, 9(4), pp. 565–572. doi: 10.1002/cbic.200700435.

Takami, W., Horinouchi, M., Nojiri, H., Yamane, H. and Omori, T. (1999) 'Evaluation of trichloroethylene degradation by *E. coli* transformed with dimethyl sulfide monooxygenase genes and/or cumene dioxygenase genes', *Biotechnology Letters*, 21(3), pp. 259–264. doi: 10.1023/A:1005404931086.

Tøndervik, A., Bruheim, P., Berg, L., Ellingsen, T. E., Kotlar, H. K., Valla, S. and Throne-Holst, M. (2012) 'Ralstonia sp. U2 naphthalene dioxygenase and Comamonas sp. JS765 nitrobenzene dioxygenase show differences in activity towards methylated naphthalenes', *Journal of Bioscience and Bioengineering*. The Society for Biotechnology, Japan, 113(2), pp. 173–178. doi: 10.1016/j.jbiosc.2011.10.001.

Vézina, J., Barriault, D. and Sylvestre, M. (2007) 'Family shuffling of soil DNA to change the regiospecificity of Burkholderia xenovorans LB400 biphenyl dioxygenase', *Journal of Bacteriology*, 189(3), pp. 779–788. doi: 10.1128/JB.01267-06.

Wackett, L. P. (2002) 'Mechanism and applications of Rieske non-heme iron dioxygenases', *Enzyme and Microbial Technology*, 31(5), pp. 577–587. doi: 10.1016/S0141-0229(02)00129-1.

Wolfe, M. D., Parales, J. V., Gibson, D. T. and Lipscomb, J. D. (2001) 'Single turnover chemistry and regulation of O2activation by the oxygenase component of naphthalene 1,2-dioxygenase', *Journal of Biological Chemistry*, 276(3), pp. 1945–1953. doi: 10.1074/jbc.M007795200.

Xu, Z. and Sigler, P. B. (1998) 'GroEL/GroES: Structure and function of a two-stroke folding machine', *Journal of Structural Biology*, 124(2–3), pp. 129–141. doi:

10.1006/jsbi.1998.4060.

Yoshiyama-Yanagawa, T., Enya, S., Shimada-Niwa, Y., Yaguchi, S., Haramoto, Y., Matsuya, T., Shiomi, K., Sasakura, Y., Takahashi, S., Asashima, M., Kataoka, H. and Niwa, R. (2011) 'The conserved rieske oxygenase DAF-36/Neverland is a novel cholesterol-metabolizing enzyme', *Journal of Biological Chemistry*, 286(29), pp. 25756–25762. doi: 10.1074/jbc.M111.244384.

Zachos, I., Gaßmeyer, S. K., Bauer, D., Sieber, V., Hollmann, F. and Kourist, R. (2015) 'Photobiocatalytic decarboxylation for olefin synthesis', *Chemical Communications*, 51(10), pp. 1918–1921. doi: 10.1039/c4cc07276f.

Zhang, W., Fernández-Fueyo, E., Ni, Y., Van Schie, M., Gacs, J., Renirie, R., Wever, R., Mutti, F. G., Rother, D., Alcalde, M. and Hollmann, F. (2018) 'Selective aerobic oxidation reactions using a combination of photocatalytic water oxidation and enzymatic oxyfunctionalizations', *Nature Catalysis*. Springer US, 1(1), pp. 55–62. doi: 10.1038/s41929-017-0001-5.

Zhang, W. and Hollmann, F. (2018) 'Nonconventional regeneration of redox enzymes - a practical approach for organic synthesis?', *Chemical Communications*. Royal Society of Chemistry, 54(53), pp. 7281–7289. doi: 10.1039/c8cc02219d.

7 APPENDICES

7.1 APPENDIX A

TABLE 28 - List of primers used for cloning and sequencing.

Name	Sequence 5'-3'	Description
1_Fd+restr_FW	CGCGGATCCATGACCTTTAGC	Ferredoxin + restriction sites
2_Fd+restr_RV	AGTGCGGCCGCTTACGGTG	Ferredoxin + restriction sites
3_FdR+restr_FW	GACAAGCTTGCATGATTAAAAGCATCG	Ferredoxin Reductase + restriction sites
4_FdR+restr_RV	AGTGCGGCCGCTTACTCGC	Ferredoxin Reductase + restriction sites
5_CumA1+restr_FW	CGCGGATCCATGAGCAGCATTATTAAC	CumA1 + restriction sites
6_CumA1+restr_RV	GAGTGCGGCCGCTTAGCTTTTCAG	CumA1 + restriction sites
7_CumA2+restr_FW	CGCGGATCCATGAGCCGTGTTC	CumA2 + restriction sites
8_CumA2+restr_RV	GAGTGCGGCCGCTCAAAAAAACTG	CumA2 + restriction sites
9_CumA1+A_FW	CTAGAAATAATTTTGTTTAACTTTAAGAAGGAGATATACATGAGCAGCATTATTAACAA	gibson assembly primer with ~40bp overhang
10_CumA1+A_RV	TGTATATCTCCTTCTTATACTTAACTAATATACTAAGATGGGGTTAGCTTTTCAGGGTATCCC	gibson assembly primer with ~40bp overhang
11_CumA2+A_FW	CCCCATCTTAGTATATTAGTTAAGTATAAGAAGGAGATATACAATGAGCCGTGTTCAGGTTGC	gibson assembly primer with ~40bp overhang
12_CumA2+A_RV	TCCTGGCTGTGGTGATGATGGTGATGGCTGCTGCCCATGTCAAAAAAACTGGCTCAGAT	gibson assembly primer with ~40bp overhang
13_Fd+A_FW	ATCTTAGTATATTAGTTAAGTATAAGAAGGAGATATACAATGACCTTTAGCAAAGTTTG	gibson assembly primer with ~40bp overhang
14_Fd+A_RV	TGTATATCTCCTTCTTATACTTAACTAATATACTAAGATGGGGTTACGGTGCCAGATAGCCAG	gibson assembly primer with ~40bp overhang
15_FdR+A_FW	CCCCATCTTAGTATATTAGTTAAGTATAAGAAGGAGATATACAATGATTAAAAGCATCGTGAT	gibson assembly primer with ~40bp overhang
16_FdR+A_RV	ATCGCGTGGCCGGCCGATATCCAATTGAGATCTGCCATATTACTCGCAACGTTCGGCTT	gibson assembly primer with ~40bp overhang
17_Fd+B_RV	ATCGCGTGGCCGGCCGATATCCAATTGAGATCTGCCATATTACGGTGCCAGATAGCCAG	gibson assembly primer with ~40bp overhang

Name	Sequence 5'-3'	Description
18_CumA1+B_RV	TCCTGGCTGTGGTGATGATGGTGAT GGCTGCTGCCCATGTTAGCTTTTCAG GGTATCCC	gibson assembly primer with ~40bp overhang
19_CumA1+C_FW	GCTAGCATGACTGGTGGACAGCAAA TGGGTCGCGGATCCATGAGCAGCAT TATTAACAA	gibson assembly primer with ~40bp overhang
20_CumA1+C_RV	TTTGGCCGCTGCTTCTTTGGCCGCTG CTTCGCTTTTCAGGGTATCCCAAC	gibson assembly primer with ~40bp overhang
21_Fd+C_FW	GAAGCAGCGGCCAAAGAAGCAGCGG CCAAAATGACCTTTAGCAAAGTTTG	gibson assembly primer with ~40bp overhang
22_Fd+C_RV	TGCGGCCGCAAGCTTGTCGACGGAG CTCGAATTCGGATCTTACGGTGCCA GATAGCCAG	gibson assembly primer with ~40bp overhang
23_CumA1+B_FW	ACCATGGGCAGCAGCCATCACCATC ATCACCACAGCCAGATGAGCAGCAT TATTAACAA	gibson assembly primer with ~40bp overhang
24_Fd+D_RV	CTTGTCGACCTGCAGGCGCGCCGAG CTCGAATTCGGATCTTACGGTGCCA GATAGCCAG	gibson assembly primer with ~40bp overhang
25_Duet_MCS1_FW	ATGCGTCCGGCGTAGA	pETDuet-1 MCS1 seq. FW
26_Duet_MCS1_RV	GATTATGCGGCCGTGTACAA	pETDuet-1 MCS1 seq. RV
27_Duet_MCS2_FW	TTGTACACGGCCGCATAATC	pETDuet-1 MCS2 seq. FW
28_pBAD_FW	ATGCCATAGCATTTTTATCC	pBAD seq. FW
29_pBAD_RV	GATTTAATCTGTATCAGG	pBAD seq. RV
30_FP-seq_1_FW	GTCTGATTTTTGCCAACTGG	sequencing primer fusion protein
31_FP-seq_2_FW	CTATGTTTATAGCGAAGAAG	sequencing primer fusion protein
32_Duet_Spacer_FW	CATGGGCAGCAGCCATC	spacer between MCSI and MCSII pETDuet
33_Duet_Spacer_RV	TGTATATCTCCTTCTTATACTTAACT AATATAC	spacer between MCSI and MCSII pETDuet
40_pBAD_bb_FW	CTGGCTATCTGGCACCGTAAGCTGTT TTGGCGGATGAGAG	gibson assembly pBAD Fusion (CumA1-Fd)
41_pBAD_bb_RV	TTGTTAATAATGCTGCTCATGGTTAA TTCCTCCTGTTAGCC	gibson assembly pBAD Fusion (CumA1-Fd)
42_FP-1_FW	GCTAACAGGAGGAATTAACCATGAG CAGCATTATTAACAAAGAA	gibson assembly pBAD Fusion (CumA1-Fd)
43_FP-1_RV	CTCTCATCCGCCAAAACAGCTTACGG TGCCAGATAGCCAG	gibson assembly pBAD Fusion (CumA1-Fd)
44_pBAD_bb+HIS_FW	CTGGCTATCTGGCACCGTAAGCTGTT TTGGCGGATGAGAG	gibson assembly pBAD Fusion (CumA1-Fd) + HIS_n-term
45_pBAD_bb+HIS_RV	TTGTTAATAATGCTGCTCATAGCCAT ACCATGATGATGATG	gibson assembly pBAD Fusion (CumA1-Fd) + HIS

Name	Sequence 5'-3'	Description
46_FP+HIS_FW	ATCATCATCATGGTATGGCTATGAGCAGCATTATTAACAAAGAA	gibson assembly pBAD Fusion (CumA1-Fd) + HIS
47_FP+HIS_RV	CTCTCATCCGCCAAAACAGCTTACGGTGCCAGATAGCCAG	gibson assembly pBAD Fusion (CumA1-Fd) + HIS_n-term
48_FP+HIS_c-term_RV	CTCTCATCCGCCAAAACAGCTTAATGATGATGATGATGATGCGGTGCCAGATAGCCAGC	gibson assembly pBAD Fusion (CumA1-Fd) + HIS_c_term
49_pBAD_bb+HIS_c-term_FW	GCTGGCTATCTGGCACCGCATCATCATCATCATCATTAAGCTGTTTTGGCGGATGAGAG	gibson assembly pBAD Fusion (CumA1-Fd) + HIS_c-term
50_pIP107D_FW_seq_1	GCCAATCTCCTCGGGACTTTGC	sequencing of pIP107D FW #1
51_pIP107D1_RV_seq_1	GCAAAGTCCCGAGGAGATTGGC	sequencing of pIP107D RV #1
52_pIP107D_FW_seq_2	GGATCCTTGTTGGTATGCATC	sequencing of pIP107D FW #2
53_pIP107D_RV_seq_2	GTTCCCCCTTGATTGAAGGGG	sequencing of pIP107D RV #2
54_pIP107D_FW_seq_3	CTTTAGGGTTCCGATTTAGTGC	sequencing of pIP107D FW #3
55_pIP107D_cuma1_FW	ATGAGTTCAATAATAAATAAAGAAG	sequencing of pIP107D FW CumA1
56_pIP107D_cuma1_RV	TCAAGACTTTAGCGTGTCCCAAC	sequencing of pIP107D RV CumA1
57_pIP107D_cuma2_1_FW	ATGACATCCGCTGATTTGACAAAAC	sequencing of pIP107D FW CumA2
58_pIP107D_cuma2_2_RV_spacer	GCAACTGTGCTTCGCGATAGTAG	sequencing of pIP107D RV CumA2 over spacer
59_pIP107D_cuma2_3_FW_2	GCTGGTACTTTGGAAGTTAGTTC	sequencing of pIP107D FW 2 (end of cuma2 and spacer)
60_pIP107D_cuma3_1_FW	ATGACTTTTTCCAAAGTTTGTG	sequencing of pIP107D FW CumA2
61_pIP107D_cuma3_2_RV_spacer	GTTGCGAACAACTCTCCATCGACG	sequencing of pIP107D RV CumA2 over spacer
62_pIP107D_cuma3_3_FW_2	GTGTCCGCACGGGCAAGGTAAAAG	sequencing of pIP107D FW 2 (end of cuma2 and spacer)
63_pIP107D_cuma1_RV_spacer	CTCATACAAATCCTGATCAGAG	sequencing of pIP107D RV CumA1 over spacer n-term
64_pIP107D_cuma1_FW_spacer	GCTAGAAGTAGACCTCTTTGTGC	sequencing of pIP107D RV CumA1 over spacer c-term

Name	Sequence 5'-3'	Description
65_pIP107D_FW_seq_4	CTTCTGACAACGATCGGAGG	sequencing of pIP107D FW #4
66_pIP107D_RV_seq_2_final	CGTAGCTGGTCTTTCCAG	sequencing of pIP107D RV #2 new because initial primer did not work
67_Fd_FW	ATGACCTTTAGCAAAGTTTGTG	Fd FW primer
68_Fd_RV_GA_1	CGGTGCCTCTTGAACTTCTTTGTTAATAATGCTGCTCATCGGTGCCAGATAGCCAGCAT	Fd RV primer with overhang CumA1
69_CumA1_FW	ATGAGCAGCATTATTAACAAAG	CumA1 FW primer
70_CumA1_RV	TTAGCTTTTCAGGGTATCCCAAC	CumA1 RV primer
71_Fd_RV_GA_2	CTGCTTTTGGCCGCTGCTTCTTTGGCCGCTGCTTCCGGTGCCAGATAGCCAGCAT	Fd RV with overhang linker sandy CumA1
72_CumA1_FW_GA_2	TGGCACCGGAAGCAGCGGCCAAAGAAGCAGCGGCCAAAAGCAGCATTATTAACAA	CumA1 FW with overhang linker sandy Fd
73_Fd_RV_GA_3	CTGCTGGAACCACCACCACCGGAACCACCACCACCCGGTGCCAGATAGCCAGCAT	Fd RV with overhang G4S linker
74_CumA1_FW_GA_3	CACCGGGTGGTGGTGGTTCCGGTGGTGGTGGTTCCAGCAGCATTATTAACAAAGA	CumA1 FW with overhang G4S linker
75_pBAD_BB_fd-cuma1_FW	ATGATGAGCGAACCGAGTTGGGATACCCTGAAAAGCTAAGCTGTTTTGGCGGATGAGAG	FW primer backbone pBAD for Fd-CumA1 fusion protein
76_pBAD_BB_fd-cuma1_RV	CGGAACATCACTAACTTCACAAACTTTGCTAAAGGTCATGGTTAATTCCTCCTGTTAGC	RV primer backbone pBAD for Fd-CumA1 fusion protein
77_pIP107D_bb_FW	CGGGATTTTATGAAAGCTAAAGCTGAGCGATGCGAGTGACGAGCTCGAATTCACTGGCC	FW primer for backbone pIP107D repair
78_pIP107D_bb_RV	CAGCCAAGCCAGCACCAATAATG	RV primer for backbone pIP107D repair
79_CumA4_FW	ATGATTAAATCAATCGTC	CumA4_native_FW
80_CumA4_RV	TCACTCGCATCGCTCAGC	CumA4_native_RV
81_pIP107D_BB_FW	CGAGCTCGAATTCACTGGC	pIP107D_BB_FW
82_pIP107D_BB_RV	GGCGCTAGATACCCGGC	pIP107D_BB_RV
83_CumA4_OH_FW	GCGATGTGTTCGTAGACTTTGATGCCGGGTATCTAGCGCCATGATTAAATCAATCGTC	CumA4 with overhang for pIP107D BB
84_CumA4_OH_RV	TCACGACGTTGTAAAACGACGGCCAGTGAATTCGAGCTCGTCACTCGCATCGCTCAGC	CumA4 with overhang for pIP107D BB
85_QC_pIPFIX-M232A_FW	CCGAGCAATTCTGTAGCGATGCGTACCATGCGG	QuickChange pIPFIX-M232A

Name	Sequence 5'-3'	Description
86_QC_pIPFIX-M232A_RV	GCCATCGTTCCCGCATGGTACGCATCGCTAC	QuickChange pIPFIX-M232A
87_CumA2_native_RV	TTAGAAAAACTGGCTGAGATTATTCGC	native gene primer
88_CumA3_native_RV	TCATGGCGCTAGATACCC	native gene primer
99_QC_pIPFIX-G205V_FW	GCTCGATCGGACCGAGGCAGTTACTCAGGTC	QC to repair pIPFIX G205V
100_QC_pIPFIX-G205V_RV	CATACCGGTGATGACCTGAGTAACTGCCTCGGTC	QC to repair pIPFIX G205V

7.2 APPENDIX B

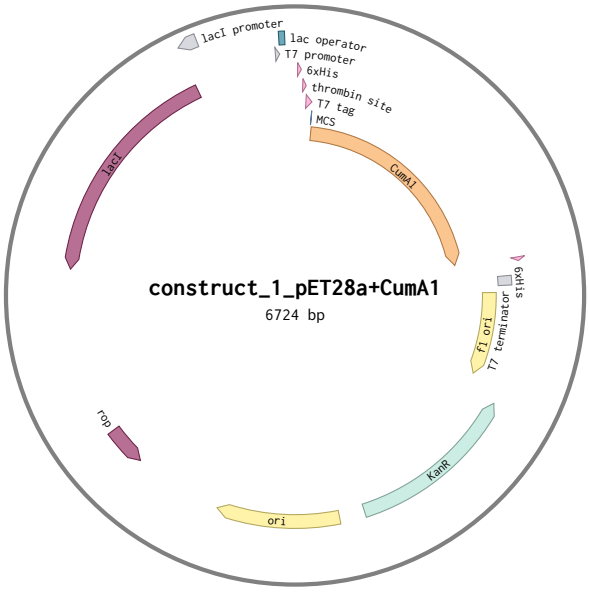

FIGURE 33 – Vector map construct 1, created using Benchling.

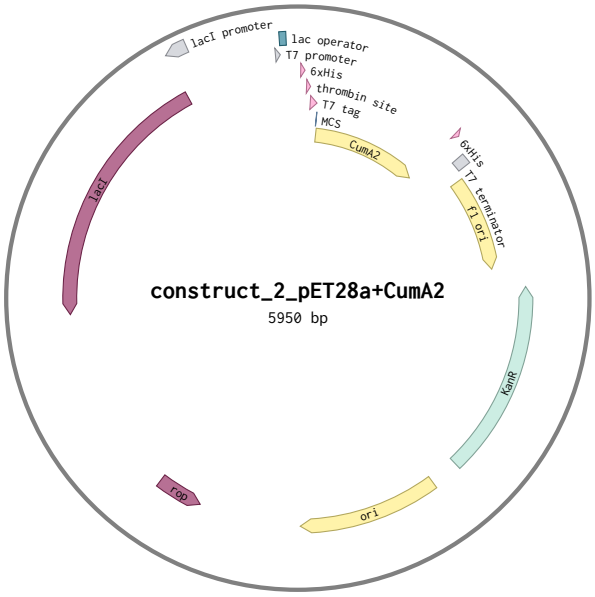

FIGURE 34 - Vector map construct 2, created using Benchling.

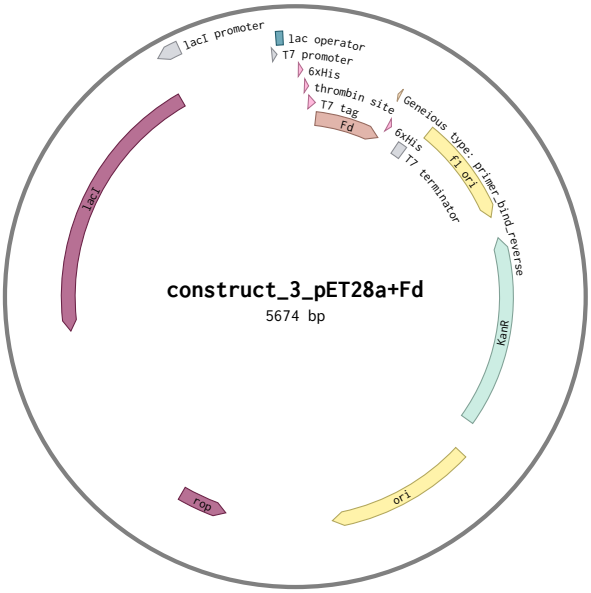

FIGURE 35 - Vector map construct 3, created using Benchling.

FIGURE 36 - Vector map construct 4, created using Benchling.

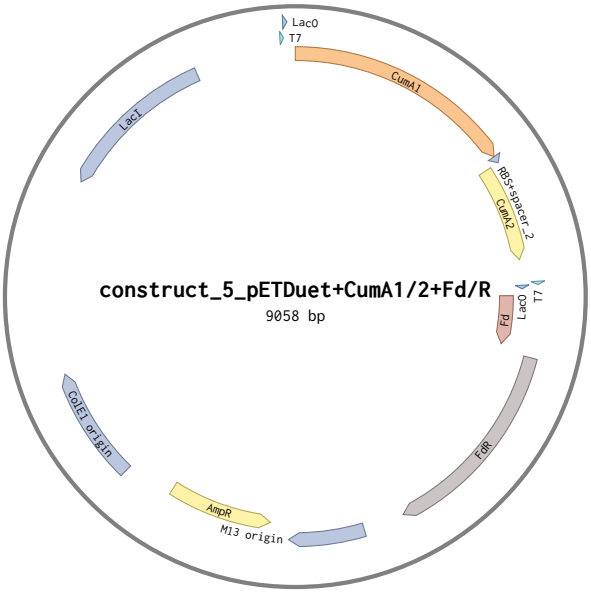

FIGURE 37 - Vector map construct 5, created using Benchling.

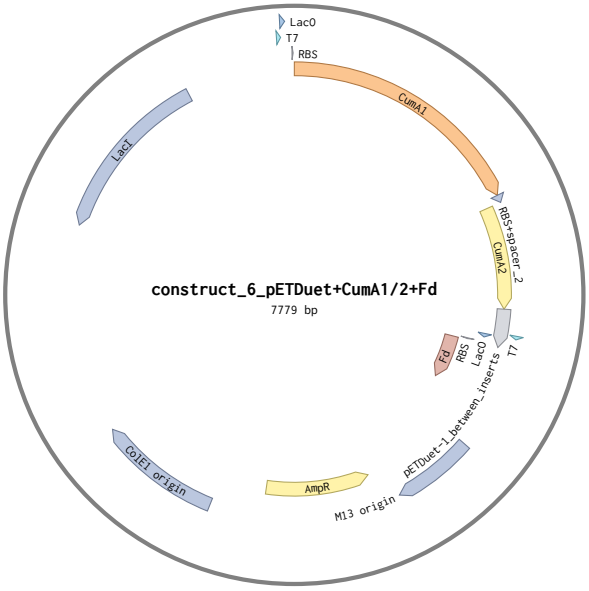

FIGURE 38 - Vector map construct 6, created using Benchling.

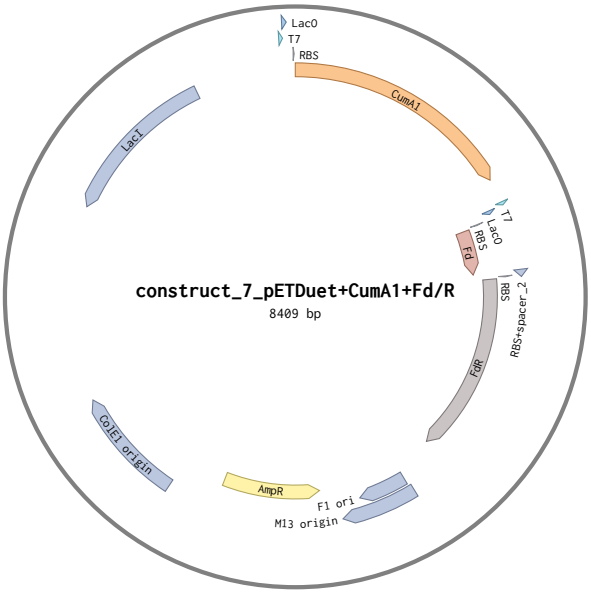

FIGURE 39 - Vector map construct 7, created using Benchling.

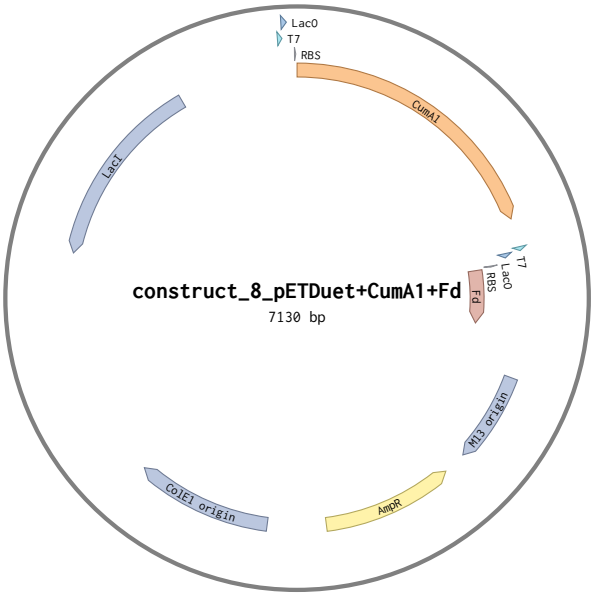

FIGURE 40 - Vector map construct 8, created using Benchling.

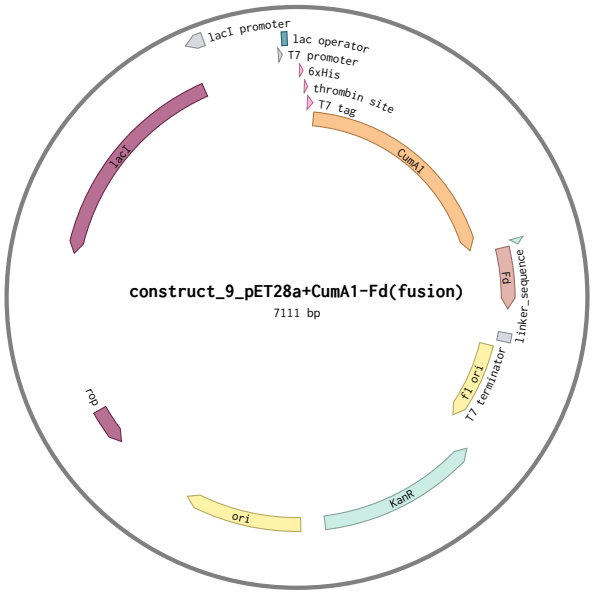

FIGURE 41 - Vector map construct 9, created using Benchling.

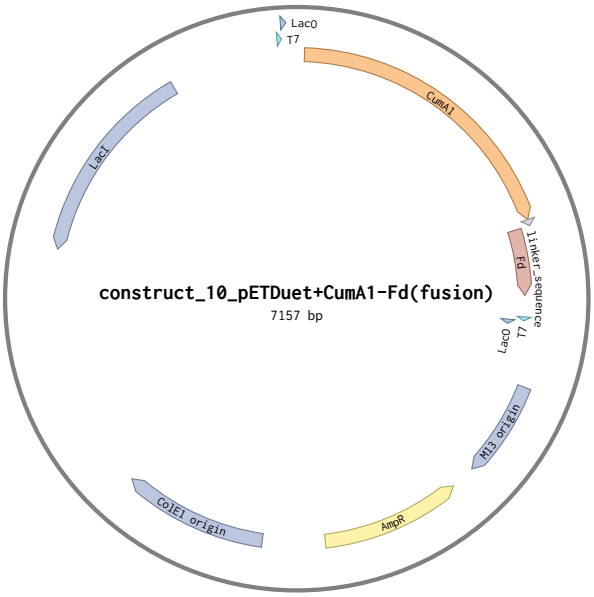

FIGURE 42 - Vector map construct 10, created using Benchling.

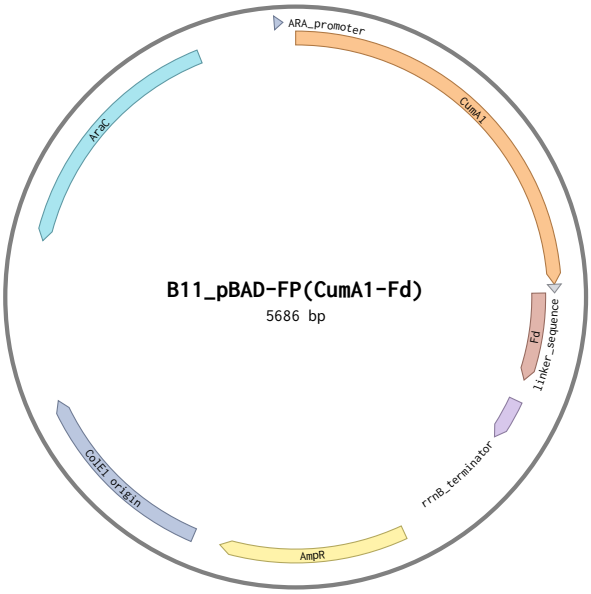

FIGURE 43 - Vector map construct 11, created using Benchling.

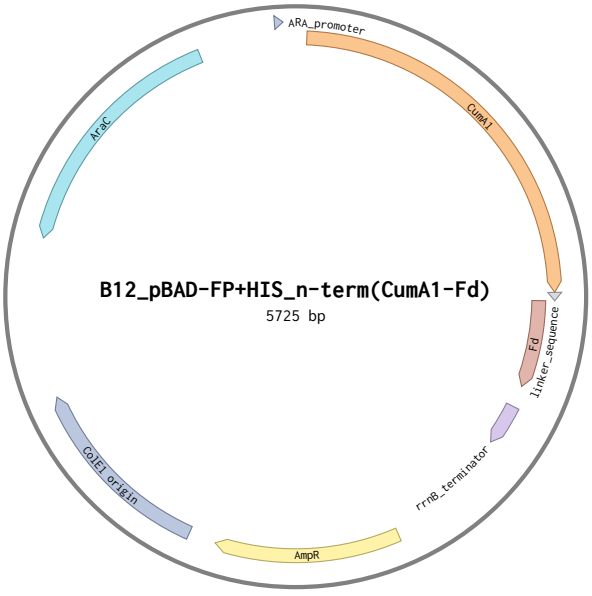

FIGURE 44 - Vector map construct 12, created using Benchling.

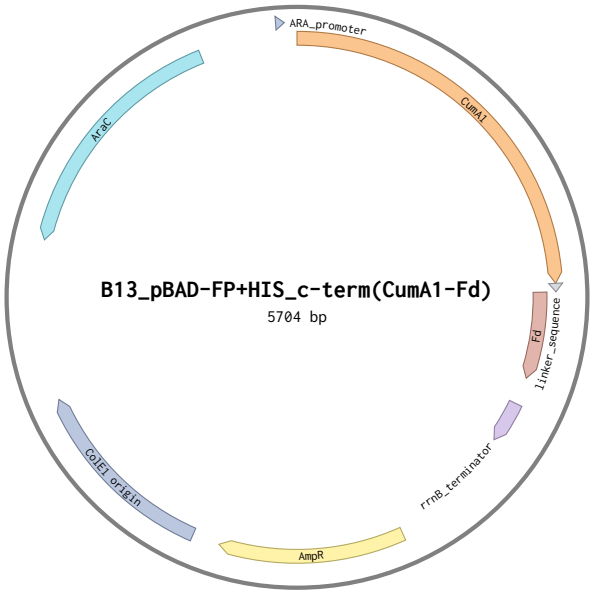

FIGURE 45 - Vector map construct 13, created using Benchling.

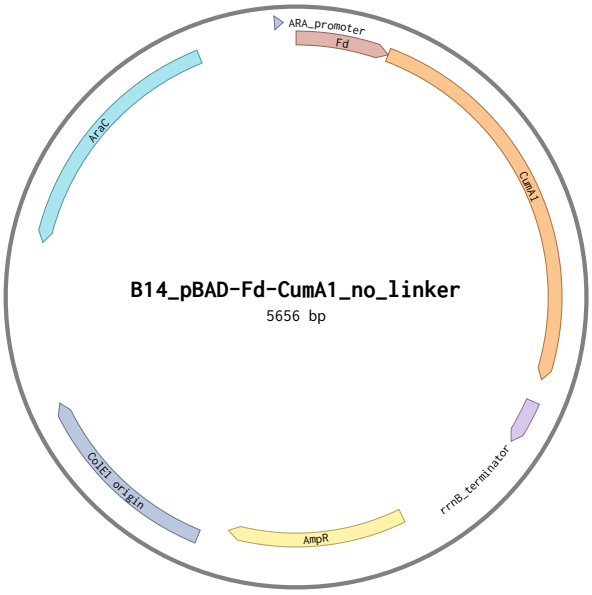

FIGURE 46 - Vector map construct 14, created using Benchling.

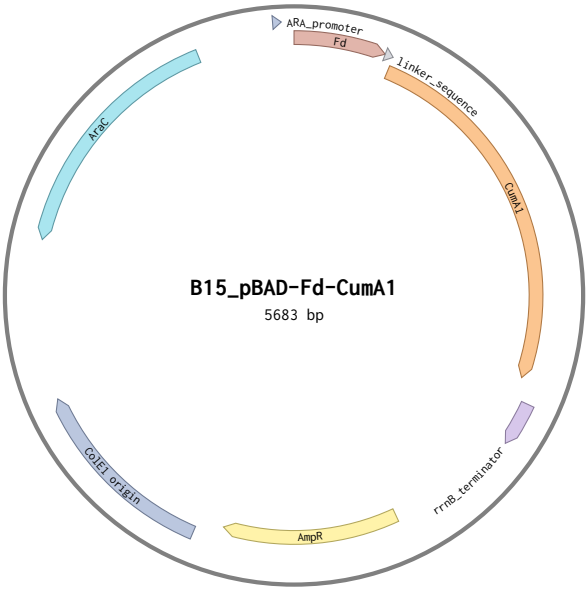

FIGURE 47 - Vector map construct 15, created using Benchling.

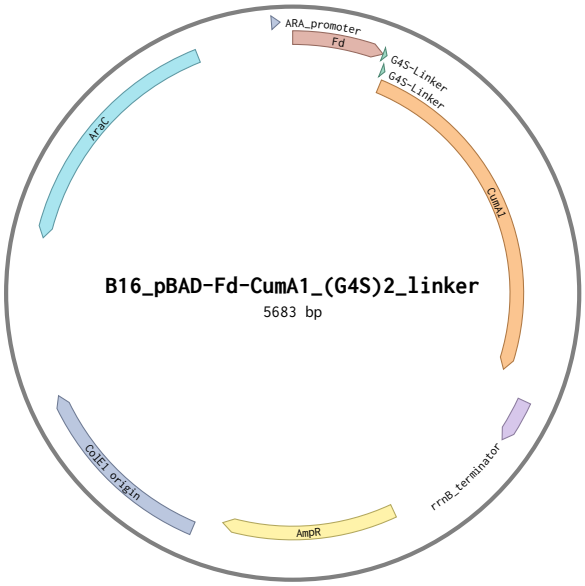

FIGURE 48 - Vector map construct 16, created using Benchling.

7.3 APPENDIX C

TABLE 29 - GC-FID parameters used for achiral analytics of styrene and products.

Achiral GC-FID parameters - styrene detection	
Instrument	GC-2010 Plus (Shimadzu Europa GmbH.)
Column	Zebron ZB-5 (Phenomenex Inc.) length: 30 m, inner diameter: 0.32 mm, film thickness: 0.25 μM
Injection volume	1 μL
Injection temp.	230 °C
Injection mode	Split
Flow control mode	pressure
Pressure	35 kPa
Total flow	24.6 mL/min
Column flow	1.03 mL/min
Linear velocity	19.6 cm/s
Purge flow	3 mL/min
Split ratio	20
Oven temp. program	2 min at 50 °C, 10 °C/min to 280 °C, 2 min at 280 °C, 40 °C/min to 310 °C, 2 min at 310 °C
FID temperature	320 °C

TABLE 30 - GC-FID parameters used for achiral analytics of *R*-(+)-limonene and products.

Achiral GC-FID parameters - (*R*)-(+)-limonene detection	
Instrument	GC-2010 Plus (Shimadzu Europa GmbH.)
Column	Zebron ZB-5 (Phenomenex Inc.) length: 30 m, inner diameter: 0.32 mm, film thickness: 0.25 μM
Injection volume	1 μL
Injection temp.	230°C
Injection mode	Split
Flow control mode	pressure
Pressure	22.7 kPa
Total flow	15.6 mL/min
Column flow	0.6 mL/min
Linear velocity	12.5 cm/s
Purge flow	3 mL/min
Split ratio	20
Oven temp. program	4 min at 60 °C, 5 °C/min to 165 °C, 2 min at 165 °C, 15 °C/min to 300 °C, 2 min at 300 °C
FID temperature	320 °C

TABLE 31 - GC-FID parameters used for chiral analytics of styrene and products.

Chiral GC-FID parameters - styrene detection	
Instrument	Nexis GC-2030 (Shimadzu Europa GmbH.)
Column	Hydrodex-β-6TBDM (Macherey-Nagel) length: 25 m, inner diameter: 0.25 mm, film thickness: 0.25 μM
Injection volume	1 μL
Injection temp.	230 °C
Injection mode	Split
Flow control mode	velocity
Pressure	89 kPa
Total flow	111.3 mL/min
Column flow	1.07 mL/min
Linear velocity	30 cm/s
Purge flow	3 mL/min
Split ratio	100
Oven temp. program	2 min at 90 °C, 2 °C/min to 120 °C, 1 °C/min to 150 °C, 40 °C/min to 230 °C, 3 min at 230 °C
FID temperature	250 °C

TABLE 32 - GC-FID parameters used for chiral analytics of *R*-(+)-limonene and products.

Chiral GC-FID parameters - (*R*)-(+)-limonene detection	
Instrument	Nexis GC-2030 (Shimadzu Europa GmbH.)
Column	Hydrodex-β-6TBDM (Macherey-Nagel) length: 25 m, inner diameter: 0.25 mm, film thickness: 0.25 μM
Injection volume	1 μL
Injection temp.	230 °C
Injection mode	Split
Flow control mode	velocity
Pressure	83.1 kPa
Total flow	106.0 mL/min
Column flow	1.02 mL/min
Linear velocity	30 cm/s
Purge flow	3 mL/min
Split ratio	100
Oven temp. program	5 min at 100 °C, 15 °C/min to 230 °C, 5 min at 230 °C
FID temperature	250 °C

TABLE 33 - GC-MS parameters used for qualitative analyses.

GC-MS parameters	
Instrument	GCMS-QP2010 SE (Shimadzu Europa GmbH.)
Column	Zebron ZB-5MSi (Phenomenex Inc.) length: 30 m, inner diameter: 0.25 mm, film thickness: 0.25 μM
Injection volume	1 μL
Injection temp.	250 °C
Injection mode	Split
Flow control mode	linear velocity
Pressure	83.8 kPa
Total flow	14.4 mL/min
Column flow	1.13 mL/min
Linear velocity	39.5 cm/s
Purge flow	3 mL/min
Split ratio	9.1
Oven temp. program	4 min at 100 °C, 20 °C/min to 340 °C, 4 min at 340 °C
MS parameters	
Ion source temp.	250 °C
Interface temp.	320 °C
Mode:	Scan
Scan range	50 - 500 m/z

7.4 APPENDIX D

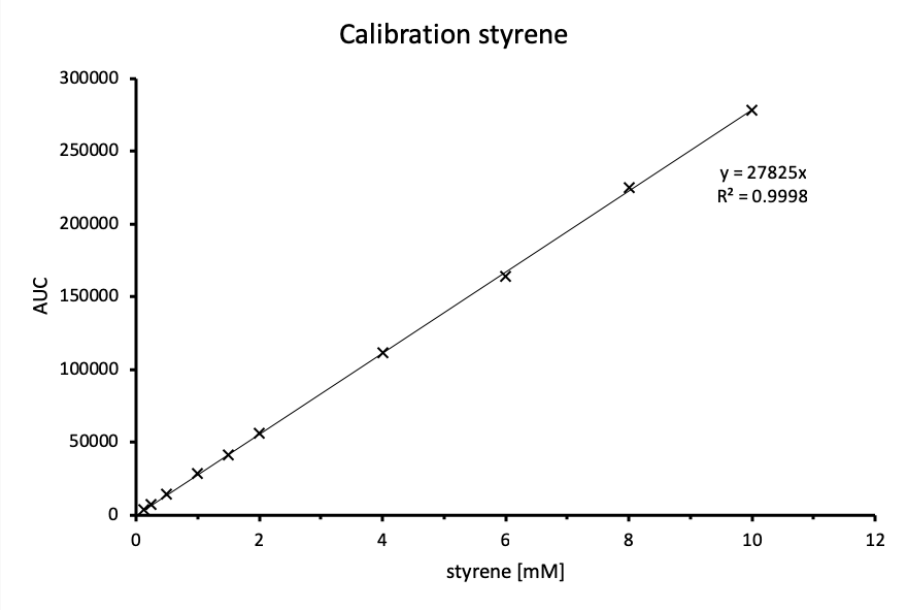

FIGURE 49 - Calibration curve of styrene on the Hydrodex-β-6TBDM (chiral column), y=27825x.

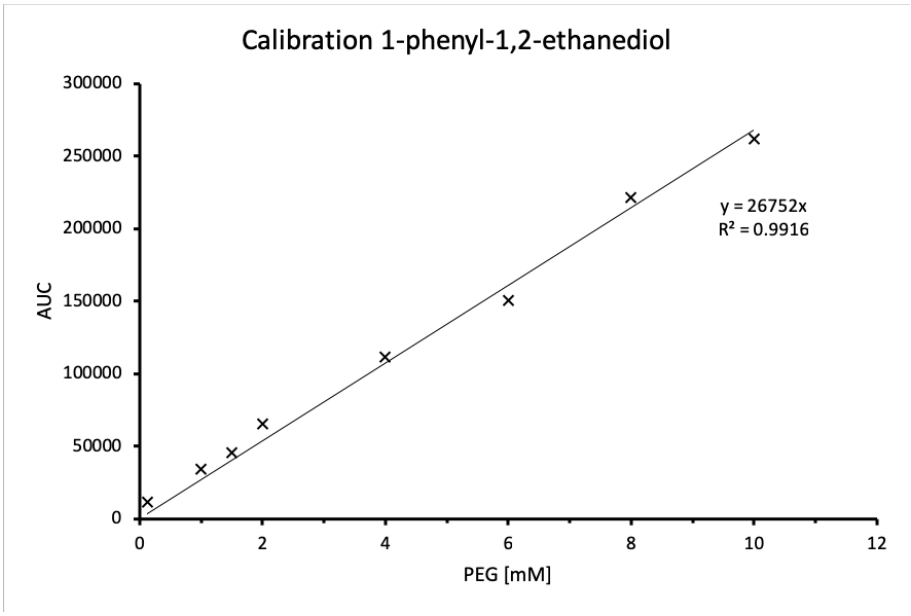

FIGURE 50 - Calibration curve of 1-phenyl-1,2-ethanediol on the Hydrodex-β-6TBDM (chiral column), y=26752x.

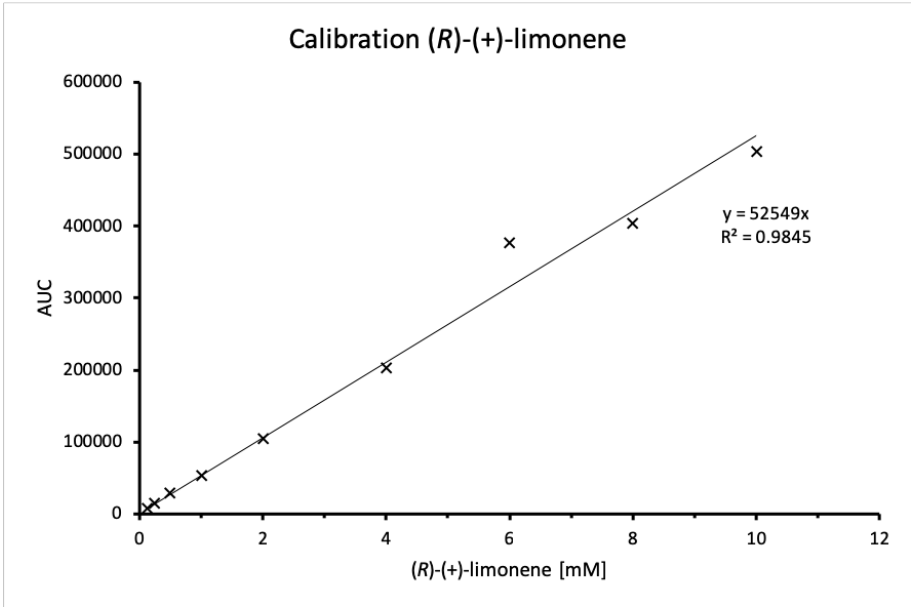

FIGURE 51 - Calibration curve of (*R*)-(+)-limonene on the Hydrodex-β-6TBDM (chiral column), y=5249x.

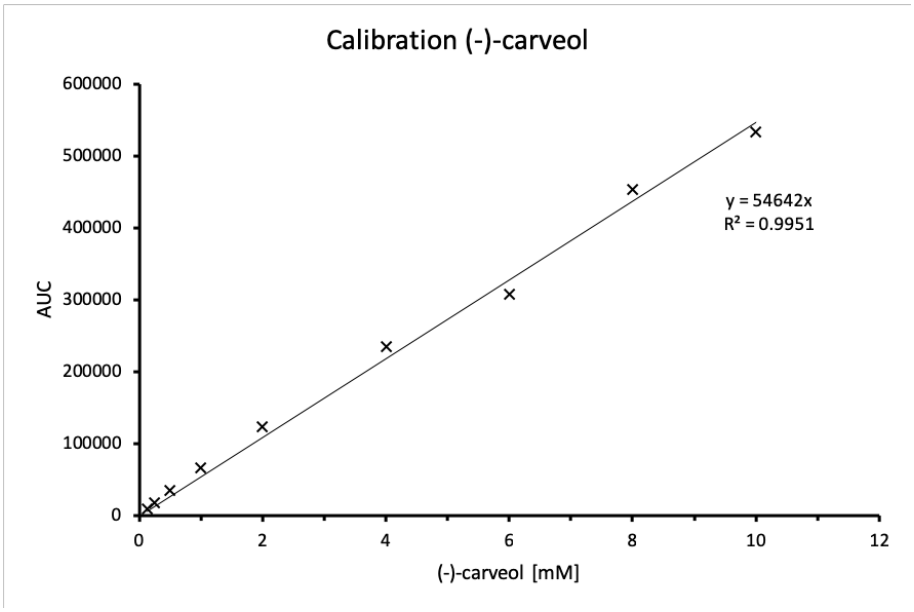

FIGURE 52 - Calibration of (-)-carveol, mixture of isomers on the Hydrodex-β-6TBDM (Chiral Column), y=54642x.

7.5 APPENDIX E

Construct 6 (pETDuet-1; MCSI: CumA1, CumA2; MCSII: Fd) in SHuffle

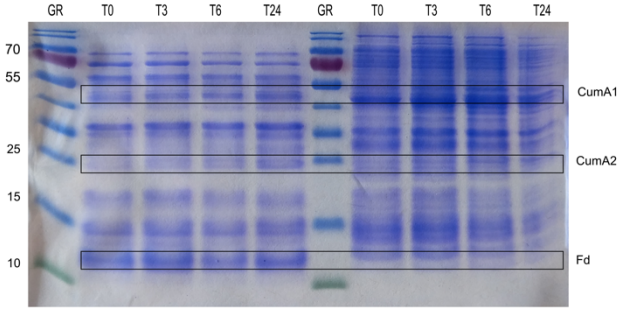

Construct 8 (pETDuet-1; MCSI: CumA1; MCSII: Fd) in SHuffle

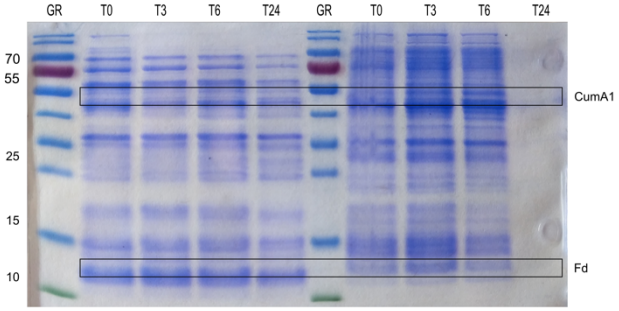

Construct 9 (pET28a, MCSI: CumA1-Fd) in SHuffle

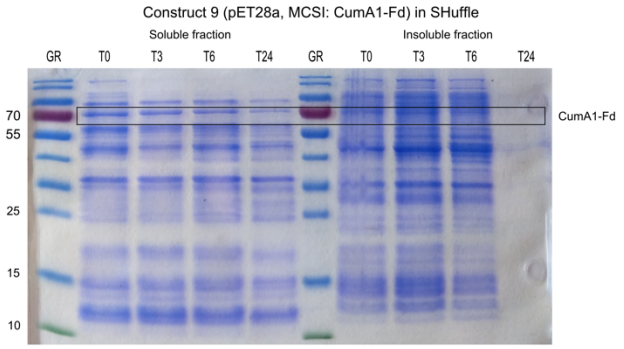

Construct 5 (pETDuet; MCSI: Fd, FdR; MCSII: CumA1, CumA2) in SHuffle

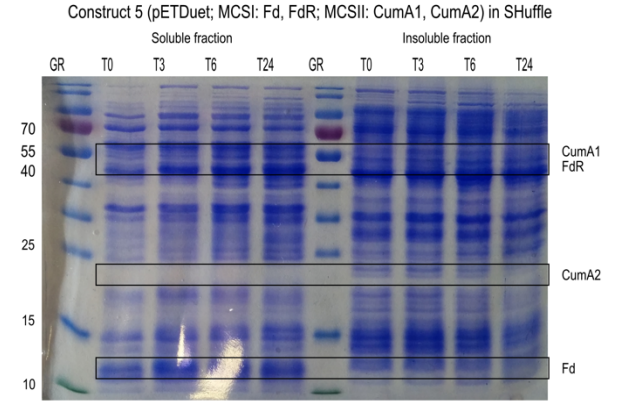

Construct 7 (pETDuet; MCSI: Fd, FdR; MCSII: CumA1, CumA2) in SHuffle

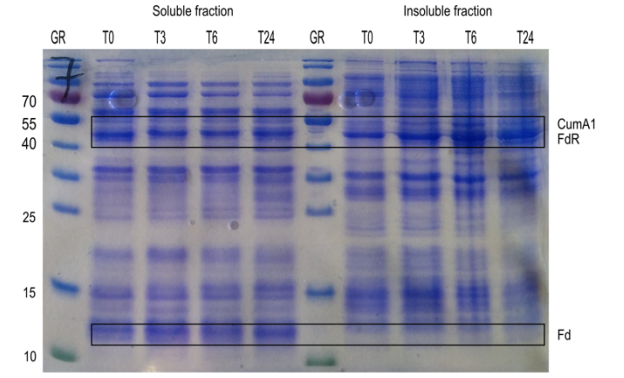

Construct 9 (pET28a, MCSI: CumA1-Fd) in SHuffle

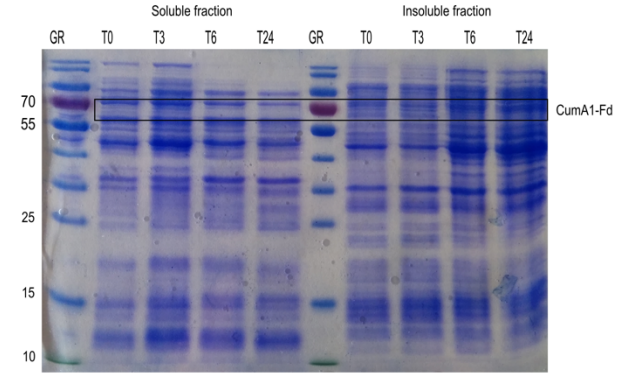

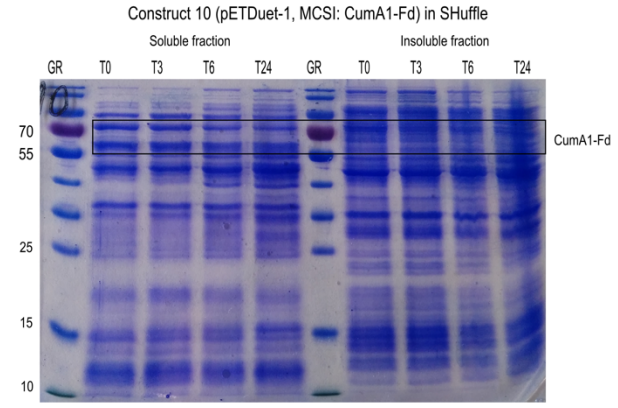
Construct 10 (pETDuet-1, MCSI: CumA1-Fd) in SHuffle
Soluble fraction
Insoluble fraction
GR T0 T3 T6 T24 GR T0 T3 T6 T24
70
55
25
15
10
CumA1-Fd

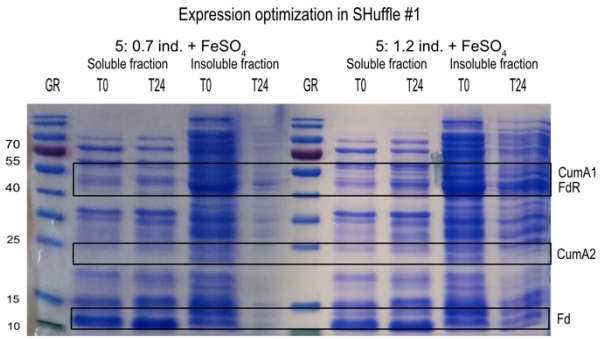
Expression optimization in SHuffle #1
5: 0.7 ind. + FeSO4
5: 1.2 ind. + FeSO4
Soluble fraction
Insoluble fraction
GR T0 T24 T0 T24 GR T0 T24 T0 T24
70
55
40
25
15
10
CumA1 FdR
CumA2
Fd

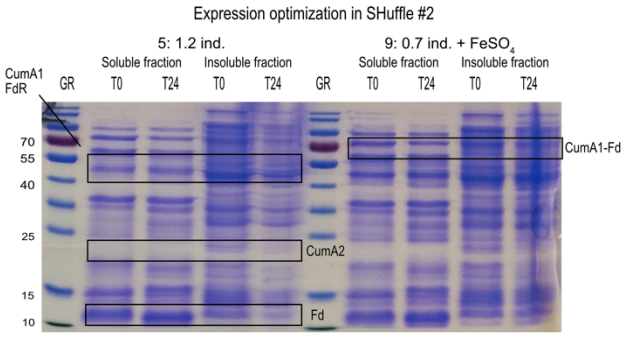
Expression optimization in SHuffle #2
5: 1.2 ind.
9: 0.7 ind. + FeSO4
Soluble fraction
Insoluble fraction
CumA1 FdR
GR T0 T24 T0 T24 GR T0 T24 T0 T24
70
55
40
25
15
10
CumA1-Fd
CumA2
Fd

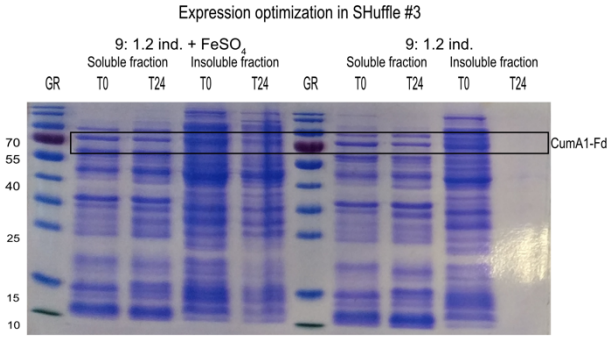
Expression optimization in SHuffle #3
9: 1.2 ind. + FeSO4
9: 1.2 ind.
Soluble fraction
Insoluble fraction
GR T0 T24 T0 T24 GR T0 T24 T0 T24
70
55
40
25
15
10
CumA1-Fd

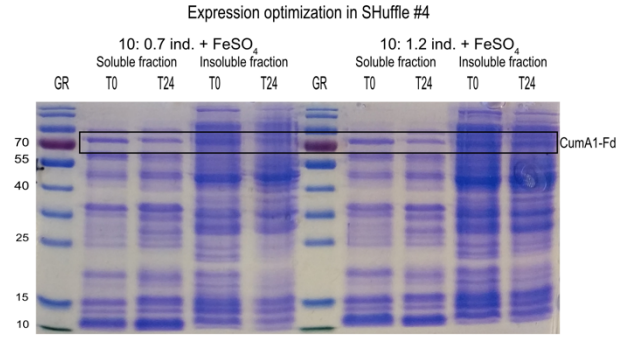
Expression optimization in SHuffle #4
10: 0.7 ind. + FeSO4
10: 1.2 ind. + FeSO4
Soluble fraction
Insoluble fraction
GR T0 T24 T0 T24 GR T0 T24 T0 T24
70
55
40
25
15
10
CumA1-Fd

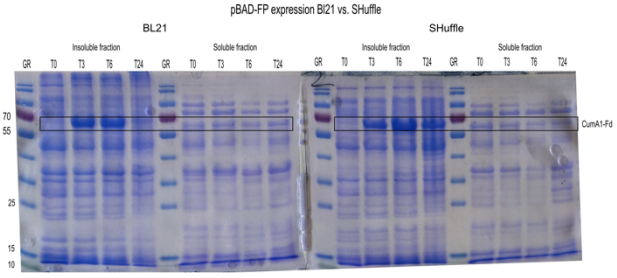
pBAD-FP expression Bl21 vs. SHuffle
BL21
SHuffle
Insoluble fraction
Soluble fraction
GR T0 T3 T6 T24 GR T0 T3 T6 T24 GR T0 T3 T6 T24 GR T0 T3 T6 T24
70
55
25
15
10
CumA1-Fd

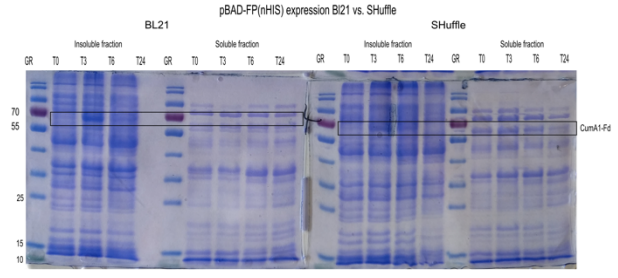
pBAD-FP(nHIS) expression Bl21 vs. SHuffle
BL21
SHuffle
Insoluble fraction
Soluble fraction
GR T0 T3 T6 T24 GR T0 T3 T6 T24 GR T0 T3 T6 T24 GR T0 T3 T6 T24
70
55
25
15
10
CumA1-Fd

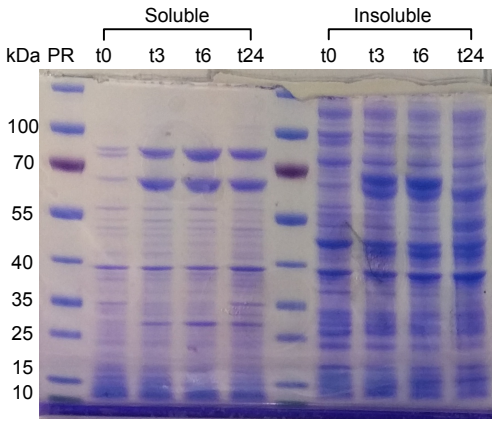

FIGURE 53 - Expression of construct 11 in *E. coli* BL21(DE3), with co-expression of dnaK-dnaJ-grpE groES-groEL

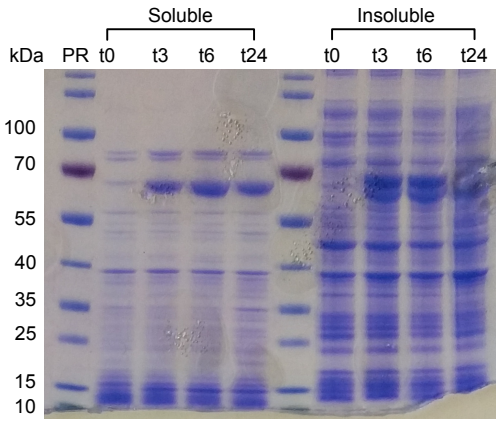

FIGURE 54 – Expression of construct 11 in *E. coli* BL21(DE3), with co-expression of groES-groEL

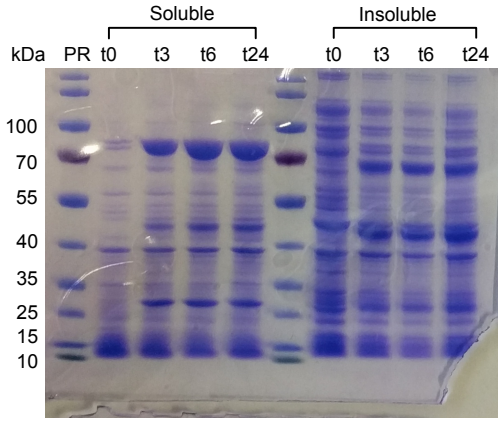

FIGURE 55 – Expression of construct 11 in *E.coli* BL21(DE3), with co-expression of dnaK-dnaJ-grpE

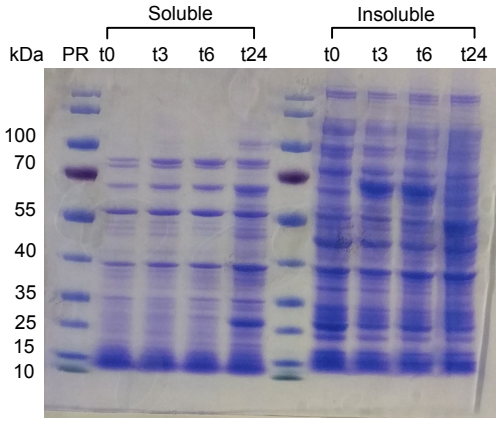

FIGURE 56 - Expression of construct 11 in *E. coli* BL21(DE3), with co-expression of groES-groEL-tig

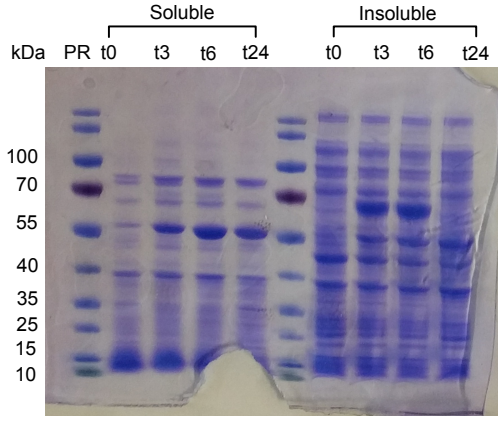

FIGURE 57 - Expression of construct 11 in *E. coli* BL21(DE3), with co-expression of tig

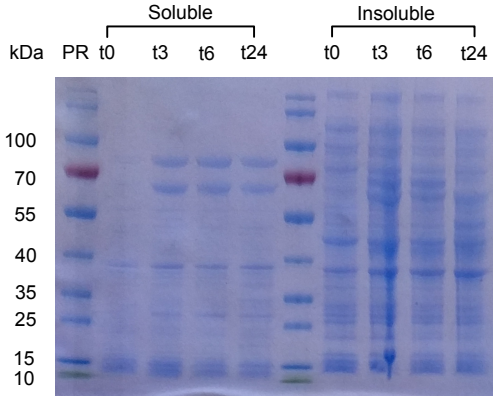

FIGURE 58 - Expression of construct 12 in *E. coli* BL21(DE3), with co-expression of dnaK-dnaJ-grpE groES-groEL

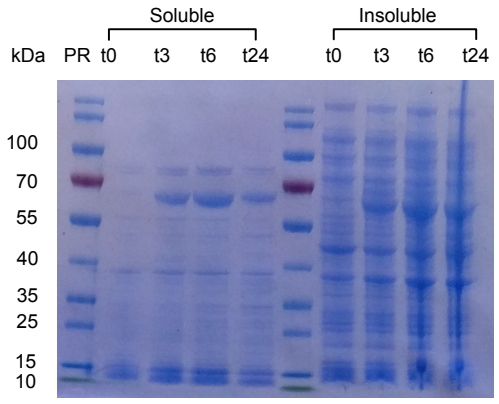

FIGURE 59 – Expression of construct 12 IN *E. coli* BL21(DE3), with co-expression of groES-groEL

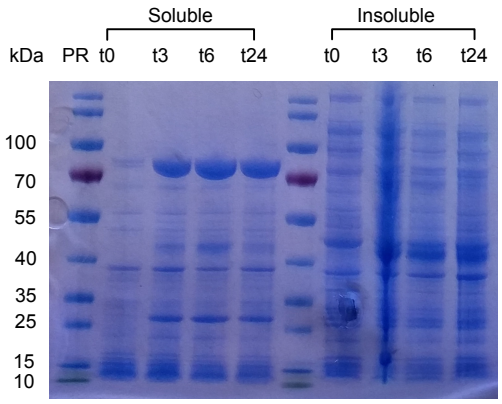

FIGURE 60 - Expression of construct 12 in *E. coli* BL21(DE3), with co-expression of dnaK-dnaJ-grpE

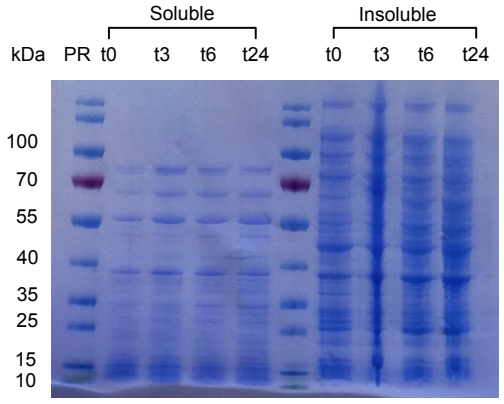

FIGURE 61 – Expression of construct 12 IN *E. coli* BL21(DE3), with co-expression of groES-groEL-tig

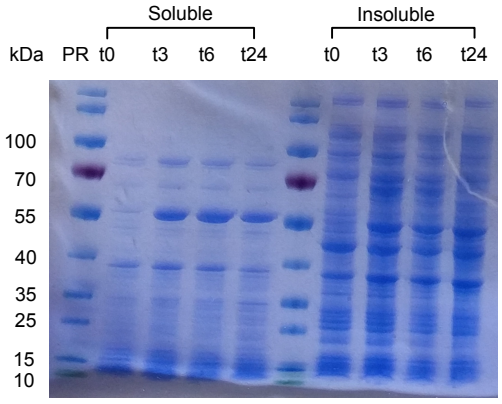

FIGURE 62 - Expression of construct 12 IN *E. coli* BL21(DE3), with co-expression of tig

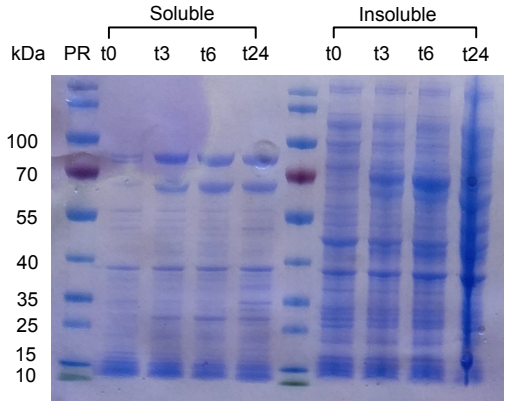

FIGURE 63 - Expression of construct 13 IN *E. coli* BL21(DE3), with co-expression of dnaK-dnaJ-grpE groES-groEL

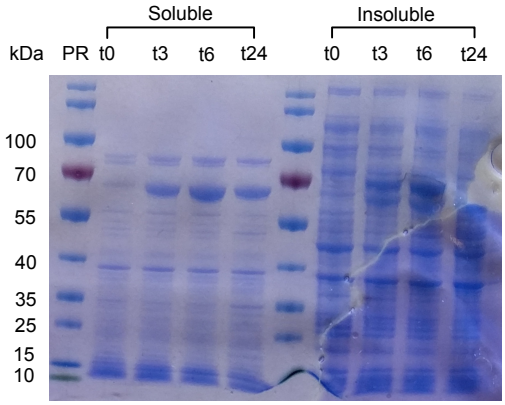

FIGURE 64 - Expression of construct 13 IN *E. coli* BL21(DE3), with co-expression of groES-groEL

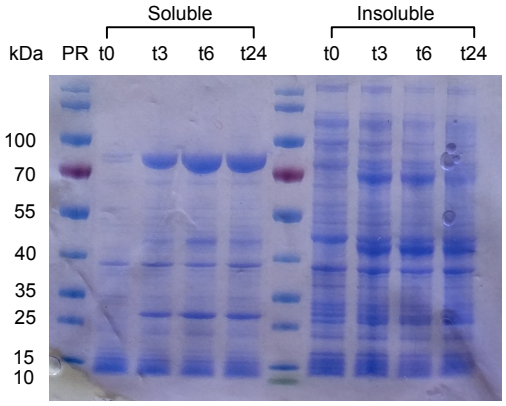

FIGURE 65 - Expression of construct 13 IN *E. coli* BL21(DE3), with co-expression of dnaK-dnaJ-grpE

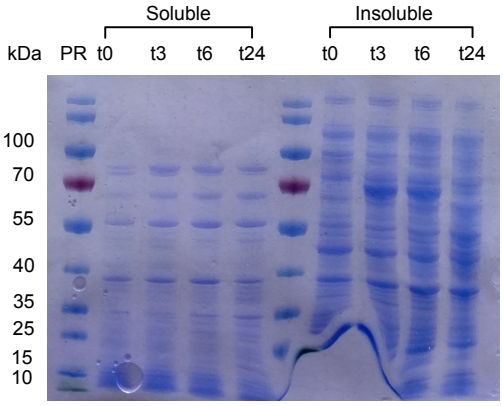

FIGURE 66 - Expression of construct 13 IN *E. coli* BL21(DE3), with co-expression of groES-groEL-tig

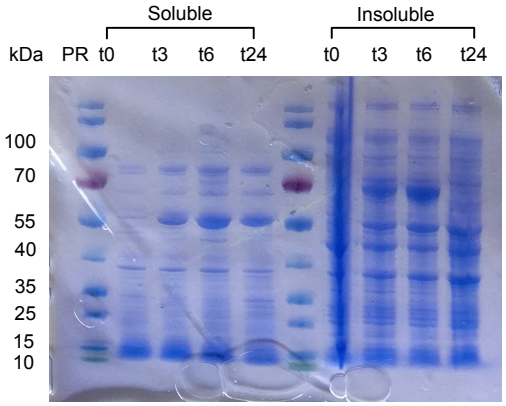

FIGURE 67 - Expression of construct 13 IN *E. coli* BL21(DE3), with co-expression of tig

7.6 APPENDIX F

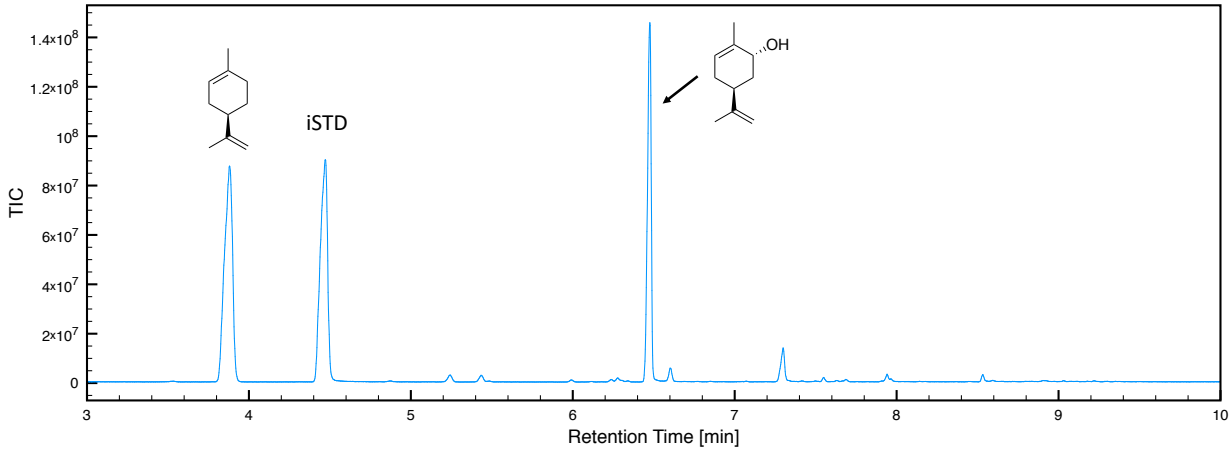

FIGURE 68 - GC-MS chromatogram showing the detection of (*R*)-(+)-limonene and carveol after 24 h whole-cell biotransformation with D-glucose supplemented CDO M232A.

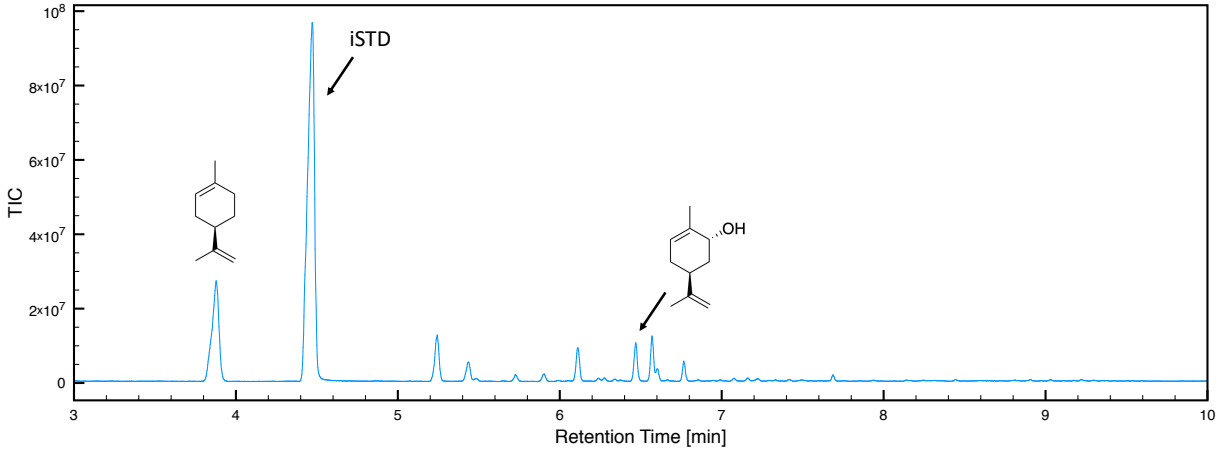

FIGURE 69 - GC-MS chromatogram showing the detection of (*R*)-(+)-limonene and carveol after 24 h light-driven whole-cell biotransformation with CDO M232A, EY and EDTA.